NORTHWESTERN UNIVERSITY

# Synthesis, Properties, and Applications of Colloidal Gold Nanoprisms

A DISSERTATION

SUBMITTED TO THE GRADUATE SCHOOL

IN PARTIAL FULFILLMENT OF THE REQUIREMENTS

for the degree

DOCTOR OF PHILOSOPHY

Field of Chemistry

By

Jill Erin Millstone

EVANSTON, ILLINOIS

December 2008

© Copyright by Jill Erin Millstone 2008

All Rights Reserved

# ABSTRACT

Synthesis, Properties, and Applications of Colloidal Gold Nanoprisms

Jill E. Millstone

Au nanoprisms are a new type of inorganic nanoparticle that is particularly interesting because these particles can be made in high yield, are composed of a metal with well known surface chemistry, exhibit strong, architecture and environment-sensitive optical features, and have well-defined crystallographic facets. All of these features make Au nanoprisms an excellent testbed for understanding, characterizing, and using the effects of particle shape at the nanoscale.

In Chapter 2, a seed-mediated growth process is presented for the production of colloidal Au nanoprisms with relatively homogeneous size distributions. The purity of nanostructures produced in this synthesis allowed the first observation of a weak quadrupole surface plasmon resonance in addition to a strong dipole resonance associated with the Au nanoprisms. The experimental optical spectra are shown to agree with discrete dipole approximation calculations modeled from the dimensions of Au nanoprisms produced in the synthesis.

Chapter 3 builds on this work by describing a method for controlling Au nanoprism edge length using seeding methodology. In this manner, the edge length of Au nanoprisms can be tailored over a range of 100 – 300 nm without appreciable changes in either nanoprism thickness or crystallinity. This work provided new insight into anisotropic gold nanoparticle growth and reactivity, and expanded the library of prism structures with optical features ranging from 1000 – 1800 nm. Based on this work and existing silver halide crystal growth theories, a preliminary nanoprism formation mechanism is proposed.

In Chapter 4, the site-selective chemical reactivity of the Au nanoprisms described in Chapter 3 is used to investigate the functionalization of the nanoprism and elucidate its surface

chemistry. It is shown that face-selective, DNA-ligand adsorption onto the nanoprism is time dependent, and can be exploited to selectively immobilize DNA on the edges of the particle.

Chapter 5 builds on the methods and techniques developed in Chapter 4 to make and use a variety of DNA-functionalized anisotropic nanostructures. This chapter describes the use of such conjugates in both diagnostic and therapeutic applications. For detections, DNA-conjugated nanodisk arrays are used as barcodes to readout the presence of biological target moieties. Additionally, gene delivery applications of Au nanoprisms are described by presenting a method for the preparation and cellular uptake of DNA-nanoprism conjugates.

Chapter 6 describes the most recent work completed on the shape-directing factors in the synthesis of Au nanoprisms. In this chapter, it is shown that CTAB, depending upon supplier, has an iodide contaminant (at a significant but varying level), which acts as a key shape directing element, because it can strongly and selectively bind to the gold (111) faces and favor the formation of anisotropic structures. Furthermore, by starting with pure CTAB and deliberately adjusting iodide concentration, it is shown that one can reproducibly drive the reaction to predominantly produce nanorods, nanoprisms, or nanospheres.

---

Thesis Advisor: Professor Chad A. Mirkin

*This thesis is dedicated to my grandparents:*

*Percy and Ida Millstone*

*Charlotte and David Michaelson*

# ACKNOWLEDGEMENTS

First, I would like to thank my advisor, Chad Mirkin. Through his enthusiasm and wisdom, I have learned how to become a better scientist, mentor, and writer. One particular thing I appreciate about Chad is his openness to science. He is always excited about and willing to work on an interesting result regardless of whether it was the result or project he had originally envisioned. It is also well known that Chad is an excellent writer, but his writing is not only technically accurate it indicates a broader ability to detect and convey the heart of a project – its true significance. His ability to detect this aspect within a given scientific result is a skill I hope I have learned in some small way. Thank you for everything, Chad!

I would also like to very sincerely thank my committee, Prof. Mark Ratner and Prof. Sonbinh Nguyen, as well as Prof. George Schatz. Through their examples, I have learned how strong character is successfully expressed in science, teaching, and leadership. I cannot thank them enough for the time they have spent with me over the last five years—it has been invaluable. Thank you!

In addition to my gratitude to the faculty at Northwestern, I am incredibly grateful to the graduate students and researchers in the Mirkin group. Throughout my graduate work, I have been overwhelmed with gratitude for the dedicated, bright, fascinating, and hilarious members of our group. First and foremost, I thank Prof. Sungho Park. Sungho taught me how to think about my experiments, to work harder than you think is reasonable, and to “get the elephant in the refrigerator” – in short, Sungho taught me how to be a productive graduate student and scientist. His endless hours of work and wisdom did no less than make my Ph. D. possible. I also thank Dr. Dimitra Georganopoulou for her encyclopedic knowledge, patience, enthusiasm, and dedication. I continue to be grateful for her friendship and advice.

It is often said in these pages that, “I have had the privilege to work with…,” and I sincerely repeat it here: It has been an enormous privilege to work with great scientists over the last five years including Khalid Salaita, Wei Wei, Gabriella Métraux, Can Xue, Nat Rosi, Savka Stoeva, Max Ovchinnikov, Meisa Salaita, Aaron Brown, Dwight Seferos, David Giljohann, Pinal Patel, Jake Ciszek, Lidong Qin, Xiaodong Chen, Matthew Banholzer, Rafael Vega, Haley Hill, Sarah Hurst, Emma Kate Payne, Shad Thaxton, Weston Daniel, Monika Fischler, Matthew Jones, Josh Cutler, and Kyle Osberg. Their ideas, work, and humor have made my graduate career not only scientifically interesting but also fun. Thank you to Shuyou Li and Jinsong Wu in the Northwestern EPIC facility—I appreciate your time and patience! Thank you to Sabine Sturm for so much help and advice over the last few years.

I would like to give particular thanks to Lauren DeWitt for being with me through thick and thin. Thank you to James Graff and Sean Mintus who have opened my eyes so many times. Thank you so much to my great friends David Giljohann, Lisa Podgurski, Erin Purdy, Emma Kate Payne, Deedee Smith, Sarah Hurst, Haley Hill and Monica Canalizo.

I give special thanks to Matt Banholzer who, in addition to his intelligence, honesty, enthusiasm, humor, and tenacity, is the highest possible form of human being – engaged in the world and trying to evolve. BSTC, in addition to everything else you’ve done, I thank you most for so much happiness. I couldn’t and wouldn’t have wanted to do it without you.

Finally, I would like to thank my Dad, Mom, and sister, Chelsey. *Everything positive that I have accomplished is a product of your hard work, patience, love, and wisdom.* To my family, it is impossible to convey how grateful I am to be your daughter, sister, niece, and cousin. Thank you for opening my eyes to the world, encouraging me to learn wherever and from whomever possible, to follow my own path, to work hard, be honest and push on! I love you!

**TABLE OF CONTENTS**

ABSTRACT ..... 3

ACKNOWLEDGEMENTS ..... 6

LIST OF FIGURES ..... 11

CHAPTER ONE ..... 21

1.1 Motivation and Introduction ..... 22

1.2 What is the nanoscale? ..... 24

1.3 A Brief Overview of Noble Metal Nanoparticles ..... 25

1.4. What is a Triangular Nanoprism? ..... 28

1.5 Photochemical Syntheses of Triangular Nanoprisms ..... 33

1.5.1 Visible Light Methods ..... 33

1.5.2 Ultraviolet Light and Radiolysis ..... 42

1.5.3 Summary of Photochemical Routes ..... 45

1.6 Thermal Syntheses of (or Chemical Reduction Methods for Producing) Triangular Nanoprisms ..... 45

1.6.1 Thermal Syntheses in Aqueous Media ..... 46

1.6.2 Biological Thermal Syntheses. ..... 51

1.6.3 Microwave and Ultrasound Assisted Techniques ..... 54

1.6.4 Thermal Syntheses in Organic Media. ..... 56

1.6.5 Summary of Thermal Syntheses of (or Chemical Reduction Methods for Producing) Triangular Nanoprisms ..... 57

1.7 Mechanisms of Platelike Growth ..... 58

1.7.1 Crystallographic Arguments ..... 59

1.7.2 Chemical Methods and Redox Chemistry Arguments ..... 66

1.8 Dissertation Overview ..... 69

CHAPTER TWO ..... 72

2.1 Introduction ..... 73

2.2 Experimental ..... 74

2.2.1 Synthesis of Gold Nanoprisms ..... 74

2.2.2 Purification of Gold Nanoprism Reaction Solution ..... 76

2.3 Results and Discussion ..... 77

2.3.1 Empirical Characterization of Nanoprism Structure ..... 77
2.3.2 Characterization of Nanoprism Quadrupole Plasmon Resonance ..... 81
2.4 Conclusion ..... 85
CHAPTER THREE ..... 87
3.1 Introduction ..... 88
3.2 Experimental ..... 89
3.2.1 Method for the Growth of Nanoprism Edge Length ..... 89
3.3 Results and Discussion ..... 90
3.3.1 Growth Method and Nanoprism Optical Features ..... 90
3.3.2 Microscopy Analysis of Expanded Au Nanoprisms ..... 94
3.3.3 Crystallographic Characterization of Expanded Nanoprisms and Proposed Growth Mechanism ..... 96
3.4 Conclusion ..... 103
CHAPTER FOUR ..... 104
4.1 Introduction ..... 105
4.2 Experimental ..... 106
4.2.1 Preparation of Au Nanoprisms ..... 106
4.2.2 Preparation of Functionalization Buffers ..... 107
4.2.3 Functionalization of Au Nanoprisms ..... 108
4.2.4 UV-vis-NIR Spectrophotometry and TEM Analysis ..... 109
4.2.5 Hybridization and Melting Experiments ..... 109
4.2.6 Determining DNA loading on Au Nanoprism ..... 110
4.3 Results and Discussion ..... 111
4.3.1 Hybridization and Melting Behavior of DNA-Nanoprism Conjugates ..... 111
4.3.2 Quantification of DNA Loading on Nanoprism Surface ..... 114
4.3.3 Localization and Time-Dependence of DNA Adsorption ..... 115
4.4 Conclusion ..... 118
CHAPTER FIVE ..... 120
5.1 Introduction ..... 121
5.2 Experimental ..... 122

5.2.1 Preparation of Functionalization Buffers ..... 122
5.2.2 Preparation of DNA-Conjugated Au Nanodisk Arrays ..... 122
5.2.3 Hybridization Procedures for DNA Functionalized Nanorod/arrays ..... 123
5.2.4 Characterization by Raman Spectroscopy ..... 123
5.2.5 Characterization of DNA Loading on Au Nanodisk Array ..... 124
5.2.6 Preparation of Au Nanoprisms and Nanorods for Cellular Transfection ..... 124
5.3 Nanodisk Codes ..... 125
5.3.1 Nucleic Acid Detection using NDCs and AuNPs ..... 127
5.4 Cellular Uptake of Au Nanoprisms ..... 133
CHAPTER SIX ..... 137
6.1 Introduction ..... 138
6.2 Experimental ..... 139
6.2.1 Materials for Anisotropic Nanoparticle Synthesis ..... 139
6.2.2 Preparation and Recrystallization of Cetyltrimethylammonium Bromide (CTAB) ... 140
6.2.3 Synthesis of Anisotropic Gold Nanoparticles ..... 140
6.2.4 Synthesis of Ag Nanoparticles (AgNPs) ..... 142
6.2.5 ICP-MS Analysis ..... 142
6.2.6 XPS Analysis ..... 142
6.2.7 UV-vis-NIR Spectrophotometry and TEM Analysis ..... 143
6.3 Results and Discussion ..... 143
6.3.1 Role of Iodide ..... 143
6.3.2 Role of Seed ..... 149
6.4 Conclusion ..... 152
REFERENCES ..... 154
CURRICULUM VITAE ..... 162

# LIST OF FIGURES

**Figure 1.1.** Diagram illustrating the interdependence of nanoparticle properties on nanostructure size, shape, composition and dielectric environment..... 23

**Figure 1.2.** Rayleigh light-scattering of particles deposited on a glass microscopy slide. The slide is used as a planar waveguide, which is illuminated with a tungsten source. (Ref. 45)..... 24

**Scheme 1.1.** Illustration of nanoprism dimensions ..... 28

**Figure 1.3.** (A) STM image of a hexagonal gold nanoprisms showing the atomic terraces (The image has been high-pass spatial filtered, and the defect on the nanoprism surface was caused by a tip crash). (B) A high-resolution zoom on the surface of the nanoprism shown in A. The corrugation is the √3 √3 R30° molecular lattice characteristic of well-ordered alkanethiol SAMs. The dark features (arrow) are SAM structural domain boundaries. (The tunneling condition for both images are: -1 Vsample, 1 pA.) (Ref. 114)..... 30

**Figure 1.4.** UV-vis-NIR spectra and corresponding solutions of Ag nanoprisms with varying edge length. Labeled vial and spectra numbers correspond to the wavelength of irradiation used to prepare the nanostructures. (Ref. 48)..... 31

**Figure 1.5.** Orientation-averaged extinction efficiency for triangular nanoprisms based on a 100 nm edge dimension with snips of 0, 10, and 20 nm. The inset shows the shape of a snipped prism. The prism thickness is 16 nm. (Ref. 36)..... 32

**Figure 1.6.** (A) EELS mapping analysis showing the flat-top morphology of the Ag nanoprisms. Inset shows the EELS intensity over the line scan (dotted line through triangle axis). (B) Stacks of Ag nanoprisms assembled in a top-to-base manner. (C) Electron diffraction analysis of individual Ag nanoprisms. The diffraction pattern is characteristic of the [111] orientation of an

individual Ag nanoprism lying flat on the substrate with its triangular face perpendicular to the electron beam. On the basis of three-zone axis analysis (not shown), the crystal structure of the Ag nanoprism was determined to be an fcc structure. The intense spots in the [111] zone axis are allowed {220} Bragg reflections (e.g., circled spot, corresponding to the lattice spacing of 1.44), and the sharp weak spot in the center of the triangles formed by the strong spots is indexed as 1/3{422} (e.g., boxed spot, corresponding to the lattice spacing of 2.50). (Ref. 45) ..... 34

**Figure. 1.7.** (A) Time-dependent UV-Vis spectra showing the conversion of silver nanospheres to nanoprisms (a) before irradiation and after (b) 40, (c) 55, and (d) 70 hours of irradiation. (B) Corresponding extinction profiles at 670 nm as a function of time. (Ref. 45) ..... 35

**Figure 1.8.** The unimodal growth of nanoprisms using dual beam excitation. (A) Schematic diagram of dual-beam excitation. (B) The optical spectra (normalized) for six different-sized nanoprisms (1 – 6 edge length: 38 ± 7 nm, 50 ± 7 nm, 62 ± 9 nm, 72±8 nm, 95 ±11 nm and 120 ± 14 nm) prepared by varying the primary excitation wavelength (450, 490, 520, 550, 650 and 750 nm ± 40 nm, respectively;) coupled with a secondary wavelength (340 nm ±10 nm). (C) Edge length as a function of the primary excitation wavelength. (D-F) TEM images of Ag nanoprisms with average edge lengths of 38±7 nm (D), 72 ± 8 nm (E) and 120 ±14 nm (F). Scale bar applies to panels D-F. (Ref. 108) ..... 37

**Figure 1.9.** (A) A TEM image of the Au@Ag core–shell nanoprisms (average edge length of 70±6 nm) synthesized by irradiation with 550-nm light. The inset shows the side view of a core–shell nanoprism. (B) Extinction spectrum of the Au@Ag core–shell colloidal nanoprisms after centrifugation. (C) A high-resolution TEM image of the {111} face of the Au@Ag core–shell nanoprisms. The hexagonal lattice shows a spacing of 1.44 2, indexed as {220} of fcc Ag. (Ref. 107) ..... 40

**Scheme 1.2.** Proposed Photomediated Growth Pathway of Silver Nanoprisms from Spherical Nanoparticles (Ref. 122 ..... 42

**Figure 1.10.** Representative TEM images of Au@Ag core–shell nanoprisms with a gold prism core. The scale bar is the same for all images. (Ref. 107) ..... 41

**Figure 1.11**. (A) UV-visible spectrum measured from a dilute solution containing the particles shown in (B). (C) Diffraction pattern from a single Au nanotriangle with electron beam perpendicular to the {111} plane. The spot array indicates the [111] direction. (Ref. 134) ..... 47

**Figure 1.12.** (A) TEM image of Au spherical and triangular nanoparticles. (B) Zoom-in image. Inset shows the electron diffraction pattern of the top of a single prism. (C) Histogram of nanoprism edge lengths. (D) AFM image of nanoprisms on mica (tapping mode). Inset: height profile along the dashed lines. (Ref. 84) ..... 48

**Figure 1.13**. (A-D) FE-SEM images of gold nanoplates with edge lengths of varying size; Scale bar is 1 micrometer in all cases (e) UV-vis-NIR absorption spectra of the samples in panels (A-D). (F) Aspect ratio (width/thickness) as a function of the molar ratio of PVP to Au. (Ref. 81). 49

**Figure 1.14.** TEM images of stacked Ag nanoprisms showing the effect of $NaBH_4$ concentration on nanoprism thickness; (A) 0.30 mM, (B) 0.80 mM. Scale bars for both images correspond to 50 nm. (Ref. 106) ..... 50

**Figure 1.15.** UV–vis spectra recorded as a function of time of reaction of lemongrass extract with aqueous gold ions; curves 1–5 correspond to spectra recorded 1, 90, 160, 220 and 340 min after reaction. Curve 6:spectrum obtained from the purified gold nanotriangle solution; inset:UV–vis–NIR spectrum of a solution-cast film of purified gold nanotriangles obtained by reaction of $AuCl_4$-lemongrass extract solution on a quartz substrate. (B) Representative TEM

image of triangular gold nanotriangles by reduction of aqueous $AuCl_4$ by lemongrass extract. (Ref. 85) ..... 52

**Scheme 1.3.** Silver halide model for a single twinned plane. Alternating sides contain A-type and B-type faces. The reentrant grooves of the A-type faces causes rapid growth that is arrested when the face grows itself out, leaving a triangular prism with slow-growing B-type faces. (Ref. 103) ..... 61

**Figure 1.16** Time evolution of UV-visible spectra during the formation of Ag nanoprisms in DMF (Ref. 133). ..... 56

**Figure 1.17** (A) TEM image of the silver nanodisk taken in side view,showing the contrast from (111) stacking faults and a preferential growth along the stacking faults. The orientation relationship of the SAED pattern and the nanodisk is shown in Figure 3, parts A and B. (B) A typical SAED pattern of silver nanodisk at 100 kV in the [011] orientation (side view). (Ref. 171). ..... 63

**Figure 1.18** (A) HRTEM image of Au seeds I. (B) HRTEM images of Au nanorods grown from Au seeds I with Ag(I). The nanorods are aligned in [001] (left image) and [011] (right image) directions. The insets show 2x magnifications of the areas labeled by the black crosses. The dimensions of the insets are 2 x 5 nm for panel a and 2 x 4.6 nm for panel (C) HRTEM image of Au seeds II. Twinned planes are indicated by arrows. In the histograms (n = 150) S, T, and U stand for single crystalline, twinned, and unidentified nanoparticles, respectively. (D) TEM image of Au nanostructures grown from Au seeds II with Ag(I) (Ref. 78)..... 65

**Table 1.1**. Shapes of gold particles and corresponding reaction conditions. (Ref. 90)..... 68

**Figure 2.1.** (A) UV-Vis spectrum and (B) corresponding TEM image of gold nanoparticle seeds.. ..... 75

**Figure 2.2.** UV-vis-NIR spectra comparing solutions of filtered and unfiltered Au nanoprisms.. ..... 76

**Scheme 2.1.** Filtration of Au nanoprism solution using Whatman AAO filter with 100 nm pore diameters……..……..77

**Figure 2.3.** (A) TEM image of Au spherical and triangular nanoparticles. (B) Zoom-in image of nanoprisms. Inset shows the electron diffraction pattern of the top surface of a single prism. (C) Histogram showing the distribution of nanoprism edge lengths. (D) AFM image of nanoprisms on mica (tapping mode). Inset: height profile along the dashed lines.. ..... 79

**Figure 2.4.** In-situ UV-vis-NIR spectra following the formation of gold nanoprisms after seed addition.. ..... 80

**Figure 2.5.** (A) TEM image of the purified Au nanoprisms. (B) Corresponding UV-vis-NIR spectra of purified Au nanoprisms (**I**) and DDA calculation (**II**). Inset: the physical dimensions of a nanoprism used in the DDA calculation.. ..... 81

**Figure 2.6.** Theoretical extinction spectra for prisms of varying edge length and 7.5 nm heights. Intensities have been scaled to represent the relative populations of a solution that is comprised of 15% small prisms (edge length = 60 nm), and 85% large prisms (edge length = 150 nm). This ratio of particle sizes corresponds to an experimental solution before separation which is the upper limit of potential small prism concentration in these experiments. ..... 83

**Figure 2.7.** UV-vis-NIR spectra of Au nanoprism solution during aggregation by slow addition of NaCl.. ..... 85

**Figure 3.1.** UV-vis-NIR spectra of nanoprism solutions that have been grown to different edge lengths. Peaks **I** and **II** represent the dipole and quadrupole resonances of the gold nanoprisms, respectively. Peak **III** represents the dipole resonance of spherical nanoparticles..... 92

**Figure 3.2.** The change in quadrupole plasmon resonance λmax between successive pairs of grwth addition showing a strong, inverse linear relationship. Error bars represent 5 separate experiments ..... 92

**Figure 3.3.** TEM images of gold nanoprisms with increasing edge lengths (A) TEM image of gold nanoprisms made without additional growth (control sample). Inset shows diffraction pattern of the nanoprisms. (B) TEM image of nanoprisms after 2 growth additions (**x2**). Inset shows diffraction pattern of **x2** prisms. (C) TEM image of **x4** nanoprisms, (D) **x6** nanoprisms, and (E) **x8** nanoprisms ..... 93

**Figure 3.4.** Histograms representing the size distribution of nanoprisms grown to different average edge lengths. ..... 95

**Figure 3.5.** Plot of quadrupole plasmon resonance $\lambda_{max}$ vs. average nanoprism edge length of the corresponding nanoprisms. The linear regression analysis shows a strong, positive correlation between the two. ..... 97

**Figure 3.6.** (A) HRTEM image of **x4** nanoprisms using EELS where contrast uniformity indicates thickness uniformity. Arrows highlight the contrast between faceted and flat particles. (B) TEM image of **x4** nanoprisms turned sideways showing prism thickness. (lines across (B) are from the Formvar coating of the Cu grid used for immobilization of nanoprism sample)..... 98

**Scheme 3.1.** The two equations represent the competing reactions during the particle growth process. When given amounts of Au ions and reducing agent are added stepwise, $rate_2 < rate_1$. However, when the same amount is added “all-in-one”, $rate_2 > rate_1$.. ..... 99

**Figure 3.7.** TEM image illustrating the primarily polyhedral geometry of the pseudo-spherical nanoparticles.. ..... 99

**Scheme 3.2.** Illustration of a twinned fcc nanocrystal, and the possible mechanism for platelike growth from such a structure. A polyhedral nanoparticle is shown for comparison.. ..... 101

**Figure 3.8.** Diffraction patterns of nanoprism faces. (A) Hexagonal pattern indicates the (111) crystal surface. The orange circle highlights the presence of forbidden reflections. (B) Rectangular pattern is consistent with the {112} crystal surface of an fcc structure. ..... 101

**Figure 3.9.** (A) UV-vis-NIR spectra of nanoprism solutions regrown at 4 and 8 weeks after their initial synthesis. Peak I and Peak II are the dipole and quadrupole plasmon resonances of gold nanoprisms, respectively. Peak III is the dipole resonance of spherical nanoparticles. (the small spike at 840nm is due to the grating changeover of the spectrophotometer when moving into the visible light range) (B) TEM images of nanoprisms grown at 4 weeks and (C) 8 weeks. ..... 102

**Scheme 4.1.** Process of determining oligonucleotide loading on Au nanoprisms. ..... 111

**Figure 4.1.** (A) Melting profile of Au nanoprism-DNA conjugates solution monitored at 1250 nm (dipole SPR of gold nanoprisms, blue) and 532 nm (dipole SPR of 40 nm gold nanoparticles, black). Inset: first derivative of melting transition at 1250 nm; Tm = 60.1$^{o}$C; FWHM = 2.4$^{o}$C (B) TEM image of nanoprism-DNA conjugates after melting. (C) UV-vis-NIR spectra of nanoprism conjugates. (D) Phase transitions of DNA-functionalized gold nanoprisms. ..... 113

**Figure 4.2.** XPS spectrum of DNA-nanoprisms showing the presence of sulfur, phosphorous, and nitrogen on the nanoprism surface. ..... 114

**Table 4.1.** Compares theoretical and experimental values for DNA loading on Au nanoprisms and 80 nm Au nanoparticles. The calculations are based on 17 nm$^2$ footprint for the DNA molecule on the gold nanoprisms surface and a 15 nm$^2$ footprint for the 80 nm nanoparticles;

these footprints account for the differences in surface curvature between the two structures….115

**Figure 4.3.** Correlation of time with DNA loading on nanoparticle surface. (Error bars indicate 5 independent experiments.). ..... 116

**Figure 4.4.** TEM images from experiments using asymmetrically functionalized AuNPs as surface functionalization probes. (A) Nanoprisms functionalized for 4 hours (B) 12 hours (C) 24 hours and then hybridized with AuNPs (13nm) that were asymmetrically functionalized with complementary ssDNA. (D) Phosphorous EELS analysis of Au nanoprism surface. The graph shows the signal of phosphorous as a function of distance. Inset is a STEM image of the nanoprism analyzed; the green line indicates the area at which each spectrum was taken. ..... 118

**Figure 5.1.** (A) Scheme of NDC synthesis and functionalization; (B) 13 possible 5-disk-pair NDCs with corresponding binary codes. (C) Two (top) and three-dimensional (middle) scanning Raman microscopy images of a 11111 NDC. Representative Raman spectrum of methylene blue (bottom) taken from the center of the hot spot generated in the middle disk pair shown in the Raman maps above.. ..... 128

**Figure 5.2.** (A) Schematic representation of three-strand DNA system, including DNA sequences used in these experiments. (B) 3D scanning Raman images of DNA detection results at target concentrations of 50 pM, 5 pM, and control with no target (top to bottom, respectively). All three images are graphed with the same z-scale. The control experiment (with only reporter and NDC strands, and no target) does not give any readable response. (C) A representative Raman spectrum taken from 3D spectra in (B) ..... 129

**Figure 5.3.**NP-target-NDC sandwich assay. (A) Three-dimensional scanning Raman image of 11011 NDC after functionalization with ssDNA and hybridization with 100 fM target concentration and reporter NPs. (B) FE-SEM image of NPs immobilized on disk-pair surface. ..... 130

**Figure 5.4.** Multiplexing with NDCs. (A) Scheme of 11011 and 10101 NDC nanostructures showing DNA sequences of target, reporter, and NDC strands. (B) Full-spectrum 3D scanning Raman image of 11011 and 10101 disk codes functionalized with different single-stranded DNA sequences. (C) Filtered Raman image of (B) where the transmitted frequencies are indicated by the blue bar in (E), corresponding to a unique Raman band from the Cy5 reporter (525.2-592.4 $cm^{-1}$). (D) Filtered Raman image of B) where the transmitted frequencies are indicated by the red bar in (a), corresponding to a unique Raman peak from the TAMRA reporter (1630.0-1679.0 $cm^{-1}$). (E) Raman spectra of Cy5 and TAMRA from reporter DNA sequences immobilized on NDC after DNA hybridization. N.B. (C,D) are taken with only a fraction of the total Raman signal being collected; the three images in (B-D) do not have the same *z*-scale and have been normalized for a straightforward comparison..... 132

**Figure 5.5.** Confocal microscope images showing fluorescence signals from 3 different cell lines, transfected with 3 different concentrations of Au nanoprisms. The volumes at the top of the image correspond to 0.25, 0.5, and 1.0 pM Au nanoprisms, respectively..... 134

**Figure 5.6.** TEM images of HeLa cell transfected with DNA-functionalized Au nanoprisms. Left image is a magnified view of the vesicle containing nanoprisms..... 135

**Table 6.1**. Iodide Concentrations of Reagents Used in Syntheses as Analyzed by ICP-MS…...140

**Figure 6.1.** UV-vis-NIR spectra of nanoparticles produced using 5 different CTABr batches. Each CTABr was used as received from the manufacturer.. ..... 144

**Figure 6.2.** (A) UV-vis-NIR spectra of nanoparticles made using various concentrations of I-, and corresponding TEM images of (B) pseudo-spherical nanoparticles, (C) nanorods, and (D) nanoprisms.. ..... 145

**Figure 6.3.** UV-vis-NIR spectra of nanoprism solutions made using 50 µM concentrations of LiI, NaI, and KI. Each batch shows the characteristic dipole and quadrupole plasmon resonances of Au nanoprisms.. ..... 147

**Figure 6.4.** XPS spectra (A) of gold nanoprisms; arrow indicates I- signal; (B) centered at binding energy of I- and taken from nanoprisms, rods, and pseudo-spherical nanoparticles. Spectra indicate I- only on nanoprisms..... 147

**Figure 6.5.** Powder XPS Spectra of CTABr batches showing no presence of iodide.. ..... 147

**Figure 6.6.** Characterization of CTABr-based, seed-mediated nanoparticle synthesis using 13 nm Au nanoparticle seeds. The UV-vis-NIR spectrum shows no spectroscopically discernable anisotropic nanoparticle formation. However, TEM and SEM analysis reveal significant populations of very large (> 1µm) hexagonal and triangular nanoplates. The TEM image in the upper right shows two overlapping nanoplates which exhibit Moiré fringes and indicate that the plates are single crystalline. ..... 150

**Figure 6.7.** Characterization of CTAB-based, seed-mediated nanoparticle synthesis using 5 nm Ag nanoparticle seeds. The UV-vis-NIR spectrum shows the characteristic spectrum of triangular platelike structures, which is confirmed by TEM. The bottom row shows statistical analysis of the size and shape distribution of the resulting nanoparticle products.. ..... 151

# CHAPTER ONE

Gold and Silver Triangular Nanoprisms

Portions of this chapter have been submitted for publication in: *Small*, **2008.**

## 1.1 Motivation and Introduction

The field of nanoscience and technology is driving the discovery of new physical and chemical phenomena, and is providing the basis for many promising technologies including applications in electronics[1-4], catalysis[5-12], diagnostics[13-24], and therapeutics.[24-28],[29] Although nanoscience and technology create and investigate structures that are extremely small, research has shown that the nano size regime is not just a miniaturization of the macroscopic world; it can be wholly different.[30, 31],[8, 32-36] For example, materials can exhibit size- and shape-dependent optical features,[34, 36, 37] relatively inert metals can become catalytic,[8, 10, 12, 38] and mechanical properties can be dramatically improved.[39, 40],[41] (Figure 1.1). Therefore with each new nanomaterial and nanoscale property elucidated, our scientific insights and technological capabilities expand – sometimes immensely.[32, 39, 42, 43] These advances have created enormous enthusiasm for nanoscience and nanotechnology[29] and encouraged the involvement of scientists in fields ranging from medicine to physics. However, numerous challenges exist for the nanoscience community regarding how to create, characterize, and understand nanoscale structures. In particular, elucidation of nanoscale structure-function relationships, high-resolution chemical and physical analysis, and nanomaterial synthesis are each the subject of numerous research projects, proposals, and initiatives.[44] The motivation for this thesis is to address both nanomaterial synthesis and structure-function relationships as they relate to nanocrystal shape.

As might be inferred from the defining influence of nanoparticle size, nanoparticle shape can be a critical factor in determining nanoparticle behaviors. For example, researchers have shown that the shape of a nanostructure can dramatically influence nanoparticle optical features, electronic behavior, and surface reactivity.[34-36, 45] The effects of material shape at the nanoscale emphasize the relationship between nanostructure morphology and behavior as a central theme

of nanoscience. It follows that nanomaterial synthesis is at the foundation of nanotechnology research, as it produces the structures from which all properties will be observed and used. Currently, approaches to nanomaterial synthesis are categorized as either "bottom-up" methods which refer to approaches that synthesize materials atom by atom or as "top-down" approaches where materials are constructed by manipulating prefabricated structures. Using top-down techniques, it is relatively simple to design and manipulate a wide variety of nanostructures with high yield and monodispersity,[46, 47] However, these techniques can be limited in both throughput and resolution. On the other hand, bottom-up strategies are easily scaled, theoretically have atomic level resolution, and are materials general.[8, 34] Yet, bottom-up techniques can be low yielding, unreliable, and produce non-homogenous products. In order to achieve directed nanocrystal growth from the bottom up, it is necessary to understand the atom by atom development of nanoscale materials, and how size and shape influences nanoparticle behavior. This thesis will address these questions and demonstrate insights into the origins, influences, and applications of nanoparticle shape using a model system of triangular gold nanoprisms.

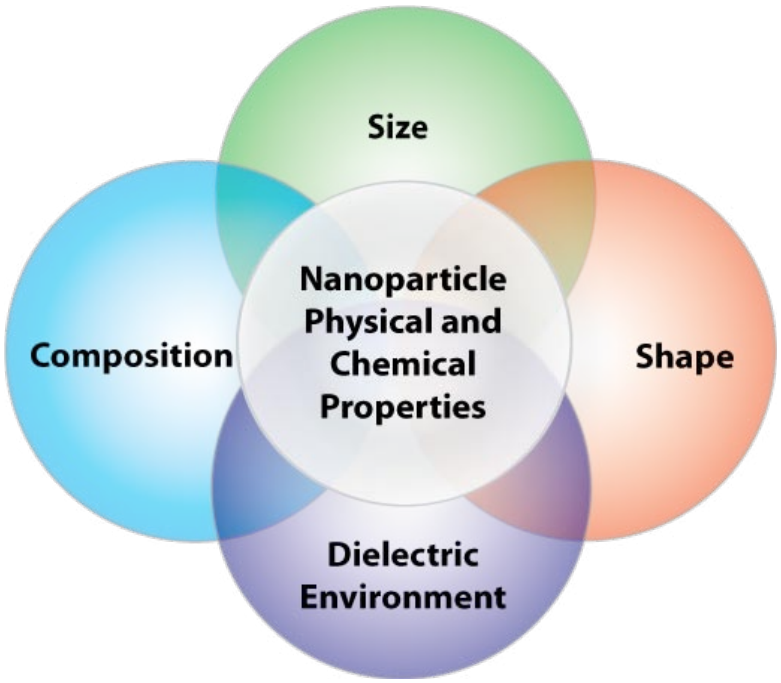


**Figure 1.1** Diagram illustrating the interdependence of nanoparticle properties on nanostructure size, shape, composition and dielectric environment.

**1.2 What is the nanoscale?**

Typically, the nanoscale is defined as 1 – 100 nm, and nanomaterials are structures with at least one dimension within this size range. Many materials developed and investigated in nanoscience are derived from previously well-studied materials such as noble metals and semiconductors. Yet, nanomaterials made from these materials often exhibit previously unobserved characteristics that correlate not only with their chemical composition, but also with their size and shape. This structure-function relationship is at the heart of nanotechnology, and it drives the intense interest in synthesizing nanoparticles in a variety of sizes and shapes. Indeed, one nanomaterial, when defined in terms of composition, can exhibit a wide variety of useful, size and shape-dependent properties. For example semiconductor nanoparticles, or "quantum dots" (QDs) exhibit a rainbow of optical emissions dependent only on their diameter, as do their

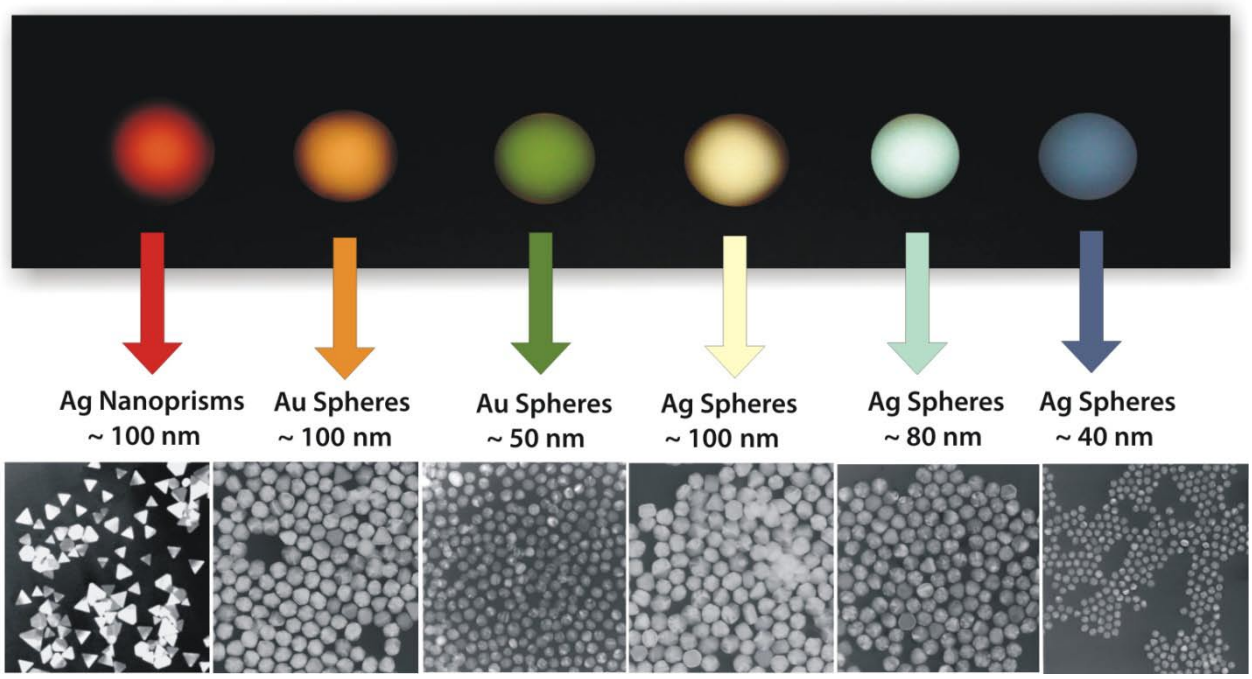


**Figure 1.2** Rayleigh light-scattering from nanoparticles deposited on a glass microscope slide. The slide is illuminated with a tungsten light source. (Ref. 45)

noble metal counterparts (*vide infra*) (Figure 1.2).[32, 48] Noble metal nanoparticles ( d > 5 nm) are particularly attractive materials, because of their visible and near-infrared (vis-NIR) optical features, well-studied surface chemistries, and relatively low toxicity.[8]

### 1.3 A Brief Overview of Noble Metal Nanoparticles

Given the size and shape dependant characteristics of noble metal nanoparticles, as well as their demonstrated utility, it is no surprise that there has been an explosion of interest in the development of synthetic methods for preparing these nanostructures and in the investigation of their properties. The majority of research effort to date has focused on isotropic (i.e. spherical or pseudo-spherical) nanoparticles, and many synthetic pathways have been developed for preparing them with various compositions (e.g., Au,[49-52] Ag,[53, 54] Pt,[55, 56] Pd[57]) and with narrow size distributions. Nanoparticles derived from these protocols have fostered the study of their optical,[36, 58-60] structural,[61, 62] catalytic,[7, 10, 12, 63] and electronic[1, 2, 12, 64] properties with respect to both size and composition. For example, 40 nm diameter Au nanoparticles (AuNP) have a molar absorption coefficient almost five orders of magnitude higher than a conventional organic dye absorbing at a similar wavelength (e. g. 7.66 x $10^9$ $M^{-1}$ $cm^{-1}$ at $\lambda_{max}$ = 528 nm for 40 nm Au nanoparticles vs. 1.16 x $10^5$ $M^{-1}$ $cm^{-1}$ at $\lambda_{max}$ = 530 nm for rhodamine-6G).[65] Gold nanoparticles with diameters less than 10 nm and immobilized within a metal oxide framework can catalyze CO oxidation or propylene epoxidation, even at low temperatures (< 0°C), whereas bulk gold is essentially inactive.[66] In another example, both Ag and Au nanostructures can significantly influence fluorescence processes by enhancing or quenching fluorophore emission as a function of the distance between the fluorophore and the metal surface.[67] Bulk gold only acts as a quencher. With these insights, scientists have begun to incorporate isotropic metal nanoparticles into a wide variety of applications including ultrasensitive detection assays,[14, 16, 18-

[24, 68, 69] catalysis,[7, 12, 63] electronics,[1, 12] encryption,[70-72] and gene regulation.[25, 73, 74] Yet in the case of gold and silver, although researchers have developed a reasonable understanding of the relationship between the properties of a particle and its size and composition, they are just beginning to explore the relationship between the shape of a nanoparticle and its physical and chemical properties.

Many Au and Ag nanoparticle shapes have been observed by electron microscopy and related methods, including rods and wires,[75-80] prisms and disks,[45, 81-85] cubes,[86-90] "dogbones,"[91] and hollow structures.[92, 93] However, there are relatively few methods that allow one to systematically make such structures in high yield with control over their architectural parameters. Indeed with respect to Au and Ag, there are three classes of anisotropic structures where there are reliable methods for making them in high yield with moderate to excellent control over architectural parameters: rods, "platonic solids", and triangular prisms.

Nanorods can be made by thermal,[79] photochemical,[94] and electrochemistry-based template[95] methods. In fact, template-based methods for preparing nanorods marked one of the first major developments in high yield, solution-phase anisotropic metallic nanostructure synthesis,[96, 97] and they are extraordinarily useful for synthesizing structures with control over both rod diameter and length, and have been investigated in numerous photonic, plasmonic, and electronic applications.[98] In the last decade, another class of materials called "platonic solids", which include cubic- and icosohedral- shaped particles, have been developed. Methods for preparing these Ag and Au versions of these structures were pioneered by both Yang and Xia using different but complementary polymer-based thermal strategies, wherein the nanoparticle shape could be controlled by such parameters as metal precursor to reducing agent ratios and seed particle type.[99, 100] These particles exhibit optical features between 600 – 1000 nm,

depending on their morphology, and are another example of using solution phase synthetic methods to control nanoparticle shape and corresponding properties. The third class of Ag and Au anisotropic nanoparticles to be extensively investigated is triangular prisms and plate-like nanostructures. These particles were observed by electron microscopy as components of complex mixtures as far back as 1951,[101] but our group developed and reported the first high yielding synthetic method for this particle type in 2001.[45] Importantly, we were able to assign the surface plasmon resonance (SPR) bands in the optical spectra of these colloids by correlating the experimental data with theoretically predicted values.[45] Since this initial work, many methods have been developed for making prismatic structures in high yield and research conducted on these nanostructures has been extensive. In particular, research has focused on determining mechanisms for describing their formation and developing methods to manipulate their optical features.[34, 79, 80, 99, 102-104]

This introduction will focus on methods for synthesizing and characterizing Au and Ag triangular nanoprisms. These structures are especially interesting because they have plasmonic features in the visible and infrared, can be prepared in high yield, and can be readily functionalized with a variety of sulfur-containing adsorbates.[45, 48, 84, 104-108] To organize a discussion of these structures, nanoprisms will first be defined as a function of their architecture and optical features. Next, photochemical, thermal, and biological routes for synthesizing these structures will be considered along with the characterization of the resulting nanoparticle products. Finally, theories of nanoprism formation will be discussed, and an outlook for anisotropic nanoparticle syntheses will be presented.

**1.4. What is a Triangular Nanoprism?**

A variety of synthetic routes can be used to generate prismatic, platelike nanostructures (also referred to as, "nanoprisms," "nanotriangles," "nanoplates," or "nanodisks"). However, despite the differences in the methods used to make them, the resulting structures share common architectural elements and possess similar chemical and physical properties. This section highlights these features and formulates a definition of structures that are commonly categorized as "nanoprisms". We will discuss these points specifically in relation to particles composed of pure gold and pure silver.

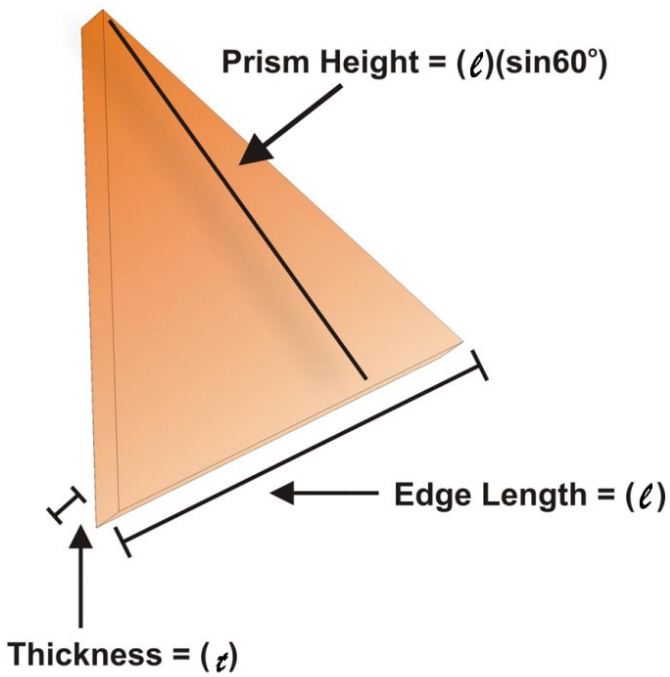


**Scheme 1.1** Illustration of nanoprism dimensions.

From a geometric perspective, prisms can be of any thickness (i. e. have an arbitrary distance between two parallel polygons), but in general, nanoprisms synthesized to date have been flat, triangular, hexagonal, or circular plates with large aspect ratios (*vide infra*) (Scheme 1.1). This review focuses on triangular nanoprisms, which exhibit three congruent edge lengths (ℓ) and a defined thickness (*t*). These Au and Ag nanoprisms typically exhibit edge lengths in the ~ 40 nm to 1 µm range and thickness ranging from ~ 5 to 50 nm. Nanoprism structures with edge lengths as large as several microns have been synthesized, but these have not exhibited the optical or chemical properties associated with their smaller analogues.[36, 109, 110] Technically,

triangular nanoprisms contain three sharp vertices or “tips” which contribute significantly to their optical and electronic properties.[36, 110] However in practice, mixtures of particles with varying degrees of tip truncation and rounding make up a colloid. When significant rounding occurs, structures are no longer described as triangular nanoprisms, and generally are referred to as nanodisks or in cases of truncation without rounding, hexagonal nanoprisms. In fact, all colloidal syntheses of triangular nanoprisms tend to yield some percentage of nanohexagons or nanodisks, which have either undergone incomplete transformation to triangular nanoprisms or have been undergone surface reorganization in such a way that they no longer exhibit the ideal triangular nanoprism structure.

In some cases, nanoprism dimensions can be controlled *in situ* by adjusting experimental parameters, including metal ion and reducing agent ratios,[106] surfactant concentrations,[90] pH,[48] irradiation wavelength,[108] seed particle concentration and type[81, 100, 104] . The edge lengths and thickness of the nanoprism determine its aspect ratio ($\ell/t$), which can be used to quantify degree of anisotropy. For example, isotropic nanoparticles such as pseudo-spherical particles have an aspect ratio of one because their dimensions are roughly the same in all directions. In the case of gold and silver nanoprisms, their aspect ratios vary from 5 to over 40.

In general, solution-prepared gold and silver triangular nanoprisms are single crystalline with face-centered cubic (*fcc*) lattice structures.[45, 48, 85, 104, 111-113] This crystallinity differentiates them from lithographically or electrochemically prepared structures, which are typically polycrystalline. The triangular (or hexagonal or circular) facets of solution synthesized nanoprisms are often composed of almost atomically flat {111} crystal faces (Figure 1.3).[84, 114] The edges of the nanoprisms are typically {110}, {112} or {100} facets,[45, 104] and HRTEM

analysis suggests that nanoprisms contain a twin plane parallel to their {111} triangular faces

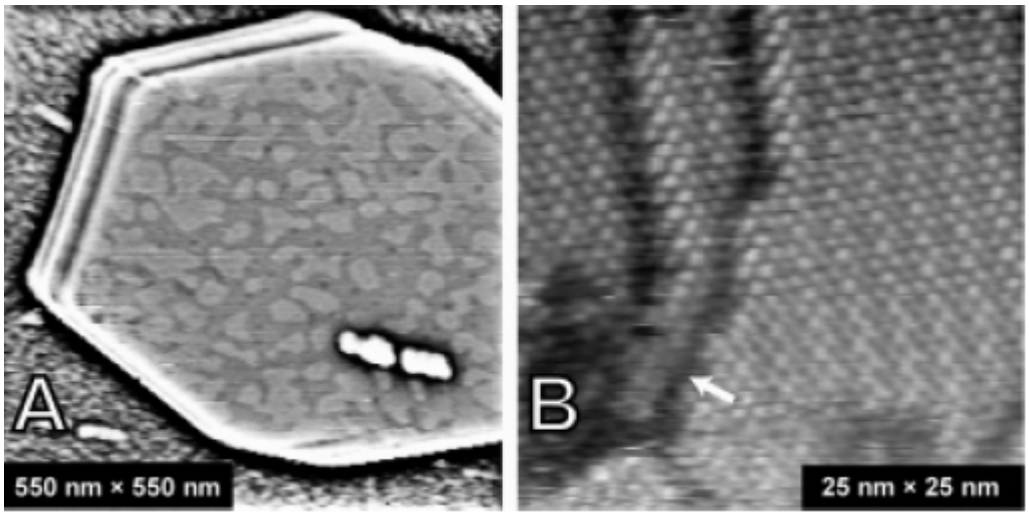


**Figure 1.3** (A) STM image of a hexagonal gold nanoprisms showing atomic terraces (the image has been high-pass spatial filtered, and the defect on the nanoprism surface was caused by a tip crash). (B) A high-resolution zoom on the surface of the nanoprism shown in (A). The corrugation is the $\sqrt{3}\times\sqrt{3}$ R30° molecular lattice characteristic of ordered alkanethiol SAMs. The dark features (white arrow) are SAM structural domain boundaries. (The tunneling condition for both images are: -1 V sample, 1 pA.) (Ref. 114)

(*vide infra*). [45, 103, 104]

These common architectural elements give rise to a set of chemical and physical properties that are shared by most gold and silver triangular nanoprisms. In particular, these prisms have SPRs that are tunable throughout the visible and near-IR spectrum by controlling nanoprism edge length, thickness, and tip morphology (Figure 1.4).[36, 45, 48, 104, 106, 108, 110] These SPRs are generated by the coherent oscillation of conduction electrons at the surface of the nanoparticle when they interact with the oscillating electric field of incident light. The frequency of this oscillation is not only dependent on the density and effective mass of the electrons, but also the size and shape of the charge distribution (Figure 1.5).[36] Further, Schatz and coworkers have used a quasi-static approximation model to show that optical properties of metal

nanoparticles are significantly affected by the wavelength-dependent dielectric constant of the particle and the dielectric constant of the surrounding medium when the particle diameter is much smaller than that of the incident light.[36, 110] The dependence of nanoparticle surface plasmon resonances on charge distribution and dielectric properties explains the sensitivity of their optical features to particle size, shape, and chemical environment, and is a highly useful feature of Au and Ag nanoprisms (*vide infra*).

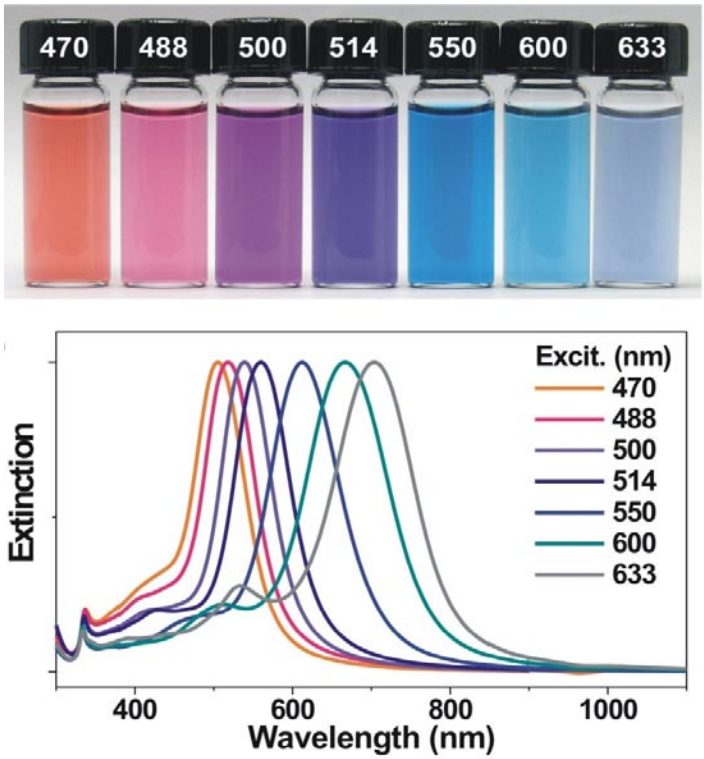


**Figure 1.4** UV-vis-NIR spectra and corresponding solutions of Ag nanoprisms with varying edge length. Labeled vial and spectra numbers correspond to the wavelength of irradiation used to prepare the nanostructures. (Ref. 48)

Sufficiently large and thin nanoprisms (aspect ratio > 10)[110] contain both dipole and quadrupole plasmon resonances that shift in frequency and extinction cross-section as a function of nanoprism size, shape, and dielectric environment as described above. With spherical particles, these two modes (quadrupole and dipole) are not distinguishable from one another,[115] however in an anisotropic particle such as a nanoprism, these modes oscillate at markedly different frequencies (generally separated by 100 - 400 nm), and can be resolved experimentally for prisms of both Au and Ag.[45, 84] Roughly, these modes originate from the degree and direction of polarization of the electron cloud relative to the incident electric field. In

this way, a dipole plasmon resonance can be described as the electron cloud surrounding the nanoparticle moving either parallel or anti-parallel to the applied field. For a quadrupole mode, half of the cloud moves parallel and half moves anti-parallel. Higher-order surface plasmon resonance modes can be obtained through more complex polarizations, and have been observed for high aspect ratio nanostructures such as nanorods.[116]

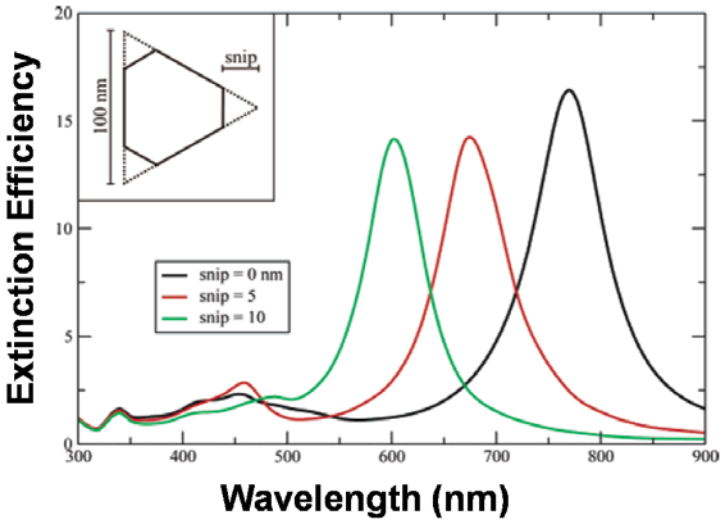


**Figure 1.5** Orientation-averaged extinction efficiency for triangular nanoprisms based on a 100 nm edge dimension with snips of 0, 10, and 20 nm. The inset shows the shape of a snipped prism. The prism thickness is 16 nm. (Ref. 36)

Given the relationship between nanoparticle morphology and nanoparticle optical features, it follows that these features can be used to assess the shape, size, and distribution of nanostructures in solution for structures that exhibit such properties.[84] For example, as the tips of a nanoprism become rounded, its optical features become blue-shifted (to shorter wavelengths) as the electron cloud density changes across the particle surface.[36] Prism thickness, edge length, and dielectric environment will also red- or blue-shift the SPRs depending on the change in particle architecture or environment.[36, 48, 104-106, 108, 110] Of particular interest are the quadrupole plasmon modes of the nanoprisms, because these modes can only be identified for colloidal dispersions with sufficiently high concentrations of nanoprisms that also have relatively narrow particle size and shape distributions (approximately < 20 %).[36, 48, 104-106, 108, 110] Indeed, one of the best diagnostics for the quality (in terms of shape and monodispersity)

of triangular prisms produced in a synthetic procedure is the identification, breadth, and spectral position of the dipole and quadrupole SPRs in the extinction spectrum of the colloid. Throughout this review, these optical features, in conjunction with electron microscopy, will be used to compare the various products of Au and Ag nanoprism syntheses.

### 1.5 Photochemical Syntheses of Triangular Nanoprisms

A photochemical route was the first reliable and high yielding method for making solution-phase triangular Ag nanoprisms.[45] This method, which allowed one to control edge length with excitation wavelength, allowed researchers to assign UV-vis spectral features as a function of prism architecture.[45] Therefore, our discussion of nanoprisms begins with photochemical syntheses and related methods that have been developed to make these nanostructures using light. Approaches to nanoprism synthesis using irradiation have been classified by the radiation wavelength employed in the synthesis.

#### 1.5.1 Visible Light Methods

This section highlights the use of visible light (300 nm < λ < 800 nm) to direct and/or drive the growth of prismatic nanoparticles. In 2001, our group reported a photochemical reaction in which small silver nanoparticles (diameter = 6 – 8 nm) could be converted into triangular nanoprisms by irradiating a solution containing trisodium citrate, and bis(*p*-sulfonatophenyl)phenyl phosphine dipotassium salt (BSPP) with fluorescent light.[45] The resulting colloid contained single crystalline Ag nanoprisms with edge lengths of ~ 100 nm (Figure 1.6). The conversion of the nanoparticles to nanoprisms could be turned on and off simply by turning on or off the light source. Interestingly, the optical spectrum displayed SPR bands that had never been observed experimentally. In addition to the in-plane dipole resonance

at 670 nm, two new bands: the in-plane quadrupole (440 nm) and the out-of-plane quadrupole (340 nm) were identified (Figure 1.7). In a collaborative effort with our group, Schatz and co

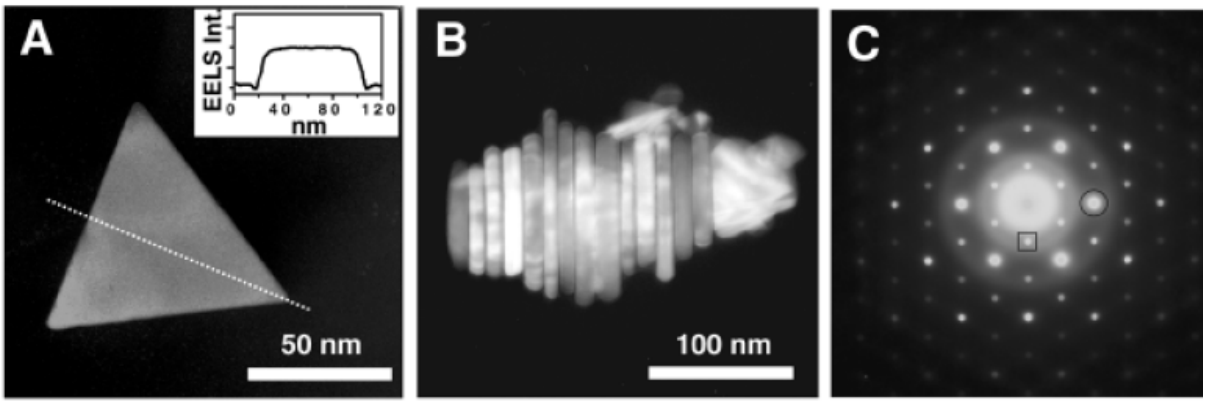


**Figure 1.6** (A) Electron energy loss spectroscopy (EELS) mapping analysis showing the flat-top morphology of the Ag nanoprisms. Inset shows the EELS intensity over the line scan (dotted line through triangle axis). (B) Stacks of Ag nanoprisms assembled in a top-to-base manner. (C) Electron diffraction analysis of individual Ag nanoprisms. The diffraction pattern is characteristic of the [111] orientation of an individual Ag nanoprism lying flat on the substrate with its triangular face perpendicular to the electron beam. On the basis of three-zone axis analysis (not shown), the crystal structure of the Ag nanoprism was determined to be an fcc structure. The intense spots in the [111] zone axis are allowed [220] Bragg reflections (e.g., circled spot, corresponding to the lattice spacing of 1.44), and the sharp weak spot in the center of the triangles formed by the strong spots is indexed as 1/3[422] (e.g., boxed spot, corresponding to the lattice spacing of 2.50). (Ref. 45)

workers calculated the optical signatures of these nanoprisms and found that the theoretically-derived spectra agreed closely with those obtained experimentally.[36, 45]

The role of light in this photochemical conversion process was more thoroughly examined in subsequent work,[108] which demonstrated the effects of photo-exciting a Ag nanoparticle colloid with wavelengths that overlap the dipole and quadrupole SPR modes of the final Ag nanoprisms. Interestingly, excitation of a silver nanoparticle colloid (AgNP) with a single wavelength (i.e. 550 nm, dipole SPR excitation) resulted in a solution of nanoprisms with two size distributions, designated Type 1 (edge length 70 ± 12 nm) and Type 2 (edge length 150 nm ± 16 nm). Type 1 and 2 nanoprisms differed only in edge length (by a factor of 2) whereas

their thickness was essentially the same. In contrast, simultaneous excitation with 550 nm (dipole SPR excitation) and 450 nm (or 340 nm, quadrupole SPR excitation) resulted in Type 1 nanoprisms only. Indeed, the results indicated that quadrupole or high energy excitation inhibits the fusion of the smaller, Type 1 prisms. Interestingly, by varying the primary beam (used for dipole excitation) over the visible range (450 – 750 nm), we were able to generate nanoprisms with edge lengths ranging from ~ 40 to 120 nm (Figure 1.8). The optical properties of the nanoprisms vary significantly with their dimensions and thus the colloidal solutions range in color from red to blue depending on nanoprism edge length. With this advance, one not only could prepare these unusual structures in high yield, but also could have unprecedented control of edge length, one of their key architectural parameters.

Since the initial report Ag triangular nanoprism synthesis, others have confirmed the results and significantly expanded upon their scope. For example, Brus and co-workers observed morphological changes of spherical Ag nanoparticles to nanoprisms when exposed to various wavelengths of visible light.[117] In this protocol, pseudo-spherical Ag seeds were prepared

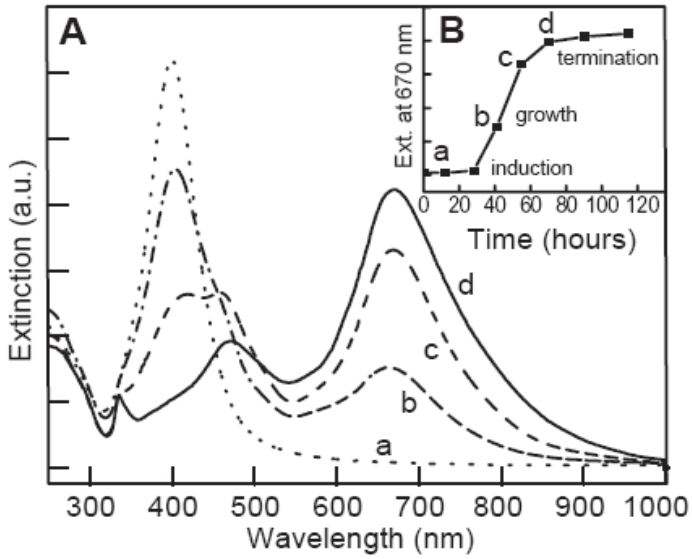


**Figure 1.7** (A) Time-dependent UV-Vis spectra showing the conversion of silver nanospheres to nanoprisms (a) before irradiation and after (b) 40, (c) 55, and (d) 70 hours of irradiation. (B) Corresponding extinction profiles at 670 nm as a function of time. (Ref. 45)

and added to an aqueous growth solution containing $Ag^+$ ions and trisodium citrate. This mixture was then irradiated with 457 nm light for several hours (power = 0.8 W/cm$^2$). The UV-vis spectrum of this solution exhibited three peaks at 338 nm (out-of-plane quadrupole), 400 nm (in-plane quadrupole), and 540 nm (in-plane dipole), indicating the formation of disk like nanoprisms. TEM analysis showed that these nanoprisms were single crystalline, approximately 38 nm in diameter and ~ 10 nm in thickness on average. When this reaction was monitored over time using TEM, the authors observed increasing numbers of nanoprisms with increasing exposure time. Similar to earlier work,[108] the disk diameter of the final nanoprisms increased with longer excitation wavelengths.

In their report, Brus *et al.* propose that the initial silver nanoparticles absorb light isotropically, resulting in a single surface plasmon resonance band at ~ 395 nm. Over time, silver clusters are reduced onto the surface of the nanoparticle, following Ostwäld ripening kinetics, causing the average size of the nanoparticles to increase. However, silver plating does not always occur uniformly on the nanoparticle surface at which point ellipsoidal shapes can be found in the colloid. The surface plasmon resonance band of non-isotropic nanoparticles splits into transverse and longitudinal modes. The longitudinal plasmon shifts to longer wavelengths (excitation

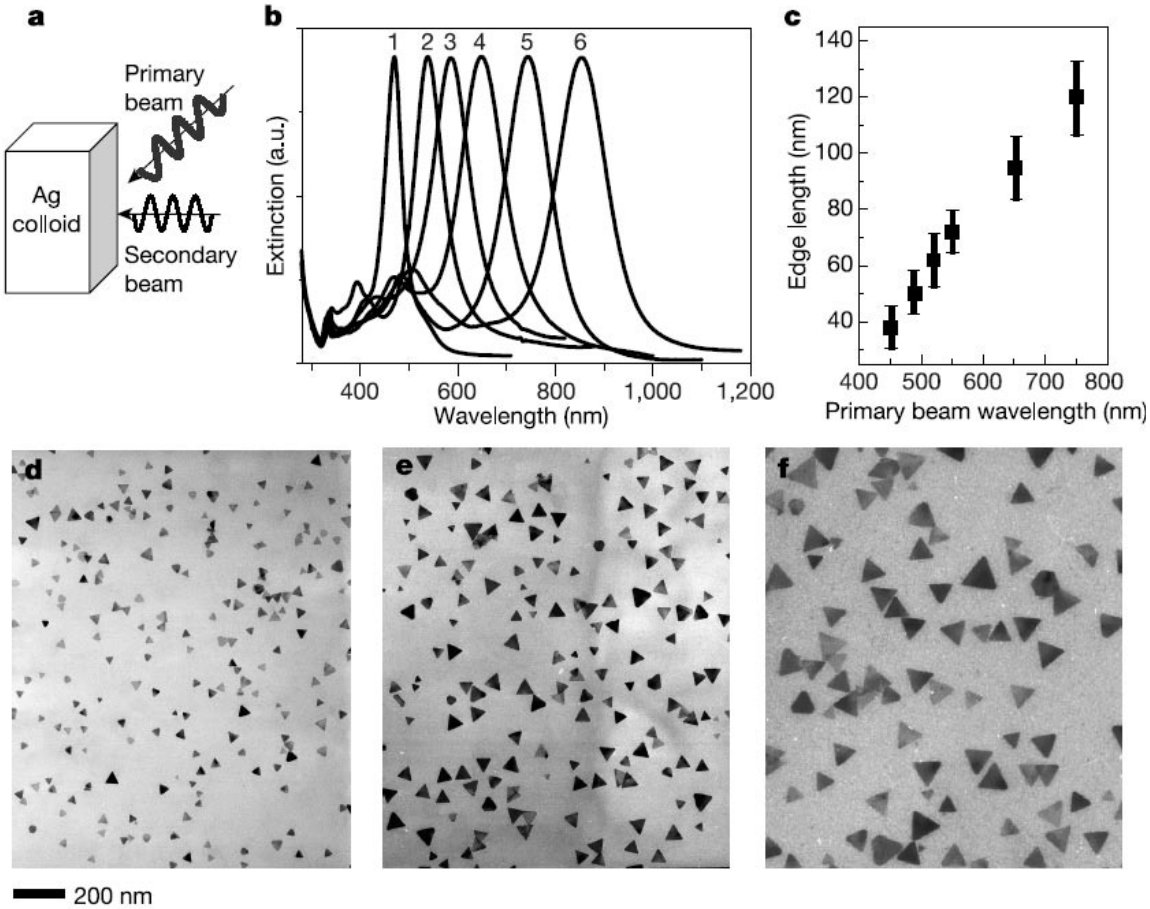


**Figure 1.8** (A) Scheme of irradiation set-up (B) Corresponding extinction profiles at 670 nm as a function of time. (B) Time-dependent UV-vis spectra showing the conversion of silver nanospheres to nanoprisms before irradiation and after (D) 40, (E) 55, and (F) 70 hours of irradiation. (Ref. 108)

source in this case, 457 nm) and absorbs more strongly than the transverse mode. In contrast, the transverse mode absorbs less strongly and blue-shifts. The authors propose that the reduced atoms deposit on the nanoparticle surface at a rate commensurate with the near field intensity enhancement at that face. Hence, the nanoparticles grow preferentially along the longitudinal mode. Crystal growth continues in this direction until the absorbance of the in-plane dipole mode (longitudinal mode) shifts beyond the excitation wavelength (457 nm). The authors note that nanodisks (i. e. prisms) possess a higher absorption coefficient at the excitation wavelength than rods, accounting for the presence of disks over other shapes (e.g., rods). Similar results were also observed by Callegari and co-workers who reported a study in which the variation of excitation wavelength was also used to control nanoprism edge length.[118]

The process of dual-beam excitation control of Ag nanoprism edge length was recently studied, and attributed to the promotion and suppression of cluster fusion processes.[48] In this work, single wavelength excitation could be used to achieve solutions of nanoprisms with relatively uniform edge lengths. This control was achieved by modulating the pH of the solution, which in turn mediates nanocrystal fusion via electrostatic interactions. High solution pH results in negative charge building on the nanoprism surface, thereby increasing electrostatic repulsion. As a result, prism fusion is efficiently inhibited at high pH, and unimodal nanoprism growth is observed. In contrast, acidic conditions promote prism fusion by lowering particle charge and leads to of the formation of large nanoprisms. This work simplified the Ag prism synthesis by eliminating the need for secondary irradiation, expanded the range of accessible prism edge lengths, and allowed one to reproducibly prepare nanoprisms with SPR wavelengths well into the NIR. Silver nanoprisms with SPR bands in the NIR region also have been synthesized by Liz-Marzan *et al.*[119] using light-emitting diodes in a photochemical approach.

Interestingly, researchers also have found that the photochemical conversion of Ag nanoparticles to nanoprisms can occur using multiple types of stabilizing agents. For example, Gehlen *et al.*[120] as well as Xia *et al.*[121] have used poly(*N*-vinyl-2-pyrrolidone) (PVP) instead of BSPP (which was used in the previously discussed synthesis from our group) to stabilize the Ag precursor nanoparticles. In the work of Junior and co-workers, the authors found that Ag nanoparticles prepared using low molecular weight (MW) PVP (29 and 55 kg/mol) underwent conversion to nanoprisms in the presence of fluorescent light whereas samples with high MW PVP (1300 kg/mol) did not. This work indicates that BSPP (or PVP) does not play a critical shape-directing role in determining the final morphology of the Ag nanoprisms, yet can influence nanoparticle conversion at high concentrations of capping ligands.

To this end, comprehensive studies of the role light and each reagent involved in photochemical synthesis of Ag nanoprisms have recently been reported by our group as well as Wu and co-workers. [107] [122, 123] In the first mechanistic study by our group, gold nanoparticles (AuNPs) were used as plasmonic seeds to photochemically initiate Ag nanoprism growth by irradiating the colloid at the SPR of the AuNPs in the presence of BSPP-capped AgNPs. Using this method, core-shell Ag triangular nanoprisms were generated with the gold core acting as a reaction label to elucidate the role of the seed particle in this photochemical synthesis (Figure 1.9). Interestingly, if a seed colloid was irradiated with light that did not overlap with its SPR, Ag nanoprisms did not form. This plasmon dependence was confirmed by using Au nanoprisms which exhibit SPRs in the NIR, and have no spectral overlap with the AgNP seeds. In this case, core-shell structures were again observed only under irradiation at the Au nanoprism SPR (Figure 1.10).

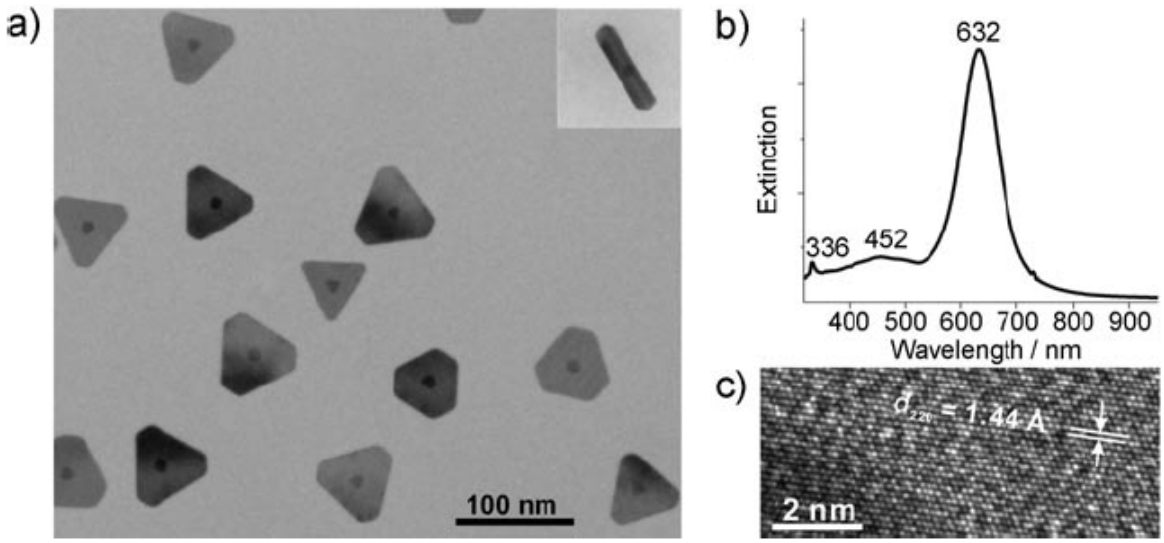


**Figure 1.9** (A) A TEM image of the Au@Ag core–shell nanoprisms (average edge length of 70±6 nm) synthesized by irradiation with 550-nm light. The inset shows the side view of a core–shell nanoprism. (B) Extinction spectrum of the Au@Ag core–shell colloidal nanoprisms after centrifugation. (C) A high-resolution TEM image of the [111] face of the Au@Ag core–shell nanoprisms. The hexagonal lattice shows a spacing of 1.44 Å, indexed as [220] of fcc Ag. (Ref. 107)

Building on this work, investigations were also made into the chemical role of each reagent in the synthesis, and a three step growth mechanism was proposed.[122] During the initial stage of photo-mediated Ag nanoprism growth, a Ag nanoparticle colloid is prepared by $NaBH_4$ reduction of $AgNO_3$ in the presence of trisodium citrate and BSPP. The resulting mixture exhibits an extinction maximum at 395 nm, and absorbs light throughout the visible range. The photochemical reaction induced by plasmon excitation of these particles has been proposed by several groups to be the charge transfer between adsorbates on the surface of the seed particle and "hot" holes that are likely produced by plasmon decay. [117, 122-124] Specifically, these reactions involve the reduction of silver cations by trisodium citrate on the Ag particle surface and oxidative dissolution of small Ag particles by $O_2$ (Eq. 1).

$$Ag^0 + ½\ O_2 + H_2O \rightarrow Ag^+ + 2\ OH^- \qquad (1)$$

BSPP increases the solubility of the Ag ions by complexing them and thereby acts as a "buffer" to keep the concentration of $Ag^+$ at approximately 20 $\mu$M (as determined by inductively coupled mass spectrometry, ICP-MS). The silver particles then serve as photocatalysts and, under plasmon excitation, facilitate $Ag^+$ reduction by citrate (Scheme 1.2). This is evidenced by the oxidation of citrate into 1,3-acetonedicarboxylate and its further decomposition into acetoacetate and $CO_2$ which was monitored by $^1$H-NMR spectroscopy.[122]

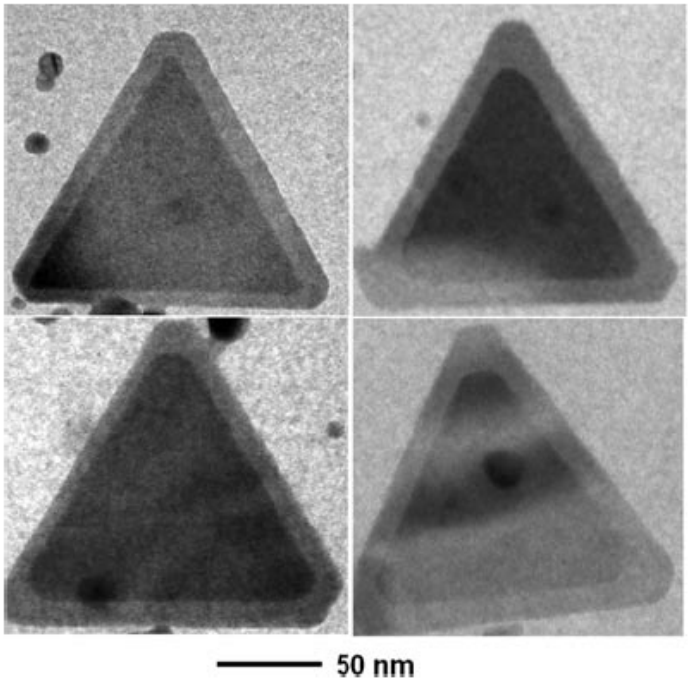


**Figure 1.10** Representative TEM images of Au@Ag core–shell nanoprisms with a gold prism core. The scale bar is the same for all images. (Ref. 107)

A mechanism for the subsequent growth of these isotropic particles into small and then larger nanoprism structures was proposed based on several empirical observations. First, after only 30 minutes of irradiating the Ag colloid, Ag triangular nanoprisms can be observed by TEM. While many mechanisms may be responsible for this growth pattern, a possible pathway involves dipole SPR excitation-induced ultrafast charge separation on the nanoparticle surface,[36] which may produce face-selective silver cation reduction as first postulated by Brus *et al.* (vide supra).[117] This theory is consistent with our recent observations using gold particles as plasmon reaction labels,[107] as well as the observations of others, which show inhomogeneous silver shell growth at early stages of photochemical synthesis.[117] Further growth by dipole

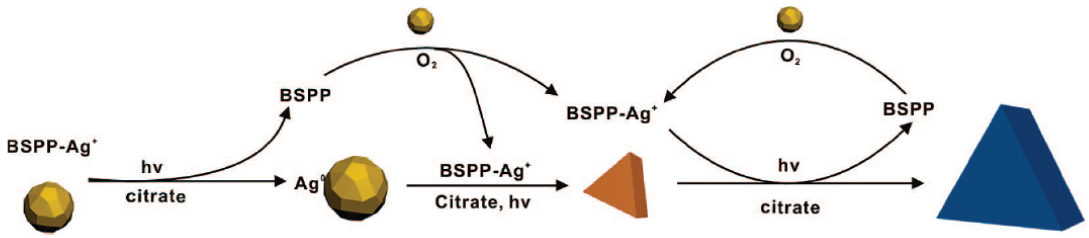


**Scheme 1.2.** Proposed photomediated growth pathway of silver nanoprisms from spherical nanoparticles. (Ref. 122)

plasmon excitation favors the formation of sharp-tipped silver nanoprisms because excitation of the dipole SPR localizes energy at the tips of the prism structure, while in-plane quadrupole excitation produces truncated prism growth by localizing energy on the edge of the nanoprism and facilitating silver deposition at those sites. This work provided significant insight into photochemical routes for preparing Ag nanoprisms, and provided a straightforward, self-consistent way to tailor both the architectural parameters and spectroscopic features of the silver nanoprisms. Remarkably, in an independent study, Wu and co-workers arrived at an almost identical mechanism for prism growth. In their work, they show that the reaction is first order in seed concentration, which indicates that seed particle fusion is unlikely to occur during the Ag nanoprism growth process. Importantly, the authors also report that at low illumination power (<10 mW/cm$^2$) the photochemical processes are rate-limiting, but at higher illumination power (>50 mW/cm$^2$) a thermal process is rate-limiting. This illumination power dependence was confirmed by the linear dependence of prism formation at illumination less than 10 mW/cm$^2$ and a "sub-linear" dependence with illumination intensities greater than 50 mW/cm$^2$. [123]

### 1.5.2 Ultraviolet Light and Radiolysis.

In addition to methods that use visible light, several techniques have now been developed that use ultraviolet (UV) light ($\lambda$ < 400 nm) to prepare nanoprisms. Some of these techniques use

UV light as an energy source to promote heating, and this process often leads to fusion or fragmentation of nanoparticles in solution.[108, 125-127] Other syntheses use UV light for radiolytic generation of radicals (e.g., UV excitation of 2-propanol to yield organic radicals)[128] that can, in turn, reduce metal ions to metals. In general, syntheses using these types of electromagnetic radiation often produce nanostructures of many different shapes, including prismatic ones. However these syntheses are important, because they highlight ways in which light can be used to produce nanoprisms that are not mediated by surface plasmon resonances.

In 2003, Jiang and co-workers[129] prepared Ag nanostructures with a variety of morphologies, including ribbons and prisms using UV irradiation. In a typical synthesis, an aqueous solution containing $AgNO_3$ and a capping ligand (nicotinic acid, formic acid, or pyridine) was exposed to UV light for 2 minutes, followed by boiling for several minutes. Silver nanoribbons were generated as the primary product when nicotinic acid was used as the particle surface capping agent, whereas pyridine or formic acid resulted in the formation of polycrystalline Ag nanoprisms. To describe the growth of these structures, the authors propose that organic molecules cap specific faces of growing Ag nanoparticles and direct their final morphology during the heating phase of the synthesis, and that specifically the number of pyridyl groups of the capping ligand dictates the final shape of the nanostructures. For example, pyridine (containing 1 pyridyl group) results in the observed prismatic nanostructures, whereas nicotinic acid (2 pyridyl groups) yields nanoribbons and 2,2’-dipyridylamine (with 3 pyridyl groups) generates long, wire-like structures. This description can be called the “face-blocking theory”, which postulates that a given capping ligand or surfactant has a preferential affinity for one crystal face over another based on surface energetics and/or arrangement of surface atoms.

In a different use of light, Tsuji and co-workers[130] formed both nanoprisms and nanorods by exposing an aqueous solution of Ag nanoparticles to a Nd:YAG laser without the use of molecular stabilizers. Initially, Ag nanoparticles (~ 20 nm diameter) were generated by ablation of a silver metal plate in pure water with the fundamental harmonic (1064 nm) of a Nd:YAG laser (12 mJ/pulse) for 10 minutes. The silver plate was then removed and the colloid was subsequently subjected to the third harmonic (355 nm, 50 – 100 mJ/cm$^2$) of the Nd:YAG laser for an additional 10 minutes. The final colloid was composed of Ag triangular nanoprisms or nanorods. The nanoprisms were found to be single crystalline and had a broad size distribution with edge lengths ranging from 100 - 300 nm. This synthesis is of significant interest in the context of face-blocking mechanisms. Here, no capping ligand or surface passivating moiety was intentionally used, which indicates that there may be multiple ways to effect platelike growth of noble metal nanoparticles.

Delcourt *et al.*[131, 132] reported that Ag nanoprisms also could be prepared via radiolysis in the presence of an organic complexing agent such as ethylenediaminetetracetic acid (EDTA). In a typical synthesis, nanoprisms were obtained when a solution of $Ag_2SO_4$, EDTA, and 2-propanol was subjected to 10 krad of radiation for several days. The final nanoprisms are single crystals (triangular face bound by [110] planes) with average edge lengths between 100 - 150 nm and thickness of 10 nm. Interestingly, the thickness of the prisms is approximately the same as that of the initial particles, suggesting that crystal growth occurs predominantly in the [110] and [100] directions. As with the methodologies previously described in this section, the authors conclude that light is necessary only for radiolytically reducing $Ag^+$ ions (via the decomposition of 2-propanol to form organic radicals) to form the initial silver nanoparticle seeds, which

undergo ligand-directed growth (e.g. by a face-blocking mechanism) to form the final nanoprisms.

### 1.5.3 Summary of Photochemical Routes

Research thus far has shown that a variety of radiation wavelengths can be used to generate nanoprisms. Depending on wavelength, the proposed mechanisms of formation differ, but have some common elements. These mechanisms involve crystal face-blocking,[112, 129] anisotropic surface energetics that create preferential growth on various crystal facets,[103, 117, 122], as well as photo-induced redox processes[48, 122, 133] . For the processes that use SPR-excitation mediated methods, a significant degree of particle size control has been demonstrated and the mechanistic underpinnings of the reaction have been evaluated. These syntheses are efficient and reliable, and the ability to tailor architectural parameters such as thickness and edge length allow the researcher to envision numerous applications based upon them.

## 1.6 Thermal Syntheses of (or Chemical Reduction Methods for Producing) Triangular Nanoprisms

Although the first reported, high-yielding synthesis of triangular nanoprisms followed a photochemical mechanism, it was not long before comparable syntheses were developed using thermal methodologies. For these methods, the central synthetic approach dates back to early protocols designed to produce pseudo-spherical nanostructures,[52, 101] where methods follow a general formula: metal ions are reduced by a given chemical reducing agent in the presence of a capping agent (generally a surfactant, polymer, or small molecule) to form small nanoparticles. These nanoparticles subsequently grow at a specific temperature and pH to form larger structures. In this section, nanoprisms that have been prepared in both aqueous and organic environments will be reviewed. Those processes that are mediated through the addition of

biological molecules or in a biological host are highlighted as a subset of synthetic schemes carried out in the aqueous phase.

**1.6.1 Thermal Syntheses in Aqueous Media.**

One of the first observations of spectroscopically identifiable nanoprisms from a thermal synthesis was made by Liz-Marzán *et al*.[134] The preparation of these nanostructures involved the formation of a gold sol using salicylic acid and $HAuCl_4$ in the presence of NaOH, followed by heating. The resulting nanoparticle solution contained a mixture of plate-like nanostructures and pseudo-spherical nanoparticles, and the extinction spectrum from this mixture showed two distinct bands corresponding to the SPRs from the two types of particles (Figure 1.11). The band in the visible region was assigned to the dipole plasmon resonance of the pseudo-spherical nanoparticles, and the near-IR band was assigned to the SPR of the triangular nanoprisms. However, the near-IR SPR band observed from the nanostructures produced in this synthesis was relatively broad as compared with later work, and implied a large size and shape distribution of the anisotropic nanostructures in solution. Similar optical spectra were later observed for Au nanoprisms made by Norman and coworkers[135] using $Na_2S$ reduction of $HAuCl_4$, and by Sastry *et al*.[85] using a biological methodology (discussed in detail in Section 1.6.2).

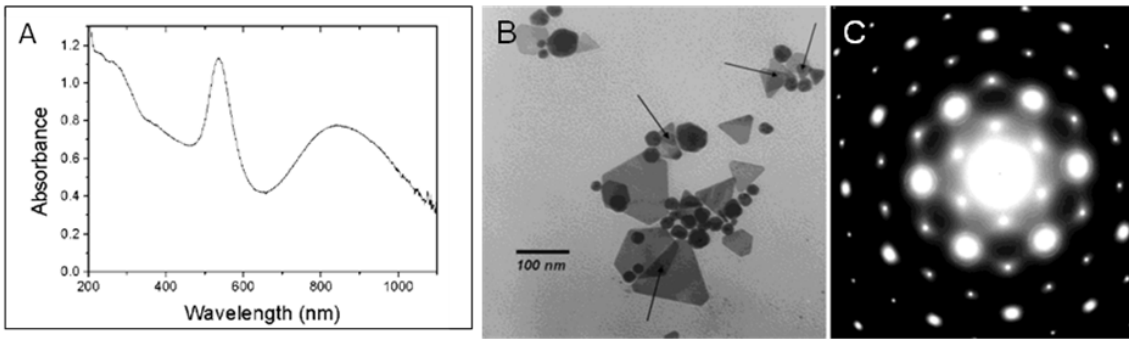


**Figure 1.11** (A) UV-visible spectrum measured from a dilute solution containing the particles shown in (B). (C) Electron diffraction pattern from a single Au nanotriangle with the electron beam perpendicular to the [111] plane. The spot array indicates a the [111] direction. (Ref. 134)

Since that time, methods for producing high quality Au nanoprisms, which exhibit higher order plasmon resonance modes have been developed.[81, 84] Our group has used a seed-mediated, surfactant-based system that produces a mixture of Au nanoprisms and pseudo-spherical nanoparticles, each with relatively narrow size distributions (nanoprism edge length: 144 ± 30 nm, nanoparticle diameter: 35 ± 2 nm).[81, 84] This method involves the use of nanoparticle seeds generated by rapidly reducing $HAuCl_4$ with $NaBH_4$ in the presence of trisodium citrate. These seeds are 4 – 6 nm in diameter, and are serially added to "growth solutions" that contain the cationic surfactant cetyltrimethylammonium bromide (CTAB), NaOH, $HAuCl_4$, and ascorbic acid. The resulting nanoprism solution exhibits distinct optical features which have been assigned to the dipole and quadrupole plasmon resonances of the Au nanoprisms, and the dipole SPR of pseudo-spherical nanoparticles that form concomitantly. These observations marked the first time that the quadrupole SPR was experimentally identified for a colloidal solution of Au nanoprisms (Figure 1.12). This synthetic method was subsequently used to control the edge length of Au nanoprisms between 100 and 300 nm by using the nanoprisms themselves as seeds.[104] Higher order plasmon modes also have been observed from prisms produced from a

synthesis described by Yun and coworkers wherein PVP is used as a capping ligand and shape directing moiety (Figure 1.13).[81]

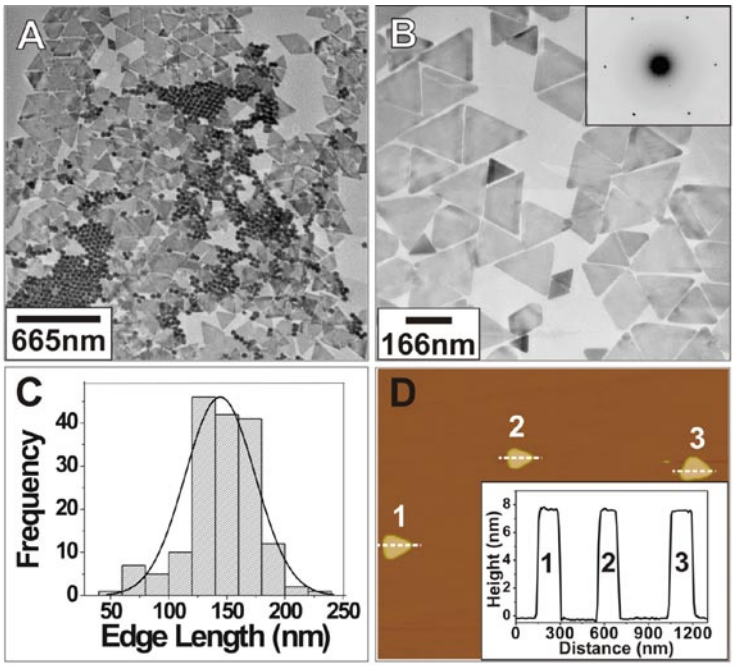


**Figure 1.12** (A) TEM image of Au spherical and triangular nanoparticles. (B) Zoom-in image. Inset shows the electron diffraction pattern of the top of a single prism. (C) Histogram of nanoprism edge lengths. (D) AFM image of nanoprisms on mica (tapping mode). Inset: height profile along the dashed lines. (Ref. 84)

The characterization of Au nanoprism optical properties evolved with the improvement of synthetic procedures for generating such structures. Conversely, the optical signatures of Ag nanoprisms were initially identified from photochemically generated nanostructures,[45] and these spectra were benchmark references for the development of thermal syntheses of similar products. Interestingly, Ag plate-like nanostructures were observed from thermal processes as early as 1999 using the bacteria *Pseudomonas stutzeri* AG259 (see section 1.6.2 for detailed description)[136], however Chen and Carroll[82, 137] reported one of the first high-yielding thermal syntheses to prepare Ag nanoprisms using a seeding methodology. In this synthesis, small Ag nanoparticle seeds (~ 15 nm) were prepared by reducing $AgNO_3$ with $NaBH_4$ in the presence of sodium citrate. These particles were then grown by serial addition of the seed particles into growth solutions containing Ag ions, ascorbic acid, and CTAB, in a manner similar to the method described for the synthesis of both Au nanoprisms and nanorods.[80, 84] The resulting Ag nanoparticle mixture was subsequently aged for 24 hours to produce a mixture of truncated

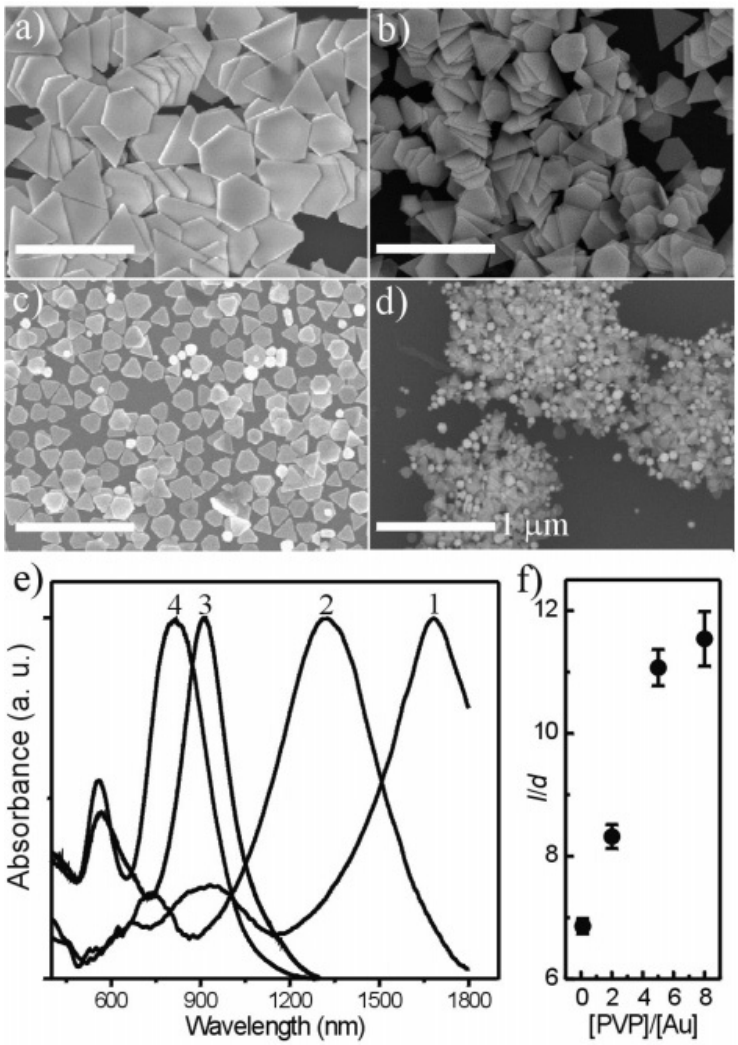


**Figure 1.13**. (A-D) FE-SEM images of gold nanoplates with edge lengths of varying size; Scale bar is 1 micrometer in all cases (e) UV-vis-NIR absorption spectra of the samples in panels (A-D). (F) Aspect ratio (width/thickness) as a function of the molar ratio of PVP to Au. (Ref. 81)

nanoprisms, nanodisks, short nanorods, and polyhedral nanoparticles. Centrifugation-based separation methods were used to prepare colloids composed primarily of Ag triangular prisms (78 %). In subsequent work, Chen and Carroll showed that many of the same factors that influence the seed-mediated thermal synthesis of Au anisotropic nanoparticles, also influence the growth of Ag nanoprisms. These factors include metal ion to reducing agent ratios, seed concentrations, and bromide ion concentrations.[83]

Xia *et al* .also have developed methods for preparing Ag nanoprisms using a combination of thermal and photochemical methods in aqueous solution.[121] In this work, silver nanoparticle seeds (d < 5 nm) are prepared by $NaBH_4$ reduction of $AgNO_3$ in the presence of PVP and sodium citrate. The resulting colloid (which is yellow, and has a narrow UV-Vis band at ~ 400 nm) is then refluxed

in ambient laboratory light for 10 h. After this process, the mixture is almost completely converted into triangular nanoprisms (95%) and wire-like nanostructures (~ 5%). In contrast to previous thermal synthesis of Ag nanoprisms, these triangular nanostructures exhibited very little tip rounding, as evidenced by a red-shift in the nanoprism SPR bands consistent with theoretical predictions.[36] Interestingly, the authors found that both light and heat were necessary for prism formation in this synthesis, where, possibly through an SPR-mediated preferential metal ion deposition mechanism,[117] light initiates the formation of small prismatic seeds that then grow via thermal processes into larger structures.

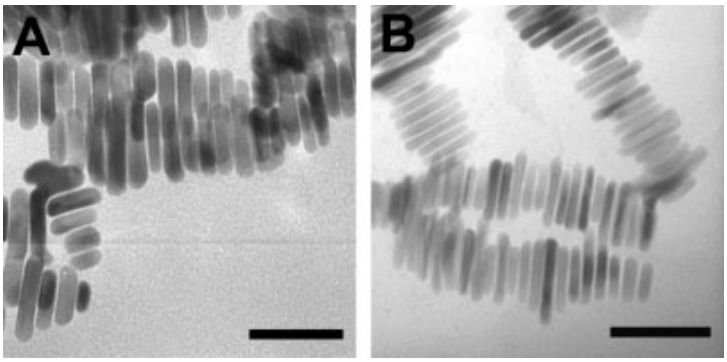


**Figure 1.14.** TEM images of stacked Ag nanoprisms showing the effect of $NaBH_4$ concentration on nanoprism thickness; (A) 0.30mM, (B) 0.80 mM. Scale bars for both images correspond to 50 nm. (Ref. 106)

Controlling nanoprism thickness has been more challenging than controlling edge length. There is only one photochemical approach[122] and one thermal method reported thus far.[106] The thermal approach involves the reduction of $AgNO_3$ with $NaBH_4$ in the presence of trisodium citrate, PVP, and $H_2O_2$ at room temperature. The thickness (and to a lesser degree, the edge length) of the final Ag nanoprisms was dependent on the concentration of $NaBH_4$ and varied from ~ 8 (using 0.3 mM aqueous $NaBH_4$) to ~ 4 nm (using 0.8 mM aqueous solution of $NaBH_4$). Electron microscopy, spectroscopic and theoretical studies showed that the variations in thickness, not edge length, were responsible for the large differences observed in the optical spectra of the various samples (Figure 1.14).

While optical spectra are an exceptionally powerful nanoparticle characterization tool, work on nanoprism thickness highlights that multiple structural variables (edge length, thickness, and degree of truncation) ultimately dictate the corresponding optical properties.[36, 110] For this reason, it is impossible to determine the exact dimensions of the nanoprisms based only on the optical properties of the colloid. For example, tip truncation, shorter nanoprism edge length, or increased nanoprism thickness all lead to a blue-shift in the in-plane dipole SPR. In this case, UV-vis spectroscopy cannot reveal which of these architectural parameters is causing the change in the optical properties, and emphasizes the complementary role of extinction spectra to electron microscopy or surface probe techniques in characterizing noble metal nanostructures.

### 1.6.2 Biological Thermal Syntheses.

Among the aqueous methods for preparing Ag and Au nanoprisms, a few syntheses have been developed that generate plate-like nanomaterials based on a combination of biological organisms, environments, and molecules. For example, Klaus *et al.*[136] have synthesized Ag nanoprisms in the bacterium, *Pseudomonas stutzeri* AG259, which is an organism known to accumulate metal ions in its intracellular space. In these experiments, bacteria were grown on agar substrates containing 50 mM $AgNO_3$. These metal ions were then reduced in either the growth medium or within the bacteria where they ultimately formed nanoprisms that accumulated in the periplasm of the organism. TEM and EDS analysis showed that the triangular faces of the nanoprisms, like the previously described triangular Au nanoprisms, were {111} planes. Nanoparticles (including nanoprisms) were most often found at the poles of the bacteria, and each cell generally contained less than 5 nanoprism structures. The driving force for particle localization within the bacteria is unclear, but the prospect of bacteria-generated anisotropic nanostructures points towards the possibility for large-scale, organism-based synthetic schemes.

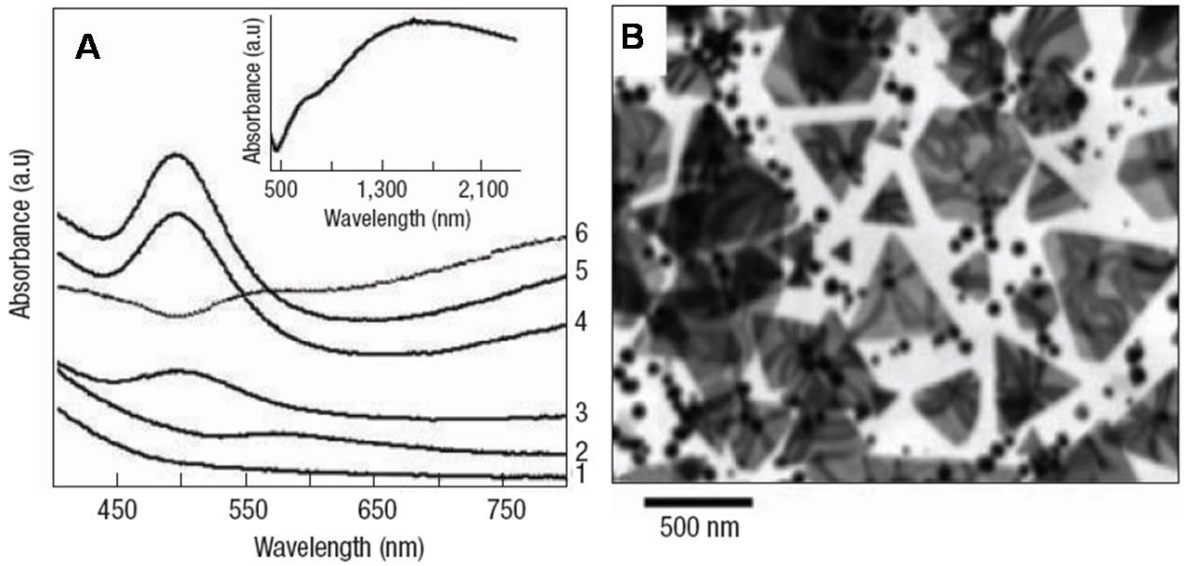


**Figure 1.15** UV–vis spectra recorded as a function of time of reaction of lemongrass extract with aqueous gold ions; curves 1–5 correspond to spectra recorded 1, 90, 160, 220 and 340 min after reaction. Curve 6:spectrum obtained from the purified gold nanotriangle solution; inset:UV–vis–NIR spectrum of a solution-cast film of purified gold nanotriangles obtained by reaction of $AuCl_4$-lemongrass extract solution on a quartz substrate. (B) Representative TEM image of triangular gold nanotriangles by reduction of aqueous $AuCl_4$ by lemongrass extract. (Ref. 85)

In addition to bacteria-generated Ag nanoprisms, single crystalline Au nanoprisms also have been made using a mixture of biological molecules from the aqueous extract of lemongrass plants,[85] aloe vera,[138] and brown seaweed.[139] In these experiments plant extracts were used as both reducing agents and capping agents for the synthesis of Au nanostructures. For example, Sastry, *et al.* have used lemongrass extract[85] to reduce $HAuCl_4$, and propose that preliminary seed nanoparticles form and then aggregate within a “liquid-like” mixture of aldehydes and ketones. These aggregates are then thought to fuse into nanoprisms and truncated nanoprisms (Figure 1.15). The optical spectrum associated with this mixture shows a broad NIR-band associated with the anisotropic nanostructures and a visible band, which is most likely associated with the pseudo-spherical nanoparticles that are also observed as products from this synthesis.

This assignment is based upon work done by our group and others as well as calculations by Schatz *et al*.[110] Finally, a similar methodology was used by Liu *et al.*, to produce a mixture of nanoprisms and truncated nanoprisms.[139] In this study, brown seaweed extract (*Sargassum sp.*) was again found to serve as a reducing and capping agent to direct the formation of high aspect ratio gold nanoprisms with 200 to 800 nm edge lengths and 8 to 10 nm thicknesses.

In addition to these methodologies, several groups also have investigated the use of proteins and nucleic acids to control nanoparticle growth.[140] For anisotropic nanostructures, Brown *et al.* have investigated the ability of polypeptides to direct Au crystallization using methods inspired by enzyme-mediated biomineralization processes.[140] In this study, various amino acid sequences were incubated with $AuCl_3$, KOH, and sodium ascorbate at room temperature. In addition to investigating the biomolecule-directed synthesis of other Au nanoparticle morphologies, the authors found that there were two critical factors for generating Au nanoprisms in particular. First, the polypeptide must have a pre-existing catalytic function (e.g., acid catalysis or a similar mechanism). Second, the polypeptide must possess an affinity for the Au surface that is not thiol-based (e.g., not driven by cysteine residues). Of the 50 amino acid sequences studied, five showed the ability to modify the formation of Au crystals, of which three displayed increased rates of gold nucleation and crystallization. Interestingly, anisotropic nanostructures were only observed with those polypeptides that increased the rate of crystallization. The authors postulate that the polypeptides create a low pH environment near the surface of the growing crystal, and that this environment in combination with blocking of the {111} crystals faces, yields nanoprisms. Shao *et al.* have reported a similar preparative route to synthesize gold nanoprisms that relies on amino acids.[141]

### 1.6.3 Microwave and Ultrasound Assisted Techniques

Nanoprisms also have been prepared using microwaves and ultrasound.[112, 125-127, 142] In terms of nanoparticle synthesis, microwaves are believed to heat the reaction solution rapidly and uniformly leading to more homogeneous nucleation events and shorter crystallization times than conventional heating (e.g. by hot plate). Sonication of a colloidal solution results in acoustic cavitation, during which time bubbles form, grow, and implode in solution. Depending on the power, the temperature of the imploding bubbles can be as high as 1000 K and the pressure within the bubbles can be as high as 1800 atm.[125-127] In addition to the high temperatures and pressures created, cavitation also can create shock waves in solution that impact the nanoparticle surface, sometimes leading to unusual shapes and structures.[125]

For example, Tsuji and co-workers[142] developed a method to prepare single crystalline triangular gold nanoprisms (and truncated nanoprisms) via a microwave polyol method. The authors subjected a solution of $HAuCl_4$, PVP, and ethylene glycol to pulsed or continuous wave modes of microwave irradiation. Under continuous microwave irradiation, the temperature of the colloid increased to 196 °C over the course of one minute and was held at this temperature for an additional minute. Samples exposed to continuous microwave irradiation for more than 120 seconds displayed three extinction bands (545 nm, 590 nm, and 645 nm) consistent with the formation of platelike nanoparticles.[81, 84]

As mentioned above, ultrasonic energy can cause cavitation bubbles to collapse creating shock waves throughout a reaction solution. Researchers have proposed that cavitation can lead to the decomposition of water or other molecules into radicals which can then reduce metal ions to metal in solution.[125-127] Shock waves created by cavitation also are believed to result in the rapid impact of the reaction liquid on the surface of the nanoparticles resulting in their

dissolution. These phenomena can accelerate the Ostwäld ripening process and allow nanoparticles of various morphologies to be generated. This method has been used by Zhu *et al*.[125] to produce colloidal solutions of Ag nanoplates using silver nitrate in *N*,*N*-dimethylformamide (DMF) in the presence of PVP where DMF can be used as both solvent and reducing agents for metal nanoparticle synthesis (Eq. 2).

$$HCONMe_2 + 2Ag^+ + H_2O \rightarrow 2Ag^0 + Me_2NCOOH + 2H^+ \qquad (2)$$

For these methods, the molar ratio of PVP to $AgNO_3$ was a key factor in determining their final morphology, where ratios between 0.1 and 0.3 were optimal for nanoprism formation.[143]

Similarly, Cai *et al*.[112] have developed an ultrasonication route to prepare Au nanoprisms in solution, although the overall yield of prism particles was low. In a typical experiment, $HAuCl_4$ and PVP are combined in ethylene glycol under oxygen-free conditions and subjected to ultra-sonication (frequency = 45 ± 2.5 kHz, power = 2.4 W/cm$^2$) for various periods of time. Here again, the ethylene glycol is believed to serve a dual role as solvent and reducing agent. Interestingly, the authors found that the formation of gold nanoprisms is time dependent. The final colloid is composed primarily of 6 – 10 nm thick nanoprisms and truncated nanoprisms with 30 – 40 nm edge lengths, as well as a small number of spherical nanoparticles. Aging of the nanoprism colloid for one week resulted in an overall increase of the average edge length of the nanoprisms from 30 – 40 nm to 70 – 90 nm. This observation was corroborated by a significant red-shift of the in-plane dipole surface plasmon resonance band from 690 to 760 nm. The authors propose that adsorption of PVP to the {111} crystal faces, in conjunction with the mild reaction conditions, are the primary factors influencing nanoprisms formation and morphology.

### 1.6.4 Thermal Syntheses in Organic Media.

There also has been significant progress in the development of organic phase syntheses for triangular nanoprisms. In contrast to the aqueous methods described previously (which are typically conducted at room temperature or under physiological conditions), many of the organic protocols require elevated temperatures (e. g. reflux conditions). A particularly interesting aspect of these synthetic approaches is that often the solvent and/or surfactant acts as both a capping ligand and reducing agent.

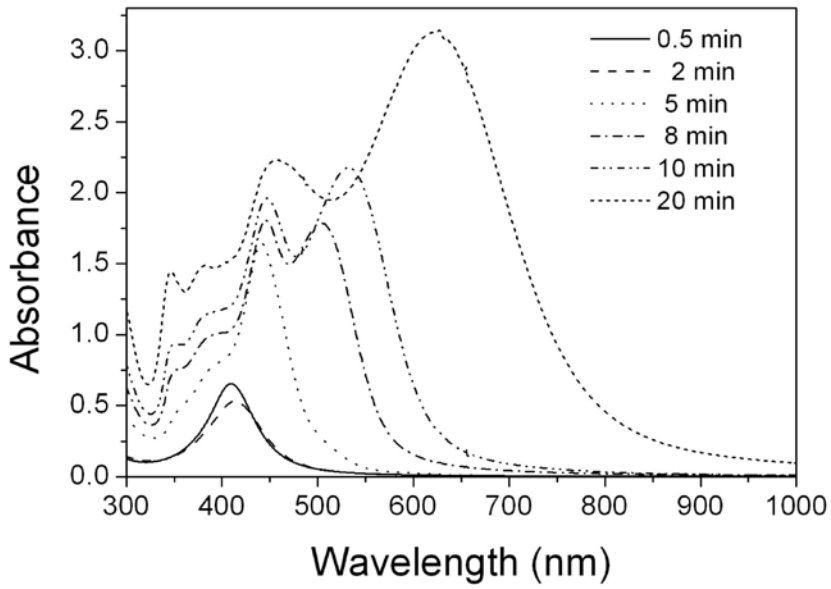


**Figure 1.16** Time evolution of UV-visible spectra during the formation of Ag nanosprisms in DMF. (Ref. 133)

An early work in thermal organic synthesis of nanoprisms was reported by Liz-Marzán *et al.*[133] where Ag nanoprisms were prepared by boiling DMF and reducing $Ag^+$ in the presence of PVP. The authors postulate that DMF acts as both the solvent and reducing agent.[143] The authors found that if the concentration of Ag ions was increased relative to the concentration of PVP, particles with anisotropic shapes (mainly nanoprisms) were observed. After purification by centrifugation, the nanoprisms could be largely isolated from the pseudo-spherical nanoparticles, and the optical signatures of the $Ag^+$ nanoprisms could be observed. The optical spectrum is consistent with that observed for photochemically generated nanostructures: the in-plane dipole

resonance (~ 770 nm), the in-plane and out-of-plane quadrupole resonances (~ 470 and 340 nm, respectively), and the weak out-of-plane dipole resonance (~ 410 nm) with deviations explained by the imperfect triangular shape of the prisms.

Interestingly, this work showed that the optical signatures of nanoprisms were very sensitive to the refractive index of the surrounding medium. When these Ag nanoprisms were transferred from DMF to water, the in-plane dipole resonance blue-shifted ~ 40 nm and the out-of-plane quadrupole resonance shifted ~ 2 nm. This effect also has been observed by others in the context of surface-immobilized metal nanostructures.[105, 144, 145] The authors also demonstrated a degree of size control based on the reflux time of the nanoparticles in DMF, where longer reflux times led to larger nanoprism structures (Figure 1.16). In a separate report, Ag nanoprisms have been made in a similar fashion using formamide as both a solvent and reducing agent in the presence of poly(ethylene glycol) (PEG) at room temperature. In this report, the authors found that in the presence of a 1:1 polymer mixture of PEG and PVP, a mixture of nanoprisms and nanospheres could be prepared.[111]

### 1.6.5 Summary of Thermal Syntheses of (or Chemical Reduction Methods for Producing) Triangular Nanoprisms

In previous sections, it has become evident that nanoprisms can be formed in a wide variety of media under relatively mild reaction conditions, and that these prisms exhibit common optical and crystallographic features. However, synthetic challenges remain. While Ag nanoprisms have been synthesized in both aqueous and organic environments, Au nanoprisms have only been accessed in aqueous media. There are still very few methods for controlling nanoprism thickness, and the driving forces behind growth of either triangular, hexagonal, or disklike nanoprisms are still poorly understood. What stands out amongst the thermal

preparations for nanoprism structures is the wide variety of chemical conditions used to achieve the same nanoparticle architecture. While yield, size, and monodispersity of nanoprisms vary from synthesis to synthesis, the consistent observation of platelike growth encourages one to seek the common themes and approaches amongst these seemingly disparate methods. In the following section, a very brief overview of commonly proposed platelike growth mechanisms are presented in order to provide current thinking in shape evolution of Au and Ag noble metal nanoparticles.

### 1.7 Mechanisms of Platelike Growth

At first glance, there is little overlap between the chemistries involved in each preparative route for nanoprisms. Indeed, each synthetic scheme generates nanoprisms with different compositions, yields, sizes, and size distributions. However, upon closer inspection a central theme emerges within most syntheses: mediated reduction of metal ions onto nanoparticle seeds. Although the experimental details differ (e.g. temperature, pH, surfactant/capping ligands, reducing agents), each methodology involves two general steps: (1) nucleation of nanoparticle seeds and (2) crystal growth of seeds by mediated reduction of metal ions. In the nucleation stage, metal ions are reduced via thermal or photochemical means to generate small metal nanoparticles. In a subsequent growth step, these nanoparticle seeds are combined with metal ions and reducing agents. and exhibit additional crystal growth until the final structure is obtained. Yet, such a general scheme oversimplifies the complex issue of crystal nucleation and growth. Typically, mechanisms for nanoprism formation can be broken down into crystallographic and redox chemistry arguments. While aspects of these theories overlap, here they are treated as distinct components which control nanoprism formation through a delicate interplay between the two.

### 1.7.1 Crystallographic Arguments

Crystallographic mechanisms can be described as mechanisms that use the crystal structure of the original seed particle, crystal face-blocking mechanisms, and/or crystal facet surface energetics to explain the preferential growth of a nanoprism structure. For the seed nanoparticle, it has often been postulated that the original structure of the seed dictates the final morphology of the nanostructure by limiting the number and variety of crystal facets available for growth.[78, 146, 147] In the case of face-blocking mechanisms, as discussed previously, these processes selectively block one crystal face from metal ion reduction, and thereby promote growth of other facets. In the case of crystal facet surface energetics, due to the coordination number and therefore chemical reactivity of the surface atoms, certain crystal facets exhibit higher surface energies and higher chemical reactivities than others (e.g. $\sigma_{Au(111)} < \sigma_{Au(110)} < \sigma_{Au(100)}$).[148, 149] To explore this topic, theoretical models and experimental results in plate-like silver halide crystals (rock salt structure, composed of two interpenetrating face-centered cubic (*fcc*) lattices) are discussed and parallels can be drawn between the formation of these structures and the plate-like growth of Ag and Au (both *fcc* metals) nanoprisms.

For the past two centuries, the photosensitivity and photo-reactivity of plate-like silver halide crystals (i. e. AgBr, AgI) have been exploited in a variety of photographic film and memory storage applications.[150-154] In an effort to improve the current technology, a variety of studies, in both the scientific and patent literature, have focused on developing an understanding of the crystallization processes occurring in the formation of plate-like silver halide (primarily AgBr) crystals. From these reports, it is generally believed that plate-like crystal growth can only occur when the initial nanoparticle seeds contain one or more parallel twin planes.[155-158] Although AgBr nanoparticle seeds are often described as spherical structures, on the atomic scale

they are bound by the {111} and {100} faces, which are the most stable AgBr faces in the absence of capping ligands. During the initial stages of nucleation, the AgBr seeds undergo a process called twinning, in which stacking faults are formed within the crystal matrix. Due to their atomic symmetry, coalescence between two {100} faces will not generate the low-energy stacking faults (twins) required for plate-like crystal growth. In contrast, coalescence between two {111} facets (oriented at a 60º rotation relative to one another) yields stacking faults, which can lead to crystal growth normal to the {111} crystal planes.[103]

Crystal twinning that leads to plate-like structures was proposed by Berriman and Herz[159] to account for the plate-like morphology of silver bromide crystals. Hamilton and Seidensticker[160] later confirmed this hypothesis experimentally in their report that plate-like germanium crystals possess two or more twin planes parallel to their major {111} facets. Twinned seeds are believed to be formed from coalescence events between two unstable {111} crystal faces.[154, 161] This was demonstrated experimentally by Antoniades *et al.*, who showed that the rate of addition of Ag precursor ($AgNO_3$) as well as the concentration of the reducing agent (gelatin) control the coalescence events that lead to twinned AgBr seeds (which ultimately lead to plate-like AgBr crystals).[151] Hence, although coalescence is responsible for the formation of twins, several papers have found that other experimental factors including capping ligand and reducing agent (gelatin in both cases), concentration, pH, and temperature are all key parameters in controlling the degree of crystal twinning in solution.[155]

Twinned crystal seeds are believed to set the stage for plate-like morphologies by providing low-energy reentrant grooves favoring lateral crystal growth (Scheme 1.3). Jagannathan *et al.*, demonstrate experimentally and theoretically that plate-like crystal growth is propagated by the formation of two twin planes parallel to their major {111} crystal faces.[156] This atomic arrangement initially results in {111} faceted reentrant grooves on the sides of the crystal plates, providing nucleation sites for adsorption of new crystal layers and driving plate-like crystal growth. The authors calculated that the probability of adsorption at the reentrant groove is ~ 50 times greater than adsorption at a (non-twinned) surface site. Preferential crystallization at reentrant grooves can also be rationalized using a nearest neighbor argument: an isolated atom can form four nearest neighbor bonds in a reentrant groove and only three on a {111} face. The increased bonding strength and coordination number thus results in preferential adsorption at reentrant grooves over the {111} faces. Ming and Sunagawa observed similar crystallization events using Monte Carlo simulations.[158, 162] Interestingly, the reentrant grooves are regenerated as new layers of atoms deposit on them, making them permanent preferential regions of lateral growth. Growth continues until the adsorption units ($AgBr_3^{2-}$ and other species) are exhausted and yields the final nanoprisms where the

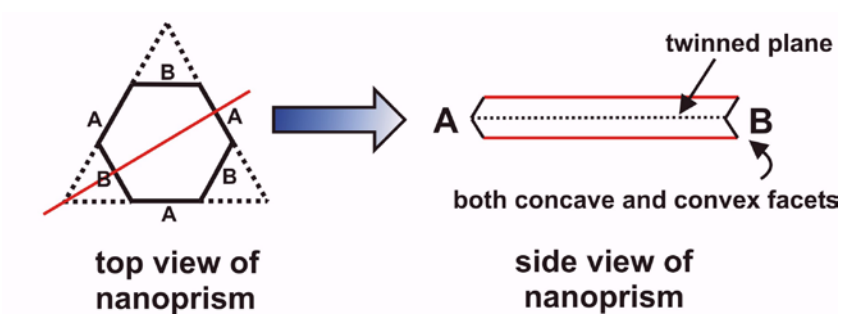


**Scheme 1.3** Silver halide model for a single twinned plane. Alternating sides contain A-type and B-type faces. The reentrant grooves of the A-type faces causes rapid growth that is arrested when the face grows itself out, leaving a triangular prism with slow-growing B-type faces. (Ref. 103)

major faces are bound by the {111} crystal planes.

Anisotropic crystal growth of Au or Ag derived from twinned crystal seeds was most recently addressed in a comprehensive article written by Lofton and Sigmund,[103] who extended these crystallization arguments to plate- and needle-like nanostructures composed of Ag and Au. Theoretical and experimental results have shown that silver halide crystals (NaCl structure) and metals (*fcc* structure) are bounded by the {111} crystal faces.[163, 164] In their paper, the authors argue that the crystal structure of the seed particle ultimately dictates the final morphology of the crystal. This is seemingly in contrast to many papers published by other groups that argue that preferential adsorption of capping ligands or surfactants directs the formation of rod- or platelike growth. Lofton and Sigmund point out that such surface passivation (or "crystal-face poisoning") models are unlikely given that identical nanoparticle shapes can be attained via drastically different methods and chemical environments. Indeed, the various methodologies highlighted in this discussion support their conclusions. However, recent work with halide ions presents an interesting counterpoint (see section 1.7.2 and Chapter 6).[165-167]

Although there are no clear answers about the parameters that control the degree and arrangement of stacking faults in crystal seeds, the role of crystal twinning in directing the final architecture of nanostructures may be a crucial element. In most of the examples for preparing Ag and Au nanoprism crystals cited in this review, the initial seed nanoparticles are prepared by chemical reduction of metal precursors (e.g., $AgNO_3$ or $HAuCl_4$) in the presence of one or more capping molecules. Generally, fast reduction of the metal ions (e.g., accomplished by rapid addition of strong reducing agents to metal salts) results in small, pseudo-spherical nanoparticles.[54, 168-170] The surfaces of the nanoparticles typically exhibit a mixture of {111} and {100} planes. To minimize their overall energy, nanoparticle seeds will undergo twinning to

form a twinned icosahedron or decahedron. Interestingly, the shape of the small nanoparticles (< 5 nm) can fluctuate, and studying their morphology and crystal structure can be difficult. The chemical environment can also cause morphological and crystal structure changes in the nanoparticles. For example, Xia and co-workers.[146] recently reported that addition of $Fe^{3+}$ or $O_2/Cl^-$ to a Ag nanoparticle colloid comprised of twinned crystals results in rapid etching of the crystals. After 24 hours, a second nucleation stage occurred to yield single-crystalline Ag nanoparticle seeds

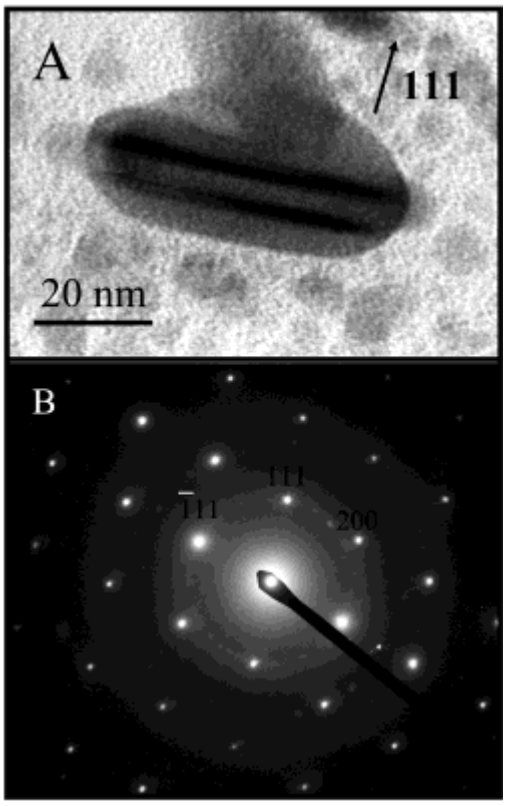


**Figure 1.17** (A) TEM image of the silver nanodisk taken in side view,showing the contrast from (111) stacking faults and a preferential growthalong the stacking faults. The orientation relationship of the SAEDpattern and the nanodisk is shown in Figure 3, parts A and B. (B) A typical SAED pattern of silver nanodisk at 100 kV in the [011] orientation (side view). (Ref. 171)

The sensitivity of small nanoparticles to experimental and environmental conditions makes their characterization via electron microscopy or optical techniques difficult. In spite of these limitations, some high-resolution transmission electron microscopy (HRTEM) studies have been performed on nanoparticle seeds, but have not yet been able to distinguish seed crystal structure as the driving force of anisotropic crystal growth. HRTEM data from Pileni *et al.*[171] suggests that stacking faults parallel to the {111} crystal planes are responsible for plate-like

growth of Ag nanostructures (nanodisks) (Figure 1.17). Indeed, crystal twin planes parallel to the major {111} faces are frequently observed in the final disks (in both the TEM and diffraction images), as well as during the early stages of nanodisk growth. The authors claim that varying the degree of crystal twinning is critical to controlling the final morphology of the nanostructures, although no detail is given as to possible experimental methods to do so. Similarly, Murphy *et al.*[172] have reported that Au nanoparticle seeds containing five-fold twinning exhibited growth to form Au nanorods whereas single crystalline seeds did not.

More recently, Xia and coworkers have demonstrated that the crystal structure of Ag nanoparticles prepared by a polyol method can be modified based on the nature of the salt added to the reaction mixture.[89, 147] In 2005, the authors reported that addition of NaCl or HCl to a solution of $AgNO_3$, PVP, and ethylene glycol yield single crystalline nanoparticle seeds upon 30 minutes of refluxing (160 ºC).[89] Additional refluxing of the mixture yielded single crystalline Ag nanocubes. In their more recent report, the authors found that replacing NaCl with NaBr resulted in the formation of Ag nanoparticle seeds (containing a single twin plane after 1.5 hours of reflux. After 5 hours of refluxing, these twinned seeds (diameter ~ 15 nm) yielded Ag right bipyramids (edge length ~ 150 nm). Interestingly, the authors note that the seed nanoparticles contain a single twin plane that may allow growth of the right bipyramids.

Liu and Guyot-Sionnest have reported a comprehensive study of the effect of seed crystal structure on the final nanostructure morphology.[78] In their report, the authors prepared gold nanoparticle seeds via two methods and examined the crystal structure of each type. Seeds *I* were prepared via the synthesis outlined by Nikoobakht and El-Sayed[77] whereas seeds *II* were synthesized via that described by Murphy and coworkers.[75] HRTEM analysis revealed that the two preparative routes yielded seeds with very different crystal structures. Seeds *I* were single

crystalline (diameter ~ 1.5 nm) whereas seeds *II* were twinned with pentagonal symmetry. Each batch of seeds were subsequently exposed to a Ag(I)-assisted growth solution (comprised of $HAuCl_4$, $AgNO_3$, CTAB, HCl, and L-ascorbic acid) and their final morphology evaluated. Interestingly, Au nanostructures derived from seeds *I* underwent one-dimensional growth to form Au nanorods with various aspect ratios. In contrast, seeds *II* displayed growth to form bipyramidal structures in high yield (Figure 1.18). The authors conclude that the seed structure is, in fact, governing the shape and crystal structure of the final nanostructures.

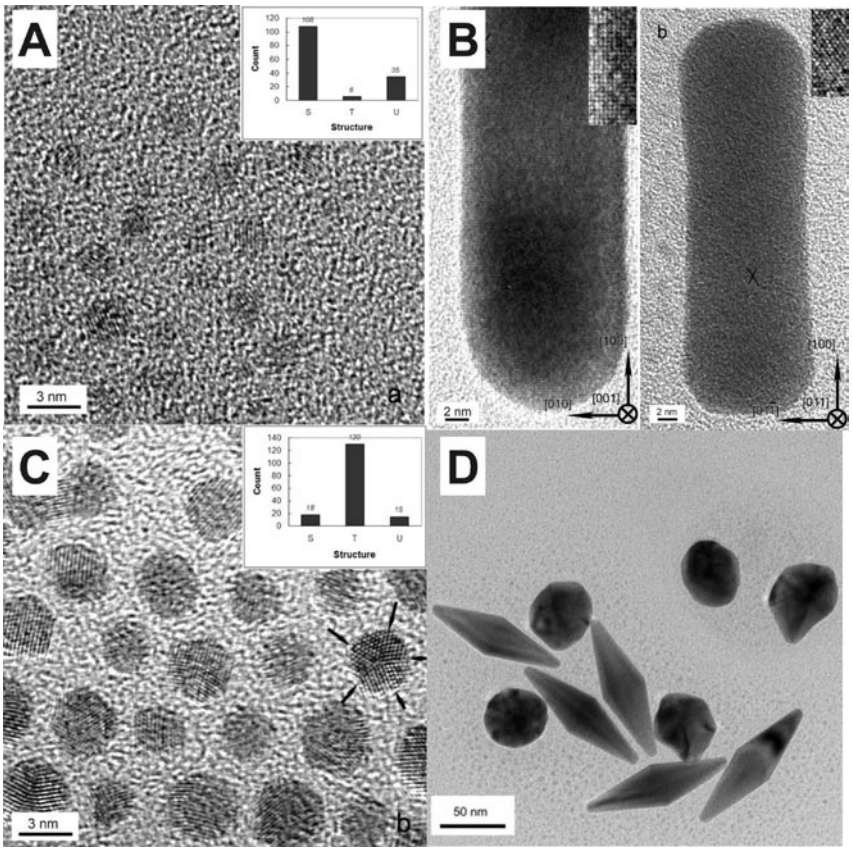


**Figure 1.18** (A) HRTEM image of Au seeds I. (B) HRTEM images of Au nanorods grown from Au seeds I with Ag(I). The nanorods are aligned in [001] (left image) and [011] (right image) directions. The insets show 2x magnifications of the areas labeled by the black crosses. The dimensions of the insets are 2 x 5 nm for panel a and 2 x 4.6 nm for panel (C) HRTEM image of Au seeds II. Twinned planes are indicated by arrows. In the histograms (n = 150) S, T, and U stand for single crystalline, twinned, and unidentified nanoparticles, respectively. (D) TEM image of Au nanostructures grown from Au seeds II with Ag(I). (Ref. 78)

Although these reports demonstrate that stacking faults are present in the final structure, they do not reveal what types of crystal twins lead to plate-like (or other anisotropic)

morphologies. Indeed, unless anisotropic growth of the initial seed particles is observed *in situ*, it is difficult to predict what nanoparticle morphology will lead to platelike crystal growth. In addition, a detailed analysis of the experimental parameters that control crystal twinning (e. g. number of twins and orientation) has yet to be reported. Such studies are critical to a better understanding of plate-like crystal growth.

### 1.7.2 Chemical Methods and Redox Chemistry Arguments

Despite a compelling argument that the crystal structure of the nanoparticle seed is a determining factor in platelike growth, it is also true that the same seed particles can, in some cases, yield various morphologies depending on reaction conditions such as surfactant concentration, metal ion concentration, reducing agent concentration, and metal or halide ion additives.[77, 79, 90, 129, 165, 173-175] That different nanoparticle morphologies can be obtained from the same nanoparticle seed indicates that the reduction method and chemical environment for crystal growth can also be critical factors in determining the final shape and size of a nanoparticle. For example, Scheme 1.4 illustrates "face-blocking" which bridges crystallographic and redox chemistry theories. In this mechanism, surfactant selectively adsorbs to the most favorable crystal facet where "favorable" is determined by either surface reactivity (as dictated by crystal facet) or surface charge (as dictated by capping ligand).[61, 175] It is thought that once bound, these capping molecules significantly or completely block reduction of metal ions onto the surface of the growing nanocrystal. This explanation is common to the vast majority of proposed mechanisms for the role of a particular capping ligand.[34, 80, 99] One representative study is the work of Murphy *et al.*[90] which showed that the morphology and dimension of Au nanoparticles produced in a particular aqueous thermal methodology depended strongly on the concentrations of the seed particles and CTAB, in addition to the concentration of

gold ions ($Au^{3+}$) and reducing agent (ascorbic acid). All of the above factors were found to be interdependent, and gave rise to a variety of shapes depending on combination (Table 1). For example, high surfactant concentrations produced rectangular nanorod structures, whereas lower surfactant concentrations of surfactant mixture produced pentagonally-twinned nanorods, triangles, and pseudo-spherical particles. A combination of crystal blocking theories were used to explain these variations, which have continued to be the subject of significant investigation.[34, 78, 79, 91, 103, 165-167, 176-178] This work highlights a number of the most common observations and explanations regarding the interplay of seed, surfactant, metal ion, and reducing agent concentrations, and demonstrates the still limited understanding of the role of these parameters.

A particularly promising advance in understanding the chemical factors that influence platelike growth has been the elucidation of the role of halide ions in the aqueous thermal syntheses of gold anisotropic materials. In 2006, Sastry *et al.* reported the suppression of gold nanoprism growth with the addition of iodide ion ($I^-$).[166] Here, the authors added mM concentrations of KF, KCl, KBr, and KI to an aqueous mixture of gold ions and lemongrass extract. The presence of $Cl^-$ was found to produce the highest yield of nanoprism structures, and propose that because chloride ions do not introduce interfacial strain on the Au surface when they adsorb, there is no driving force to change the “original” growth pattern into nanoprism structures. In contrast, Ha *et al.* report that the presence of $I^-$ promotes nanoprism formation when used in aqueous synthesis with the CTAB and ascorbic acid as a reducing agent.[165] In recent work also on CTAB-based, aqueous seed-mediated Au nanoprism syntheses, we have reported that CTAB, depending upon supplier, can contain an iodide contaminant which acts as a key shape directing element. In this study, we also demonstrate that by starting with pure CTAB and deliberately adjusting iodide concentration, one can reproducibly drive the reaction to

| [CTAB]/M | $[Au]_{seed}$/M | $[Au^{3+}]$/M | [AA]/M | Shape/Profile | Dim |
|---|---|---|---|---|---|
| $1.6x10^{-2}$ | $1.25x10^{-8}$ | $2.0x10^{-4}$ | $6.0x10^{-3}$ | Cube | 6 |
| $1.6x10^{-2}$ | $1.25x10^{-8}$ | $2.0x10^{-4}$ | $3.0x10^{-3}$ | Hexagon | 7 |
| $1.6x10^{-2}$ | $1.25x10^{-7}$ | $2.0x10^{-4}$ | $6.0x10^{-3}$ | Triangle | 3 |
| $1.6x10^{-2}$ | $1.25x10^{-8}$ | $4.0x10^{-4}$ | $6.4x10^{-4}$ | Cube[a] | 9 |
| $9.5x10^{-2}$ | $1.25x10^{-7}$ | $4.0x10^{-4}$ | $6.0x10^{-3}$ | Tetrapod[a] | 3 |
| $1.6x10^{-2}$ | $1.25x10^{-8}$ | $4.0x10^{-4}$ | $1.2x10^{-2}$ | Star | 6 |
| $5.0x10^{-2}$ | $6.25x10^{-7}$ [b] | $5.0x10^{-4}$ | $3.0x10^{-3}$ | Tetrapod | 29 |
| $9.5x10^{-2}$ | $2.5x10^{-7}$ | $4.0x10^{-4}$ | $6.4x10^{-4}$ | Branched[a] | 17 |

**Table 1.** Shapes of gold particles and corresponding reaction conditions. (Ref. 90)

predominantly produce either pseudo-spherical nanoparticles, nanorods, or triangular nanoprisms (cf. Chapter 6).[167]

The dependence of nanoparticle morphology on iodide concentration may be understood based on the preferential adsorption of iodide on {111} crystal facets of Au.[149] Without iodide, a CTAB bilayer is present on all surfaces due to electrostatic forces, which leads to a lack of preferential growth and an isotropic nanoparticle. When the iodide concentrations is slightly increased iodide adsorbs on the {111} crystal facets (at the ends of the rods), leaving the {110} and {100} (the long axis facets of the rod) open for the adsorption of a close-packed CTAB layer that can limit the reduction of gold ions at these sites.[61, 175] This model is consistent with previous observations for rod formation and offers additional insight into why growth in the [111] direction can compete effectively to form nanorods.[61, 175] At elevated concentrations of iodide ($25 < x < 75$ μM, a layer of iodide is formed on the Au surface (as indicated by XPS, $I_{3d}$ = 618.9eV).[167, 179] This layer may promote nanoprism formation by allowing the chemical reactivity of the different crystal facets to dominate the growth processes with growth at the high energy side crystal facets favored.[104] Taken together, this model presents a series of competing factors for directing anisotropic nanoparticle growth where iodide plays the primary mediating role.

These studies help to elucidate the shape-directing factors involved in a subset of aqueous thermal syntheses that use CTAB and are seed-mediated. However they may also be useful in illustrating the ways in which the interplay between crystallographic factors and chemical reaction conditions can be modulated to achieve a desired nanoparticle shape.

**1.8 Dissertation Overview**

In the previous sections it has been shown that there are numerous methods to access nanoprism structures and that once made, there are a variety of interesting chemical and optical features that can observed, studied, and potentially used in applications ranging from catalysis[180] to spectroscopic enhancement[145] to therapeutics.[27] In order to bridge the gap between current synthetic preparations and envisioned applications, it will be first necessary to consistently understand the factors that determine nanoprism formation in solution and to fully characterize the crystallographic, optical, and chemical features of the resulting particles. This dissertation describes developments in these areas as they are related to Au nanoprisms prepared by aqueous thermal methodologies.

In Chapter 2, a three-step, CTAB-based, seed-mediated growth process is presented for the production of colloidal gold nanoprisms with relatively homogeneous size distributions. This synthetic approach builds on previous methods used to generate colloidal anisotropic nanoparticles made of gold, and offers synthetic advances for the high yield production of Au nanoprisms in complement to their Ag counterparts. The purity of nanostructures produced in this synthesis allows the observation of a weak quadrupole SPR in addition to a strong dipole SPR associated with the Au nanoprisms. The experimental optical spectra agree with discrete dipole approximation calculations that have been modeled from the dimensions of gold

nanoprisms produced in this synthesis, and a detailed analysis of the resulting quadrupole is presented.

Chapter 3 builds on the previous work by describing a method for controlling Au nanoprism edge length. A straightforward method for controlling and reinitiating the growth of single crystalline gold nanoprisms is presented. The approach is based on seeding methodology and depends on the slow reduction of metal ions onto the surface of a growing nanoparticle. In this manner, the edge length of gold nanoprisms is tailored over a range of 100 – 300 nm without changing nanoprism thickness or crystallinity. Each size of nanoprisms has been characterized by UV-vis-NIR spectroscopy, transmission electron microscopy (TEM) techniques, and statistical analysis. Based on this work and existing silver halide crystal growth theories, a preliminary mechanism is proposed which comments on the interplay between crystal growth and surface chemistry that ultimately dictates the morphology of the resulting nanostructure in this system. The nanostructures reported here give new insight into anisotropic gold nanoparticle growth and reactivity, and present an expanded library of prism structures with optical features ranging from 1000 – 1800 nm.

In Chapter 4, the site-selective chemical reactivity of the Au nanoprisms described in Chapter 3 is used to investigate the functionalization of the nanoprism and elucidate its surface chemistry. In this work, DNA-conjugated gold nanoprisms have been synthesized and investigated in order to determine the factors that allow one to adsorb alkylthiol-modified oligonucleotides onto different facets of an anisotropic gold nanoparticle. In this section, it will be shown that face-selective, DNA-ligand adsorption processes are time dependent, and can be exploited to tune the selective immobilization of DNA on the edges of the particle. These results

are confirmed both chemically (using elemental spectroscopy) and qualitatively (by subsequent assembly events).

Chapter 5 builds on the methods and techniques developed in Chapter 4 to make and use a variety of DNA-functionalized anisotropic nanostructures. For example, this chapter describes the use of such conjugates in applications including biodetection, wherein nanodisk arrays are used as barcodes to readout the presence of target moieties. This chapter also addresses gene delivery and gene therapy applications of oligonucleotide-modified Au nanoprisms by describing the preparation and uptake DNA-nanoprism conjugates for transfection into cells.

Chapter 6 describes the most recent work completed on the shape-directing factors in the synthesis of Au nanoprisms. In fact, a variety of preparatory procedures for gold nanorods, triangular prisms, and spheres that use similar synthetic approaches now exist. Many of these methods, including the synthesis of Au nanoprisms, rely on seed-mediated approaches with CTAB as a surfactant. Interestingly, seemingly similar preparatory procedures yield very different morphologies, and although there have been a variety of proposals regarding the importance of different steps in shape control, there is no procedure that allows one to take a single batch of spherical seeds and grow either rods, prisms, or larger polyhedra in a controlled manner. In this chapter, it is shown that CTAB, depending upon supplier, has an iodide contaminant (at a significant but varying level), which acts as a key shape directing element, because it can strongly and selectively bind to the gold (111) facet and favor the formation of anisotropic structures. Furthermore, by starting with pure CTAB and deliberately adjusting iodide concentration, one can reproducibly drive the reaction to predominantly produce one of the three target morphologies.

# CHAPTER TWO

Observation of a Quadrupole Plasmon Mode from a Colloidal Solution of Gold Nanoprisms

Portions of this chapter were published previously in**:** *J. Am. Chem. Soc.*, **2005**, *127*, 5312.

## 2.1 Introduction

The use of nanostructured materials in applications such as biodetection[13], catalysis[12, 38, 181, 182], and electronics[183, 184] has led to an explosion of interest in the development of synthetic methods for preparing such structures. The majority of effort thus far has focused on isotropic, pseudo-spherical structures, but recently, researchers have made promising advances that are yielding control over particle size, shape, and composition.[45, 77, 108, 121] These architectural parameters dictate the physical and chemical properties of a nanostructure.[185] Triangular nanoprisms, in particular, are a class of nanostructures that have generated intense interest due to their unusual optical properties, and the recent development of new methods for preparing bulk quantities of them.[45, 48, 81, 83-85, 104] Depending upon composition and desired dimensions, certain types of prisms can be prepared by either thermal or photochemical methods.[45, 48, 81, 83-85, 104] Thus far, the photochemical routes have been used to synthesize silver nanoprisms with excellent size control. Gold nanoprisms, on the other hand, have been synthesized exclusively by thermal methods with varying degrees of success regarding purity and size control.[85, 134]

The optical spectra of nanoprisms should exhibit a distinct dipole resonance as observed in isotropic spherical structures in addition to weaker higher order resonances.[36] In the case of silver, where bulk preparations of high quality and relatively pure nanoprisms can be realized, these plasmons have been identified and assigned through experiment and computation.[45] To the best of our knowledge, no one has experimentally identified a quadrupole plasmon resonance for colloidal solutions of gold nanoprisms. Such structures should exhibit quadrupole resonances as evidenced by their identification in lithographically patterned analogues.[186] The identification of higher order surface plasmon resonance modes with other metal nanoparticles is important because it not only provides greater understanding of their physical properties, but also a

spectroscopic fingerprint that can be used to characterize and assess the quality of such structures. Herein, we discuss a synthetic approach and separation procedure for synthesizing and isolating large quantities of gold nanoprisms with uniform edge lengths and thicknesses, which has allowed us to use UV-vis-NIR spectroscopy to observe an in-plane quadrupole resonance mode of such structures for the first time.

## 2.2 Experimental

### 2.2.1 Synthesis of Gold Nanoprisms

In a typical experiment, all glassware is washed with aqua regia (3:1 ratio by volume of HCl and $HNO_3$), and NANOpure™ water (18.2 MΩ). ***Hazard:*** *aqua regia is highly toxic and corrosive and must be handled in fume hoods with proper personal protection equipment.* Cetyltrimethylammonium bromide (CTAB, 95%), hydrogen tetrachloroaurate trihydrate ($HAuCl_4$•$3H_2O$, 99.9%), sodium borohydride ($NaBH_4$, 99.995%), sodium hydroxide (NaOH, 99.998%), L-ascorbic acid (99%), and trisodium citrate (99%) are obtained from Aldrich and used as received. NANOpure™ water (18.2 MΩ) is used in the preparation of all reagents and throughout all synthetic steps.

This synthetic procedure builds off of the work of Murphy et. al.,[187] and involves the preparation of small gold seed nanoparticles (d ≈ 5.2 ± 0.6 nm) and the subsequent three-step growth of seeds in an aqueous solution containing the capping agent (cetyltrimethylammonium bromide (CTAB)), gold ions, reducing agent (ascorbic acid), and NaOH). Gold nanoparticle seeds are prepared by reducing 1 mL of a 10 mM aqueous solution of $HAuCl_4$ with 1 mL of a 100 mM aqueous solution of $NaBH_4$ while stirring vigorously. The reduction is done in the presence of 1 mL of a 10 mM aqueous solution of sodium citrate and 36 mL of NANOpure water. Upon addition of the $NaBH_4$, the solution turns a reddish orange color and is allowed to

continue stirring for one minute. The resulting mixture is aged for 2-4 hours to allow the hydrolysis of unreacted $NaBH_4$. The gold nanoparticle seeds exhibited a plasmon resonance peak at 500 nm, and had an average diameter of 5.2 ± 0.6 nm (Figure 2.1).

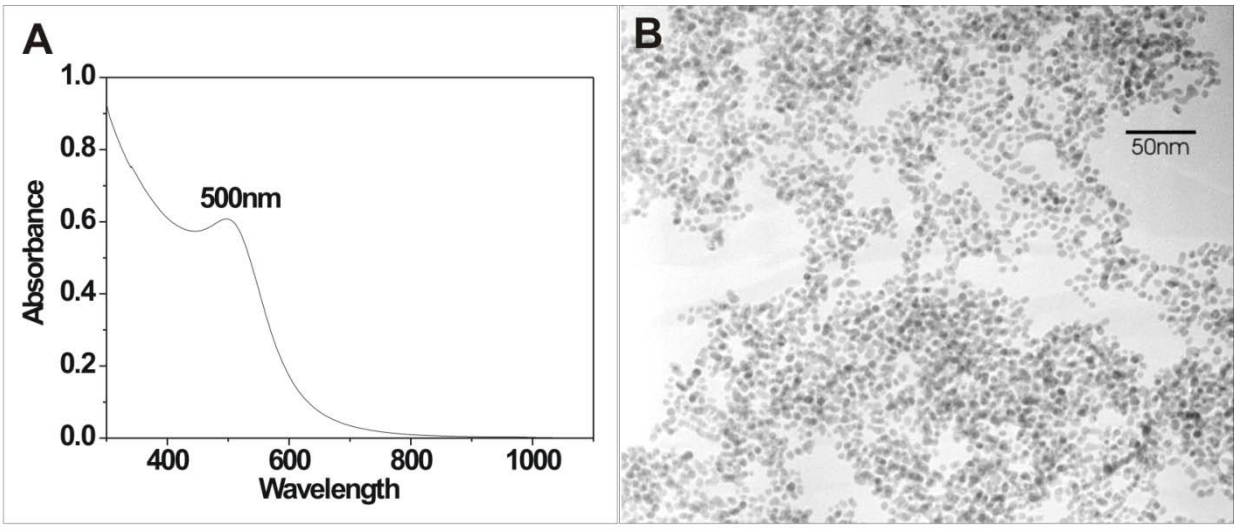


**Figure 2.1** (A) UV-Vis spectrum and (B) corresponding TEM image of gold nanoparticle seeds.

After the aging period, three growth solutions were prepared for use in the seed-mediated growth step. The first two solutions (**1** and **2**) contained 0.25 mL of an aqueous solution of 10 mM $HAuCl_4$, 0.05 mL of an aqueous solution of 100 mM NaOH, 0.05 mL of an aqueous solution of 100 mM ascorbic acid, and 9 mL of a saturated CTAB solution. The final growth solution (called **3**), contained 2.5 mL of an aqueous solution of 10 mM $HAuCl_4$, 0.50 mL of an aqueous solution of 100 mM NaOH, 0.50 mL of an aqueous solution of 100 mM ascorbic acid, and 90 mL of an aqueous solution of saturated CTAB. Prism formation was initiated by adding 1 mL of seed solution to growth solution **1**. Approximately two seconds after this addition, one mL of growth solution **1** was then added to **2**. After two additional seconds, all of the resulting growth solution in **2** was added to **3**. After the addition, the color of **3** changed from clear to deep magenta-purple over a period of 30 minutes. The seed-mediated growth reaction of the nanoparticles have been characterized by ultraviolet-visible-near infrared spectroscopy (UV-vis-

NIR) using a Cary 5000 spectrophotometer. All nanostructures have been characterized using a Hitachi-8100 transmission electron microscope (TEM) or JEOL-2100 TEM at 200kV.

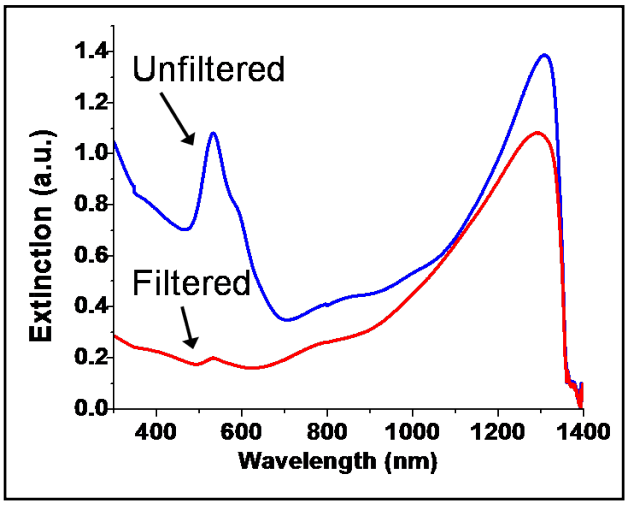


**Figure 2.2** UV-vis-NIR spectra comparing solutions of filtered and unfiltered Au nanoprisms.

### 2.2.2 Purification of Gold Nanoprism Reaction Solution

As made, the nanoprism solution contained a mixture of gold nanoprisms and pseudo-spherical nanoparticles (65% and 35% yield, respectively). Because these two types of particles are different in both weight and shape (40 nm AuNP ≈ 2 x $10^6$ atoms; 150 nm edge length nanoprism ≈ 4.3 x $10^6$ atoms) they could be separated by a variety of methods including centrifugation, filtration, and sedimentation. The most effective methods (methods that yield > 95% pure nanoprisms) were filtration and sedimentation, and are described below.

#### 2.2.2.1 Filtration

Filtration of the nanoprisms can be achieved using an aluminum oxide filter with 100 nm diameter pores (Whatman, Inc.). This filter is used to separate an as-made reaction mixture of Au prisms by eliminating particles smaller than 100 nm which include the pseudo-spherical gold particles and smaller gold nanoprisms seen in this synthesis. After filtration, the retentate was collected by sonciating the used alumina oxide filter in 1 mL of NANOpure™ water for 20 seconds. The filter was then removed from the solution, and the remaining aqueous mixture contained the filtered sample of gold nanoprisms. Prisms could be collected by centrifugation at 8000 RPM for 3 minutes using an Eppendorf Model 5145D Centrifuge (Figure 2.2, Scheme 2.1).

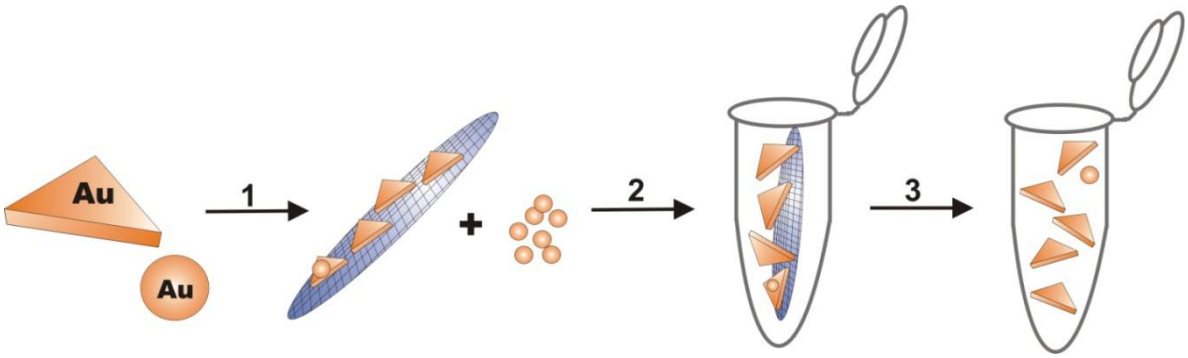


**Scheme 2.1** Filtration of Au nanoprism solution using Whatman AAO filter with 100 nm pore diameters. Step 1 involves isolating nanoprisms on the filter surface, while pseudo-spherical nanoparticles and small nanoprisms are pass through the filter and are discarded. In step 2, the filter is placed in an eppendorf tube that contains 1 mL of NANOpure™ water, and is briefly sonicated to remove the nanoprisms from the template surface. In step 3, the template is removed, and prisms are isolated in solution.

#### 2.2.2.2 Sedimentation

After the nanoprism reaction was complete, the final solution could be aliquoted into 1.5 mL centrifuge tubes. These tubes were allowed to stand in a rack overnight on the benchtop (light exposure is not a significant source of degradation, *vide infra*). After 12 h, prisms had settled to the bottom of the tube while the lighter, pseudo-spherical nanoparticles remained in solution. Using the small centrifuge tubes allowed both simple identification and separation of these two components. Upon observing separation, the supernatant of the solution was removed and discarded while the pellet was resuspended in water.

## 2.3 Results and Discussion

### 2.3.1 Empirical Characterization of Nanoprism Structure

As described in the experimental section, this synthetic procedure produces a mixture of spherical and triangular gold nanoparticles, each with a relatively homogeneous size distribution (Figure 2.3A). In contrast with many other similar synthetic routes for gold nanostructures

utilizing CTAB, our synthetic method produced no rods, cubes, or branched structures.[90] The histogram in Figure 2.3C represents the edge-length size distribution of the nanoprisms. The average edge length of the nanoprisms is 144 ± 30 nm. The average pseudo-spherical nanoparticle diameter is 35 ± 2 nm. Interestingly, electron diffraction analysis of an individual gold nanoprism shows that, unlike lithographically generated structures, they are single crystalline, and that the large, flat top and bottom faces are {111} facets (Figure 2.3B). Atomic force microscope (AFM) images of the gold nanoprisms confirm that their top and bottom faces are atomically flat with a uniform thickness of 7.8 ± 0.5 nm (13 prisms studied, Figure3D and inset). This thickness is approximately equal to the average diameter of the seed nanoparticles when the thickness of the two layers of CTAB on the top and bottom surfaces of nanoprisms are taken into account. This suggests that growth of prisms occurs in two dimensions from the isotropic seed to form the anisotropic prism.

The nanoprism growth process has been monitored in real time by UV-vis-NIR spectroscopy (Figure 2.4). The spectra clearly reveal two distinct bands, the first of which appears at 532 nm and indicates the presence of spherical particles (35 ± 2 nm, Figure 2.3A). The position of this band does not change significantly with time. This band is assigned to the dipole resonance associated with the spherical gold nanoparticles, and its intensity correlates with the concentration of gold nanoparticles in solution. A second band is observed initially at 750 nm, which red-shifts as the growth process continues. This band is assigned to the dipole resonance of the gold nanoprisms and at the end of the growth process appears in the NIR at 1296 nm in conjunction with another band that appears at 814 nm. The shift of $\lambda_{max}$ most likely reflects an increase in nanoprism edge length.[36] The assignment of this shift in dipole resonance as a

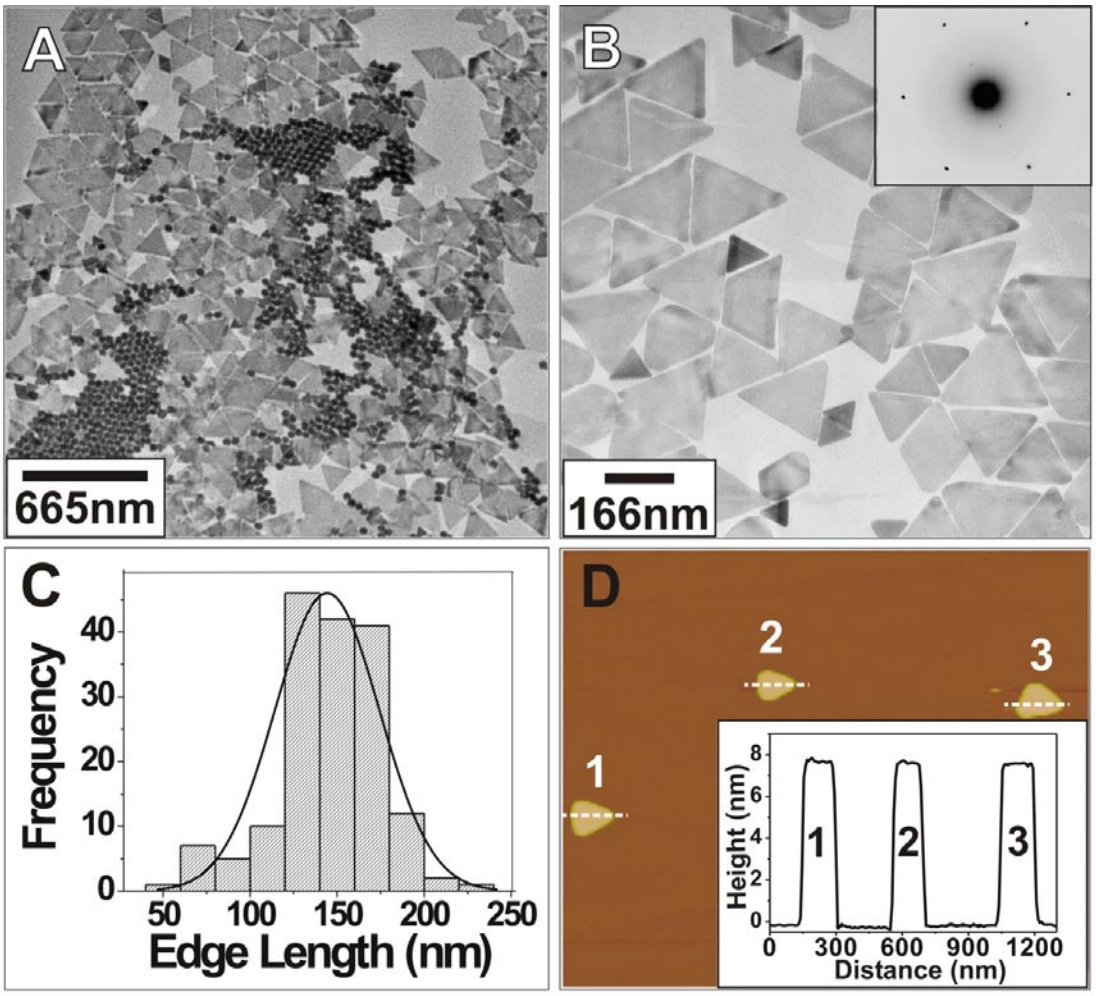


**Figure 2.3** (A) TEM image of Au spherical and triangular nanoparticles. (B) Zoom-in image of nanoprisms. Inset shows the electron diffraction pattern of the top surface of a single prism. (C) Histogram showing the distribution of nanoprism edge lengths. (D) AFM image of nanoprisms on mica (tapping mode). Inset: height profile along the dashed lines.

function of time and concomitant increase in edge length is consistent with theoretical calculations and our isolation of the final nanoprism product (*vide infra*). After 30 minutes the reaction stops as indicated by fixed dipole plasmon resonances at 532 nm for the spherical particle products and ~1300 nm for the nanoprisms. These bands do not increase in intensity after this point, even after three months in the growth solution. Interestingly, when the nanoprisms are predominantly separated from the spherical particles, one clearly sees a broad

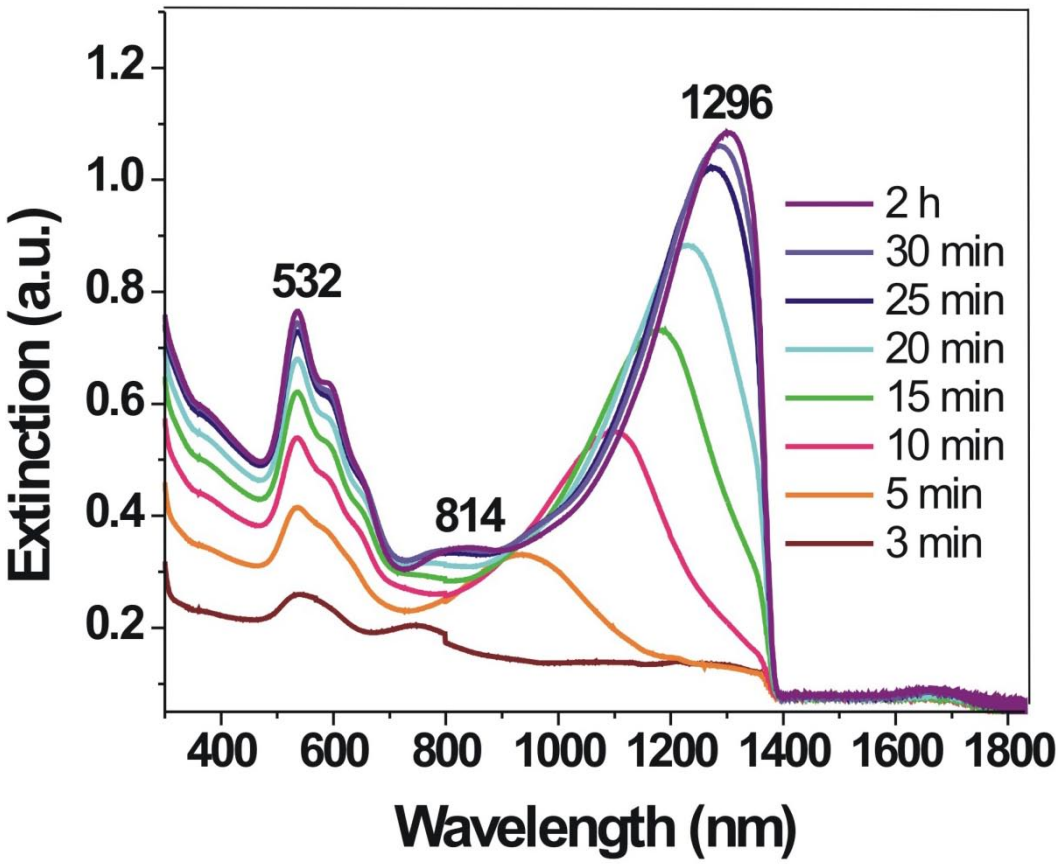


**Figure 2.4** In-situ UV-vis-NIR spectra following the formation of gold nanoprisms after seed addition.

band in their UV-vis-NIR spectrum at 800 nm, which we assign to the in-plane quadrupole mode of the nanoprisms (Figure 2.5). This assignment is based upon the characterization of these prisms by electron microscopy, and on discrete dipole approximation (DDA) calculations,[188] which predict plasmon bands that match experiment. Attempts to investigate intermediate sizes and shapes by TEM do not reveal homogeneous nanoparticle distributions, but rather often showed irregular nanoparticle shapes and sizes. This experiment was complicated by the inability to definitely arrest the growth process during sample isolation and preparation. Similar

results were reported by others and have been attributed to the reactive nature of the gold intermediate structures in the solution.[189]

### 2.3.2 Characterization of Nanoprism Quadrupole Plasmon Resonance

A UV-vis-NIR spectrum (**I**) of the purified Au nanoprisms and a corresponding simulated spectrum obtained by DDA calculations (**II**) are in excellent agreement (Figure 2.5B). An in-plane dipole band with $\lambda_{max} \approx 1300$ nm is observed in both spectra, as is a quadrupole band occurring at $\lambda_{max} \approx 800$ nm. The theoretical spectrum presented in trace **II** reflects the experimentally derived size distribution of gold nanoprisms in solution. DDA calculations have been performed on nanoprisms with a width of 7.5 nm and effective edge lengths of 90, 110, 130, 150, 170, 190, and 210 nm. The contribution of each of the prisms in the set was then weighted according to a Gaussian fit of the relative particle populations in solution like that shown in Figure 3C. The weighted cross sections of these spectra were summed to form trace **II**.

The calculated spectrum is based on gold dielectric constants taken from Lynch and

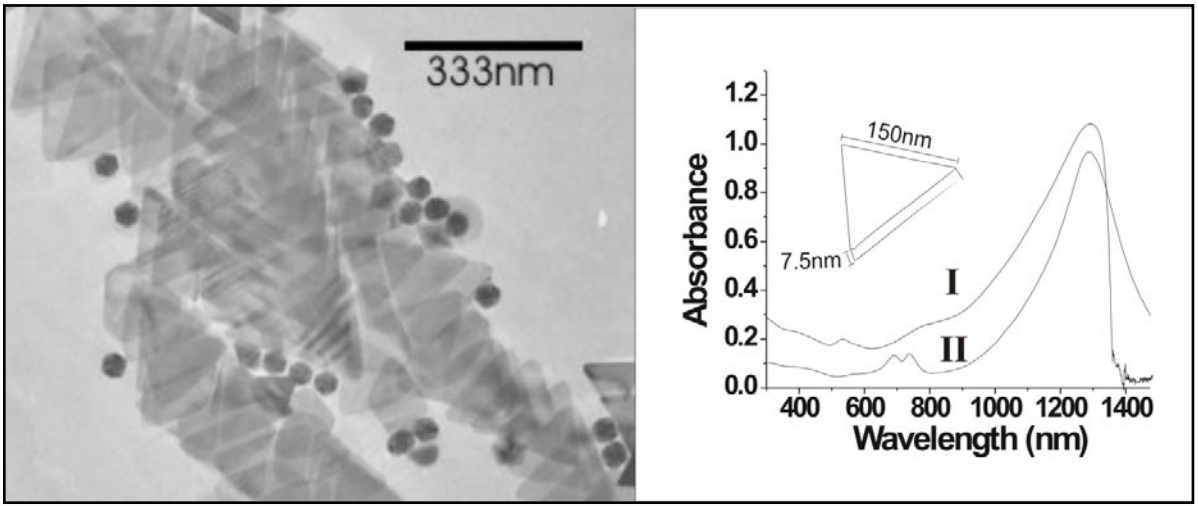


**Figure 2 5** (A) TEM image of the purified Au nanoprisms. (B) Corresponding UV-vis-NIR spectra of purified Au nanoprisms (**I**) and DDA calculation (**II**). Inset: the physical dimensions of a nanoprism used in the DDA calculation.

Hunter.[190] In particular we use their tabulated values from Theye[191], and not from Dold and Mecke.[192] The spectrum presented in Trace **II** of Figure 2.5B is a spectrum reflecting a weighted average of prism edge lengths; a distribution which was derived from experimentally determined histograms of effective triangle edge length, e.g. Figure 2.3C. The spectrum also reflects the real shape of the triangular nanoprisms in solution, rather than a perfect prism shape approximation. The experimentally derived nanoprisms have slightly rounded edges which we call "snipped." In all calculations then, we have chosen to snip the vertices of perfect triangular prisms in order to accurately represent the particles in solution. In each prism calculation, 25 nm has been removed from each point giving an effective edge length that is 50 nm shorter than the corresponding perfect prism.

In the assignment of the quadrupole resonance, the possible contributions from nanoprisms of smaller edge lengths have been considered. DDA calculations modeling relative populations of each prism length show that the intensity of the quadrupole resonance from large prisms is much greater than the intensity of the dipole resonance of any remaining small edge length prisms in solution. The asymmetry of the experimental dipole resonance peak nm is due to the truncation of the peak by the absorbance of water in the IR region. It should be noted that additional calculations also showed that the in-plane dipole resonance peak at ~1300 nm is very sensitive to the physical dimensions of Au nanoprisms, as it is in the case of Ag nanoprisms.[36, 108] The in-plane quadrupole is also affected by those variations, but less sensitively. For example, the resonance bands (either of Ag or Au) redshift with increase in edge length and sharpness, and decrease of thickness.[36, 108],[110]

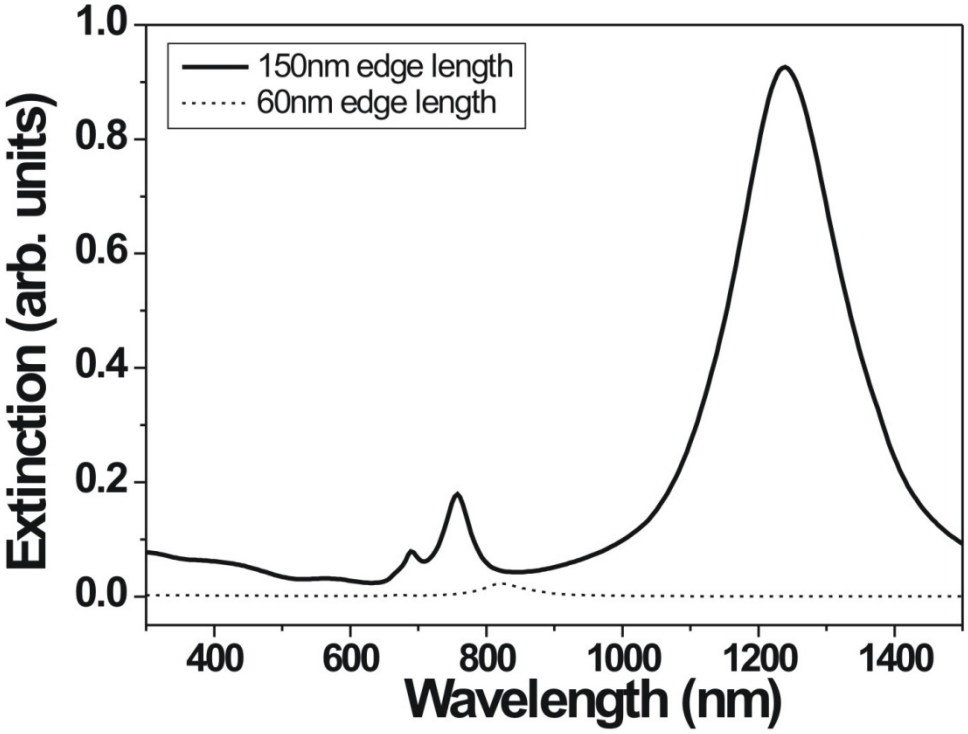


**Figure 2 6** Theoretical extinction spectra for prisms of varying edge length and 7.5 nm heights. Intensities have been scaled to represent the relative populations of a solution that is comprised of 15% small prisms (edge length = 60 nm), and 85% large prisms (edge length = 150 nm). This ratio of particle sizes corresponds to an experimental solution before separation which is the upper limit of potential small prism concentration in these experiments.

Figure 2.5B, Trace **I** shows the experimental spectrum from a solution of separated prisms. The spherical particle peak's absorbance at $\lambda_{max}$ = 532nm has decreased by ~95% from the peak's absorbance in the spectrum taken from the original, unfiltered solution (Figure 2.2). If the peak at ~800 nm was from smaller triangles (edge length <100 nm), we would expect to see a decrease of similar magnitude in this peak as well. However, we do not observe such a decrease.

Additionally, we assign the peak at ~800 nm to the quadrupole resonance of large gold prisms based on multiple DDA calculations that show how the relative intensities of the dipole and quadrupole modes depend on edge lengths. These spectra indicate that as the edge length of

the gold nanoprism decreases, its dipole resonance blueshifts and decreases in intensity. In order to determine whether the peak at ~800 nm was from the dipole resonance of these smaller prisms, or from the quadrupole resonance of the larger prisms, we compared the spectra of gold nanoprisms with effective edge lengths of 60 and 150nm (Figure 6). This simplistic representation of two particle sizes is sufficient to illustrate the significant differences in relative peak intensity. The prism particle cross sections were weighted to reflect their populations in solution before any filtration or purification. The intensity of the quadrupole plasmon resonance from larger prisms dwarves any possible contribution from the dipole resonances of smaller nanoprisms. The intensity from the smaller prisms relative to the intensity of larger prisms (under these "worst case" conditions) shows that it is unlikely for small prisms to contribute significantly to the peaks observed in our experimental spectra (Figures 2.4 and 5). In addition, it was found that including the smaller prisms in the accurately weighted spectrum (Figure 2.5B) does not alter the results. This is again because of the relatively small cross sections of small particles and the extremely small weighting coefficient produced from the Gaussian fit.

In analyzing the optical properties of the nanoprism solution we have considered the presence of smaller edge length nanoprisms, and the real prism size distribution in solution. In addition to these parameters, we have also considered the possible contribution of particle aggregation to the optical spectrum. In Figure 2.7, we show the UV-vis-NIR spectrum of a solution of gold nanoprisms as it undergoes aggregation by increasing salt concentration. We have tried to induce aggregation of the nanoprisms in order to determine if the origin of the ~800nm peak is from a distribution of aggregated particles. During the aggregation process we see a continuous decrease in the dipole peak intensity and a concomitant decrease in the quadrupole peak intensity which further indicates that the two peaks are correlated. If the

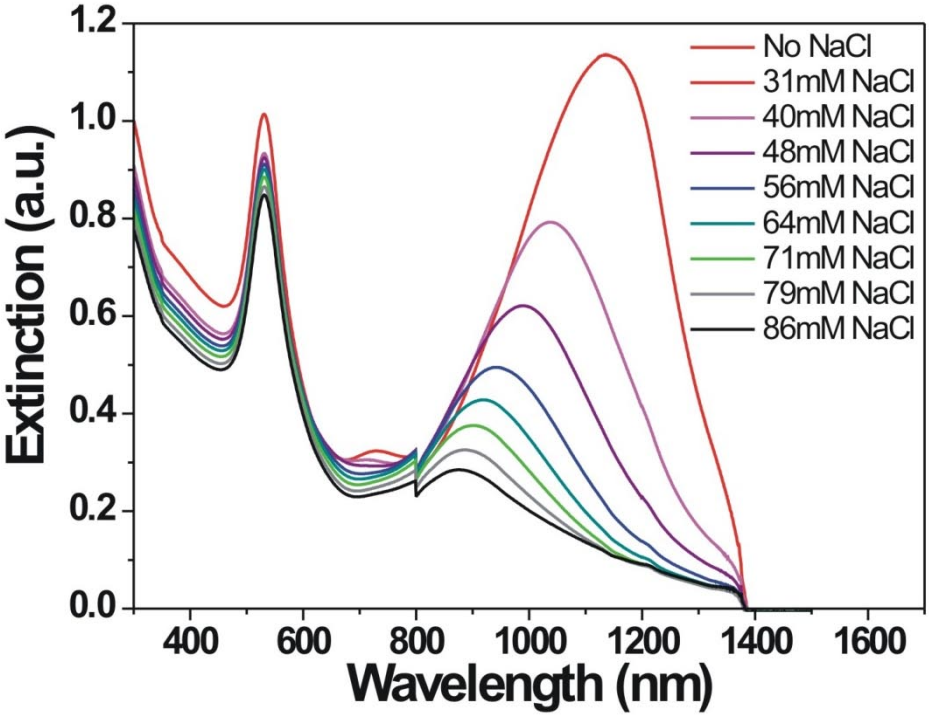


**Figure 2.7** UV-vis-NIR spectra of Au nanoprism solution during aggregation by slow addition of NaCl.

~800nm peak was from a suspended aggregate, one would expect to see an increase in the intensity of the 800nm peak as aggregation in solution increased. The absence of this peak increase further confirms that the peak at ~800nm is the quadrupole resonance of gold nanoprisms.

## 2.4 Conclusion

This chapter provides a method for synthesizing and isolating Au nanoprisms in their purest form. The purity of such materials has allowed us to correlate their structure with their optical properties and identify the quadrupole plasmon resonance, which has never been observed in solution because of inhomogeneity and impurities found in the products formed from other preparatory procedures. In view of the high stability of gold as compared with silver, these structures should provide a route to synthesizing many technologically useful materials as well

as provide insight into the formation and uses of colloidal anisotropic noble metal nanostructures.

# CHAPTER THREE

Controlling the Edge Length of Gold Nanoprisms via a Seed-Mediated Approach

Portions of this chapter were published previously in: *Adv. Funct. Mater.* **2006**, *16*, 1209.

### 3.1 Introduction

It is well-known that the physical and chemical properties of nanoparticles are largely determined by their composition, size, and shape.[34, 35] In the previous chapter, a new method for preparing Au nanoprisms was presented and their optical features were elucidated. Indeed, the strong correlation of nanoparticle architecture with nanoparticle properties could be clearly observed from the behavior of the nanoprism surface plasmon resonances as a function of nanoparticle size and shape. Because nanoparticle properties are dictated by these characteristics, it is essential to develop methods for controlling nanoparticle dimensions in order to both elucidate unique physicochemical properties and to integrate these nanostructures into emerging technologies. Size control has been established for many compositions of isotropic metal nanoparticles,[8, 51, 193, 194] and this control has allowed these structures to be used in a variety of applications ranging from biodetection[13] to catalysis.[6, 7, 10, 12] Prisms are a particularly interesting class of structures because of their unique optical features, and both thermal and photochemical routes have been developed for preparing bulk quantities of them.[45, 81, 85, 108, 195] Using the photochemical routes, one can control their dimensions through judicious use of plasmon excitation.[45, 108] On the other hand, methods for preparing gold nanoprisms have been exclusively thermal, and the monodispersity of the nanoprisms has been difficult to control.[81, 85] Only a handful of the reported methods demonstrate a degree of nanostructure size control, and there is little overlap between the synthetic approaches. The attractive feature of the Ag photochemical methods is that the reaction can be stopped and reinitiated with light at almost any stage. At present, there are no methods for controlling the edge length of Au nanoprisms that compare favorably to the photochemical methods for controlling edge length while maintaining the optical properties and tight size distribution of the original nanoprisms. Herein, we

demonstrate how a seeding methodology, developed initially for isotropic gold nanostructures by Natan,[52] can be used in the context of gold nanoprisms to initiate, stop, and reinitiate growth at almost any stage over a size range between 100 and 300nm. Based on these principles and our previous work with gold nanoprisms,[84] we have been able to grow nanoprisms (as defined by edge length) while maintaining their original shape, thickness, and crystallinity.

## 3.2 Experimental

### 3.2.1 Method for the Growth of Nanoprism Edge Length

All chemicals were obtained from Sigma-Aldrich and used as received. Prior to use, all glassware was washed with aqua regia (Caution: *aqua regia is highly toxic and corrosive*) and rinsed thoroughly with NANOpure water (Barnstead, 18.2 MΩ). The original gold nanoprism solution was made by literature methods (see Chapter 2).[19a] This prism mixture was then grown by serial addition of aliquots of gold ions ($HAuCl_4$, 0.01M) into the existing nanoprism solution in the presence of excess ascorbic acid. For these experiments, one growth step consisted of increasing the gold ion concentration by 20% and increasing the total volume of the reaction mixture by not more than 0.5%. Ascorbic acid was then added to the reaction mixture in 10-fold excess relative to the added gold ions. This addition increased the final solution volume by an additional 0.5%. Specifically, the first addition consisted of $HAuCl_4$ (50 µL, 0.01M) and ascorbic acid (50 µL, 0.1 M) and was added to a 10 mL aliquot of gold nanoprism solution followed by gentle agitation of the reaction mixture by shaking. This ratio of reagents was then called one “growth addition” and abbreviated “x1”. In total, this quantity and combination of reagents was called one “growth addition” and abbreviated “**x1**”. Subsequent growth additions are referred to as **x2 – x8** with each subsequent growth step corresponding to an addition of reagents equivalent to those described for **x1**. Over the next two months, solution **x1** could be

grown via additional growth steps (from **x2 - x8)** up to the desired size range. . Growth additions could be added as rapidly as one minute apart, and as slowly as two months apart. The resulting nanostructures were allowed to fully react for an additional hour after the last growth addition, after which point no further growth was observed. The growth could be initiated anytime within a two month period, without a significant effect on the outcome of the product. Throughout the growth experiments, surfactant concentration, gold nanoprism seed concentration (as determined by optical density), pH (8.0), and temperature (23ºC) were kept constant.

The resulting nanostructures were allowed to fully react for an additional hour after the last growth addition, after which point no further growth was observed. The resulting nanoprisms were characterized by ultraviolet-visible-near infrared spectrophotometry using UV-vis-NIR, and viewed using a Hitachi-8100 transmission electron microscope at 200kV (TEM). TEM samples were prepared by concentrating the nanoprism mixture using centrifugation (2 minutes at 8,000 rpm, Eppendorf 5145D, repeated twice). The supernatant was then removed and the pellet resuspended in 100 µL of NANOpure water). A 10µL aliquot of this solution was drop cast onto a Formvar- coated Cu grid. High resolution TEM and EELS images were taken using a JEOL-2100 TEM at 200kV, and used the same sample preparation techniques as described for standard TEM.

## 3.3 Results and Discussion

### 3.3.1 Growth Method and Nanoprism Optical Features

To control nanoprism edge length, a seed batch of nanoprisms was first prepared using as described previously.[84] Briefly, the nanoprisms are made by serial addition of citrate-capped, pseudo-spherical gold nanoparticles (called “seeds”, d ≈ 5.2 ± 0.6 nm) into three separate growth solutions containing surfactant (cetyltrimethylammonium bromide (CTAB)), gold ions

($HAuCl_4 \cdot 3H_2O$), reducing agent (ascorbic acid), and NaOH. After addition to the third growth solution, the initial synthesis is complete. For the growth experiments described herein, we refer to this time point as "$t_0$" or the beginning of nanoprism growth. From $t_0$, without additional reagents, the color of the solution changes from colorless to deep magenta-purple over a period of 30 minutes. This reaction produces a solution of nanoprisms (65% yield) and pseudo-spherical nanoparticles. These pseudo-spherical nanoparticles form concomitantly with the nanoprisms, and make-up < 5% of the total particle mixture after purification (see Chapter 2, Section 2.2). Following the growth procedure described in Section 3.2, solutions of nanoprisms with varying edge lengths were produced. These experiments were monitored by UV-vis-NIR, which demonstrate signigicant changes in both the position and intensity of the optical features from the resulting colloids. Figure 3.1 displays UV-vis-NIR spectra of the optical features from gold nanoprisms after 2, 4, 6, and 8 additions of $HAuCl_4$ and ascorbic acid. We know from our previous work that peak **I** represents the dipole resonance of the gold nanoprisms, peak **II** represents the quadrupole resonance of the nanoprisms, and peak **III** represents the dipole resonance of pseudo-spherical nanoparticles that form concomitantly.[84] The optical spectra suggest that with successive additions there is a gradual red-shift of both the nanoprism dipole and quadrupole resonances. However, it becomes difficult to reliably monitor both the position and the intensity of the dipole resonance beyond 1400 nm due to the absorbance of water. Therefore it is useful to follow the intensity changes and peak shifts of the quadrupole resonance as a function of growth. With every two growth additions, an average intensity increase of 0.0711 was observed, and this intensity change is consistent throughout the additions. These

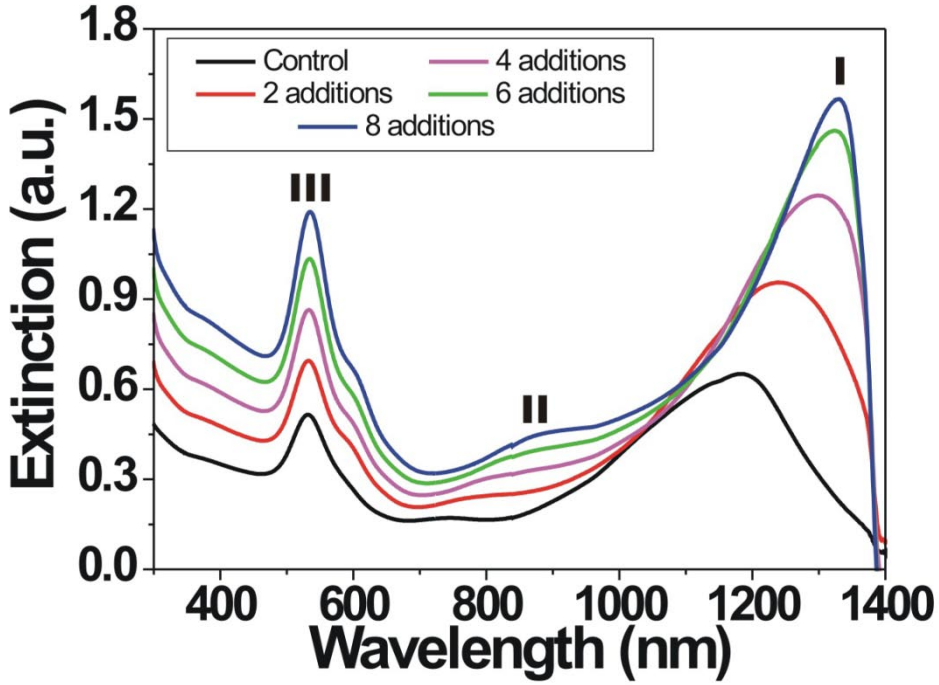


**Figure 3.1** UV-vis-NIR spectra of nanoprism solutions that have been grown to different edge lengths. Peaks **I** and **II** represent the dipole and quadrupole resonances of the gold nanoprisms, respectively. Peak **III** represents the dipole resonance of spherical nanoparticles.

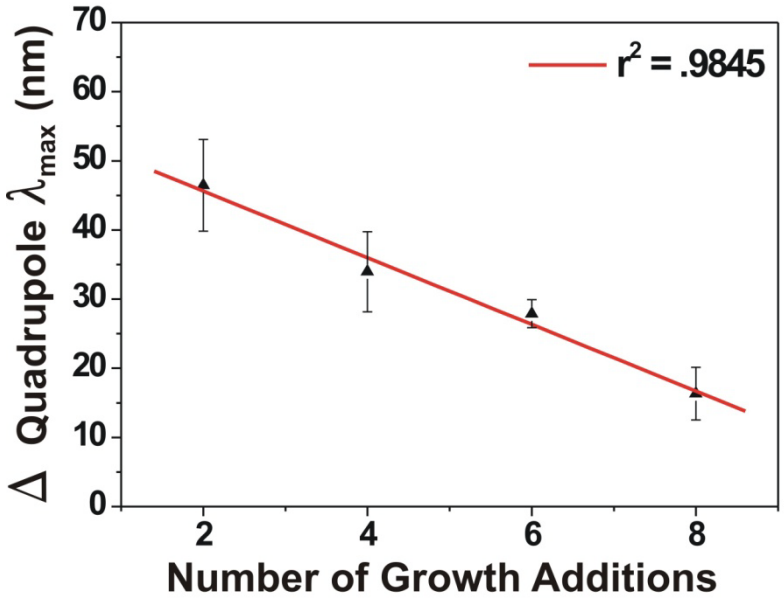


**Figure 3.2** The change in quadrupole plasmon resonance $\lambda_{max}$ between successive pairs of growth additions showing a strong, inverse linear relationship. Error bars represent 5 separate experiments.

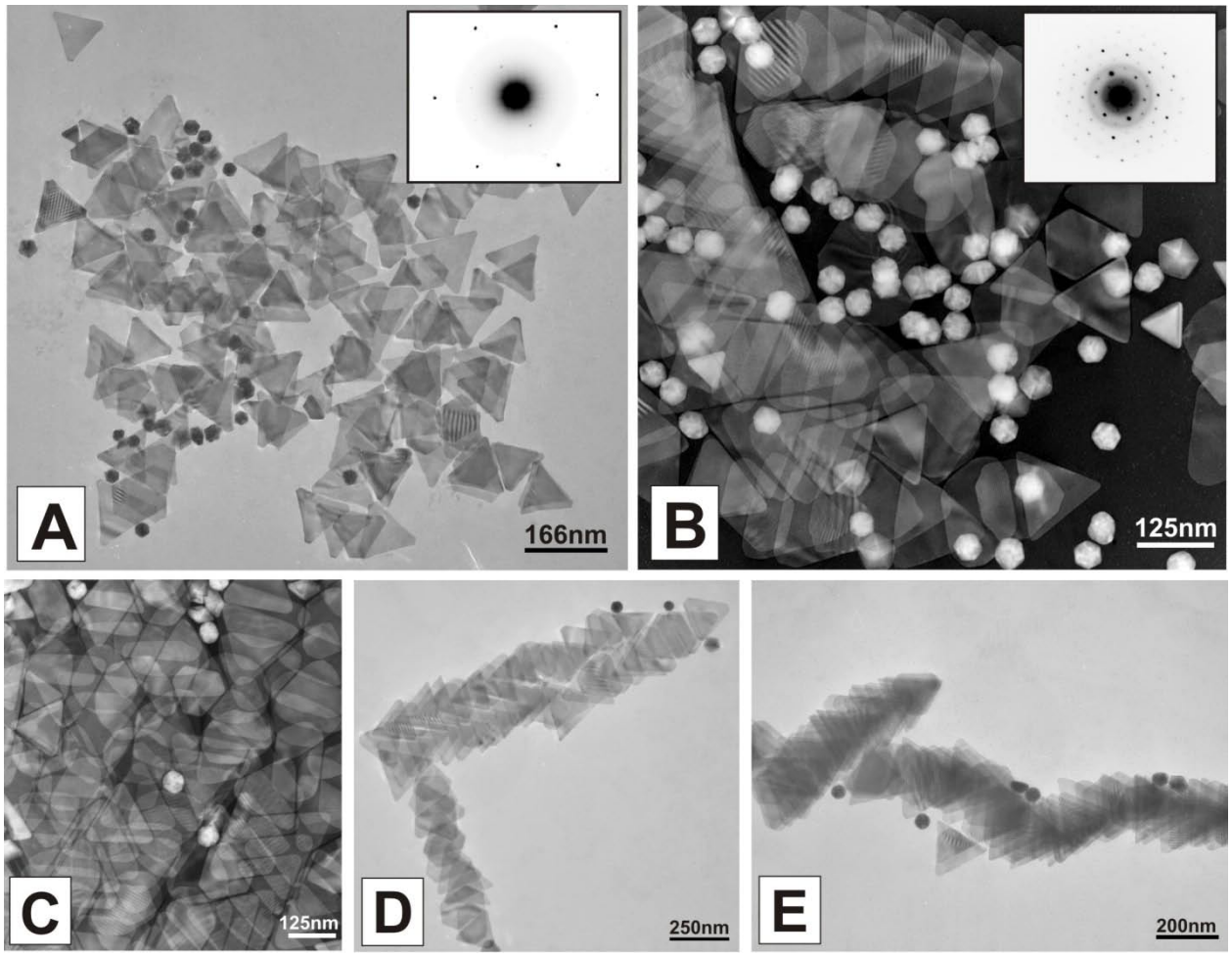


**Figure 3.3** TEM images of gold nanoprisms with increasing edge lengths (A) TEM image of gold nanoprisms made without additional growth (control sample). Inset shows diffraction pattern of the nanoprisms. (B) TEM image of nanoprisms after 2 growth additions (**x2**). Inset shows diffraction pattern of **x2** prisms. (C) TEM image of **x4** nanoprisms, (D) **x6** nanoprisms, and (E) **x8** nanoprisms.

redshifts indicate that the nanoprism edge length is growing, while the presence of the quadrupole shows that the triangular shape is being maintained (*vide infra*).[110] By plotting the magnitude of the quadrupole resonance shift per pair of growth additions, it seems that the degree of plasmon resonance shift decreases as the prism edge length increases (Figure 3.2). This change can be explained by considering that for each growth addition the same amount of gold ions and reducing agent are being added to the reaction, but the starting size of the prisms is becoming progressively larger. Therefore, there is a decrease in the degree of edge length growth that is possible per growth addition, because more gold is needed to produce a net edge length increase for an initially larger prism.

It should be noted that although the nanoprism plasmon resonances change in both position and intensity, the plasmon resonance of the nanoparticles only changes in intensity. This difference indicates that the diameter of existing pseudo-spherical nanoparticles is not significantly increasing, but rather that new particles are growing to approximately the same size and stopping (new nucleation events)—accounting for the change in intensity but not in peak position. The optical signature of the nanoprism colloid on the other hand, shows noticeable peak shifts along with changes in intensity. The observed intensity increases correlate with those expected from an increasing nanoprism extinction coefficient as the nanoprism size increases.[110]

### 3.3.2 Microscopy Analysis of Expanded Au Nanoprisms

Using TEM studies and statistical analysis, it has been observed that these plasmon resonance shifts discuss in Section 3.3.1 are indicative of a gradual increase in nanoprism edge length with little change in nanoprism thickness and crystallinity (Figure 3.3). The average edge length and thickness of initial nanoprisms are 114 nm ± 13.2% and 7.5 nm ± 6.7%, respectively (Figure 3A). A diffraction pattern of the original nanoprisms shows a hexagonal pattern that is

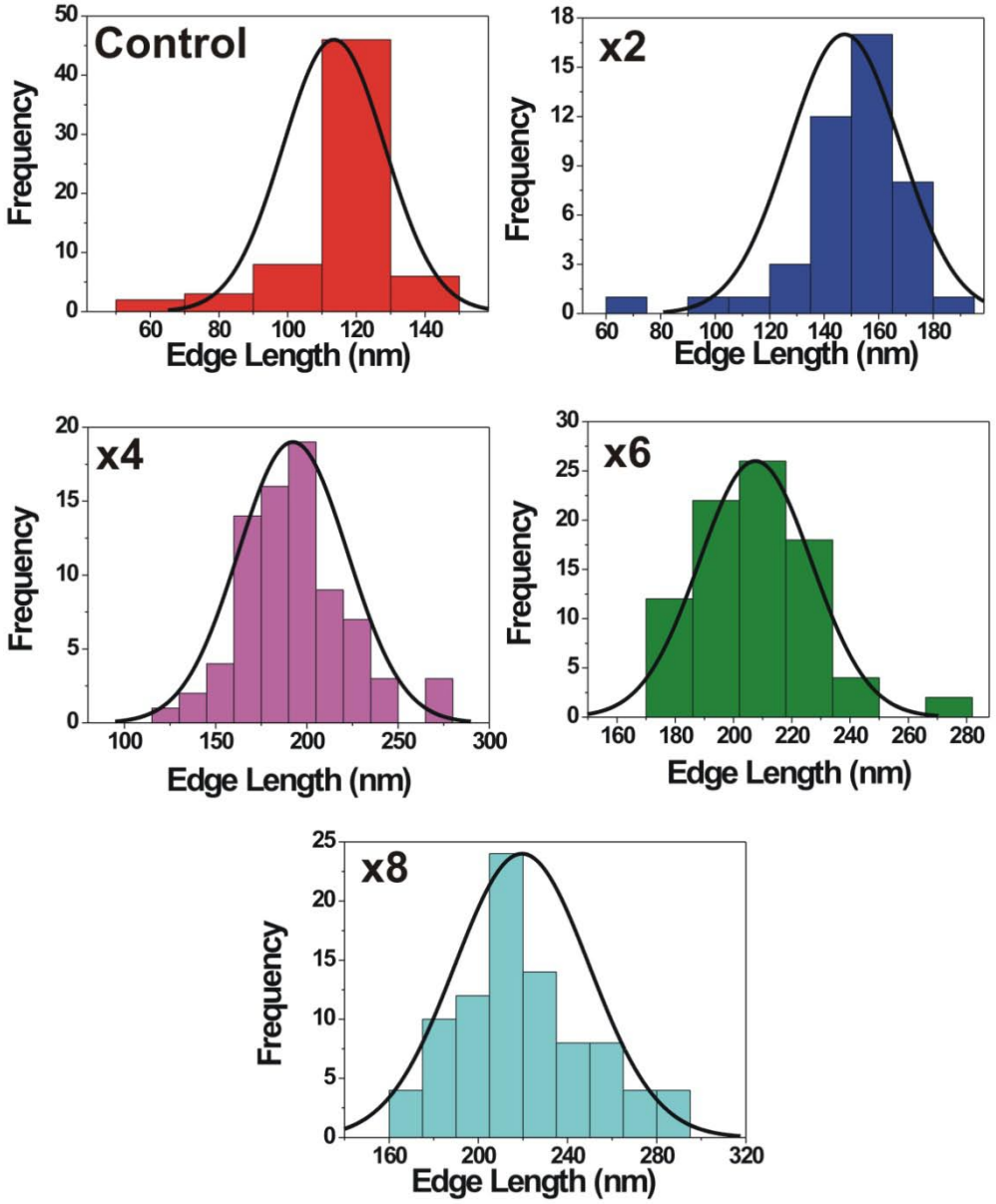


**Figure 3.4.** Histograms representing the size distribution of nanoprisms grown to different average edge lengths.

characteristic of the {111} facet of an fcc packed crystal (Figure 3.3A, inset). After the first series of growth additions (**x2**) it seems that the nanoprism shape is retained through the growing process, including edge smoothness and corner sharpness (Figure 3.3B). A diffraction pattern of a single, **x2** nanoprism also exhibits a distinct hexagonal pattern indicating a single crystalline {111} surface (Figure 3.3B, inset). This result demonstrates that the crystallinity of the nanoprisms is not significantly changed with increasing growth additions. Images of gold nanoprisms after **x4**, **x6**, and **x8** additions show similar results (Figure 3.3C, D, and E). The average nanoprism edge lengths for **x2**, **x4**, **x6**, and **x8** are 148 nm ± 13.5%, 192 nm ± 15.6%, 207 nm ± 9.2%, and 220 nm ± 13.6%, respectively (Figure 3.4). Throughout the growth additions, the average size distribution for nanoprism edge length is approximately 13%. This represents tight control over the rate and degree of gold nanoprism edge length growth. A uniform, gradual increase in average edge length is in agreement with the observed plasmon resonance shifts as well as the shifts predicted by theory (Figure 3.5).[110] Additional TEM analysis of the samples indicates that the nanoprism thickness is approximately the same throughout the additions (8 – 10 nm) and that the top and bottom faces of the nanoprisms are atomically flat as would be expected from a single crystal of gold (Figure 3.6). Electron energy loss spectroscopy (EELS) thickness analysis shows that the addition of gold to the prism side is occurring in the plane of the existing nanoprism, and that no ridges or surface roughness is created during the growth process (Figure 3.6A).

### 3.3.3 Crystallographic Characterization of Expanded Nanoprisms and Proposed Growth Mechanism

Interestingly, although there is a slight increase in prism thickness over the course of the growth additions, the nanoprism aspect ratio (aspect $\text{ratio}_{\text{nanoprism}}$ = edge length/thickness)

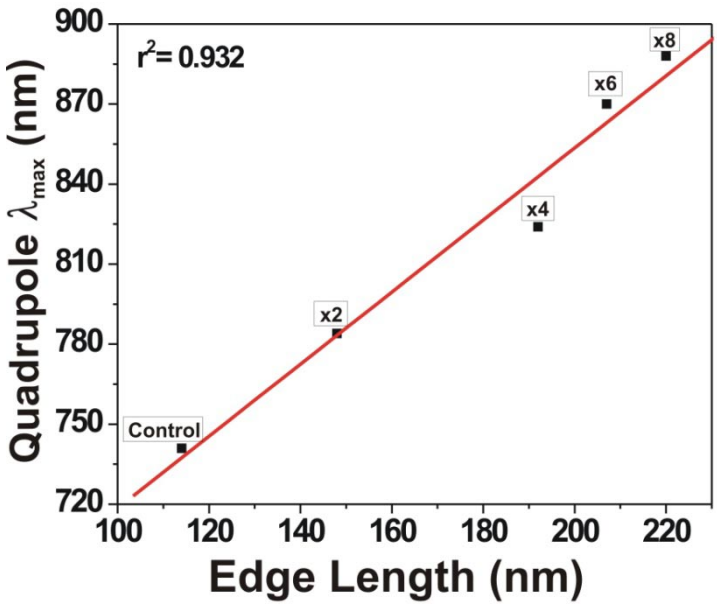


**Figure 3.5**. Plot of quadrupole plasmon resonance λmax vs. average nanoprism edge length of the corresponding nanoprisms. The linear regression analysis shows a strong, positive correlation between the two.

increases significantly from a range of 14 – 16 to a range of 22 – 27. This emphasizes the highly preferential growth of the nanoprism side facets over the triangular faces.

This degree of size control demonstrates the principles of seeding methodology.[52, 77] The concept of seeding involves the slow reduction of metal ions onto the surface of a growing nanoparticle, and at the same time, balancing the reducing power in the solution so that new nucleation events are slow relative to nanoparticle growth. Because Au ions have a high reduction potential in the absence of bulk metal ($Au_{atom}/Au^{I}$ (aq.) = -1.5V vs. NHE),[196] the Au nanostructures serve as catalysts that then facilitate Au ion reduction ($Au_{metal}/Au^{I}$ = 1.692 vs. NHE).[197] Interestingly, for a given number of additions, if equivalent amounts of gold and reducing agent are not added sequentially (as described previously), but instead are added as a single addition at the outset of synthesis, an equivalent increase in nanoprism edge length is not observed. The discrepancy indicates that the amount of gold ions in solution do not directly control the size of the resulting nanostructure. Instead, one sees an increase in the population of pseudo-spherical gold nanoparticles with little increase in nanoprism edge length. Therefore, a given amount of gold ions must be added step-by-step, otherwise the rate of pseudo-spherical particle growth can compete effectively with prism growth

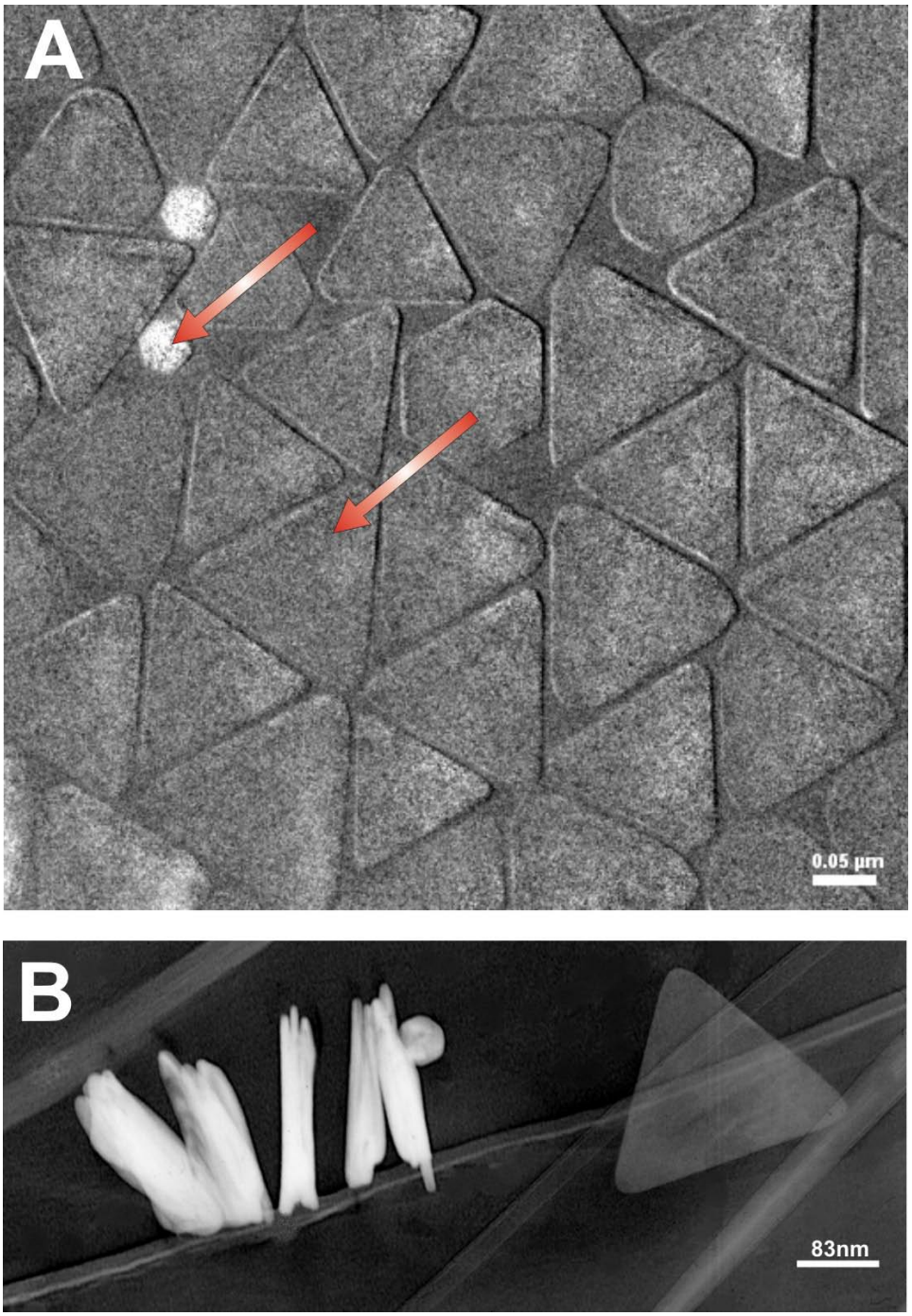


**Figure 3.6** (A) HRTEM image of **x4** nanoprisms using EELS where contrast uniformity indicates thickness uniformity. Arrows highlight the contrast between faceted and flat particles. (B) TEM image of **x4** nanoprisms turned sideways showing prism thickness. (lines across (B) are from the Formvar coating of the Cu grid used for immobilization of nanoprism sample).

(Scheme 3.1). Also, if gold ions are added in the absence of additional ascorbic acid, nanoprism edge length does not increase. From these results, one can conclude that slow addition of metal ions in the presence of a weak reducing agent is effecting prism growth.

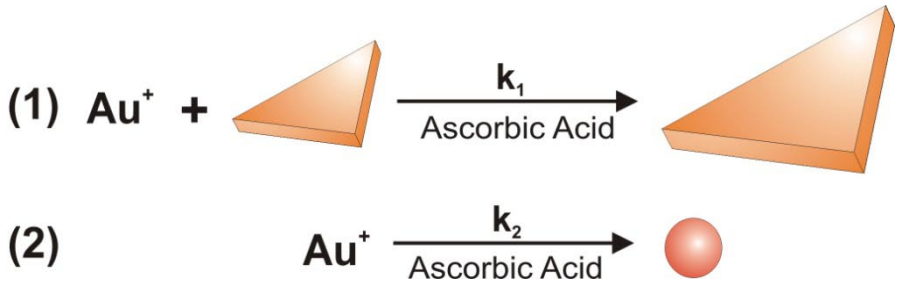


**Scheme 3.1** The two equations represent the competing reactions during the particle growth process. When given amounts of Au ions and reducing agent are added stepwise, $rate_2 < rate_1$. However, when the same amount is added "all-in-one", $rate_2 > rate_1$.

During the process of prism growth we observe an increase in the dipole resonance of pseudo-spherical nanoparticles along with the growth of the nanoprisms. The pseudo-spherical nanoparticles are primarily polyhedral (Figure 3.7) and are approximately 40 nm (± 8%) in diameter. TEM evidence shows that the nanoparticle size distribution in solution does not change significantly throughout the additions, and we do not see evidence of a population of small nanoprisms developing.[84] This competitive relationship may be understood, in part, based upon the Gibbs-Thomson effect. Consistent with the Gibbs-Thomson effect, a convex surface has a higher surface energy than a flat surface of the same material in the same phase. Conversely, a concave surface has

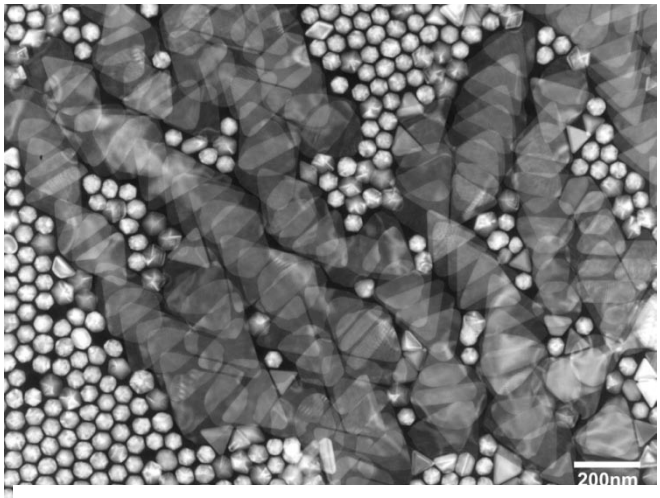


**Figure 3.7**. TEM image illustrating the primarily polyhedral geometry of the pseudo-spherical nanoparticles.

lower surface energy than a flat surface of the same material in the same phase. This effect has been observed for nanoscale metal islands, and may be one of the driving forces in anisotropic nanoparticle growth.[198] Recently, groups have suggested that nanoprisms are twinned {111} crystals, and that this twinning produces convex and concave side crystal facets.[103] The convex surface, according to a Gibbs-Thomson-like effect, would be less stable for the addition of new atoms, and could then explain the preferential growth of gold nanoprisms over the convex facets of the pseudo-spherical nanoparticles (Scheme 3.2). The diffraction patterns obtained from the nanoprisms indicate a single crystalline {111} top surface and a {112} side crystal facet (Figure 3.8). Also, we see forbidden reflections in the diffraction pattern which are consistent with the presence of a twinned structure, although they are not definitive. These crystal growth theories create a starting point for elucidating physical phenomena that are directing the selective growth of the nanoprism edge length. In addition to the physical considerations of surface energies, there are also chemical factors which mediate the growth of the nanoprism edge length by controlling the rate of gold ion reduction as was discussed earlier. It is most likely a combination of these driving forces that produce the preferential growth of the gold nanoprism edge length.

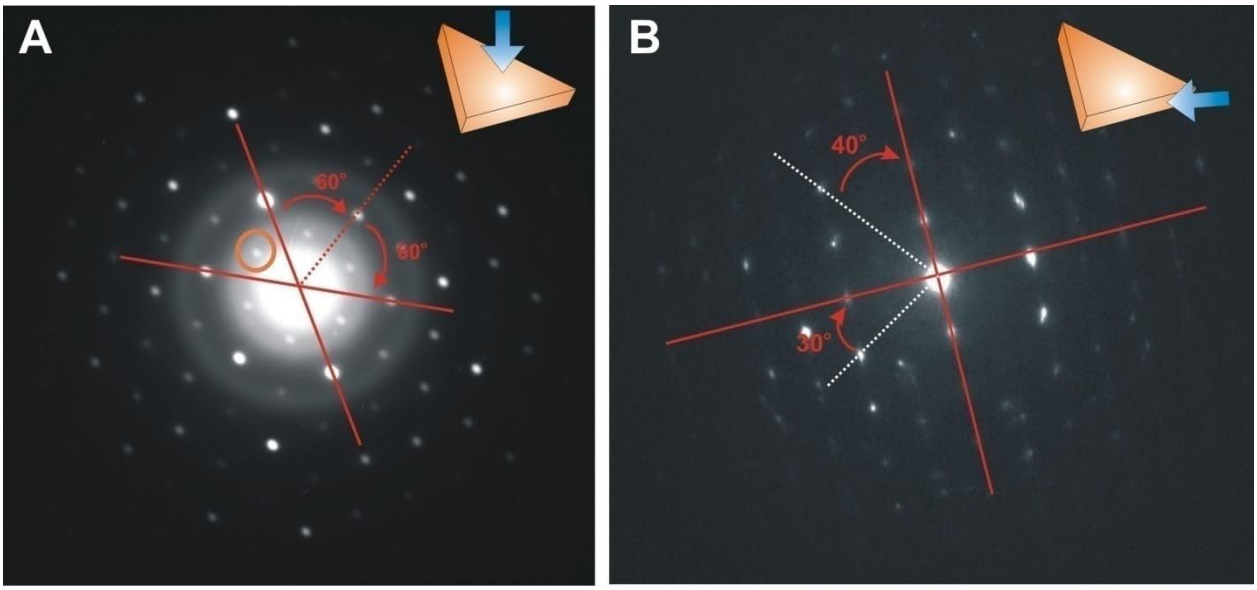


**Figure 3.8.** Diffraction patterns of nanoprism faces. (A) Hexagonal pattern indicates the [111] crystal surface. The orange circle highlights the presence of forbidden reflections. (B) Rectangular pattern is consistent with the {112} crystal surface of an fcc structure.

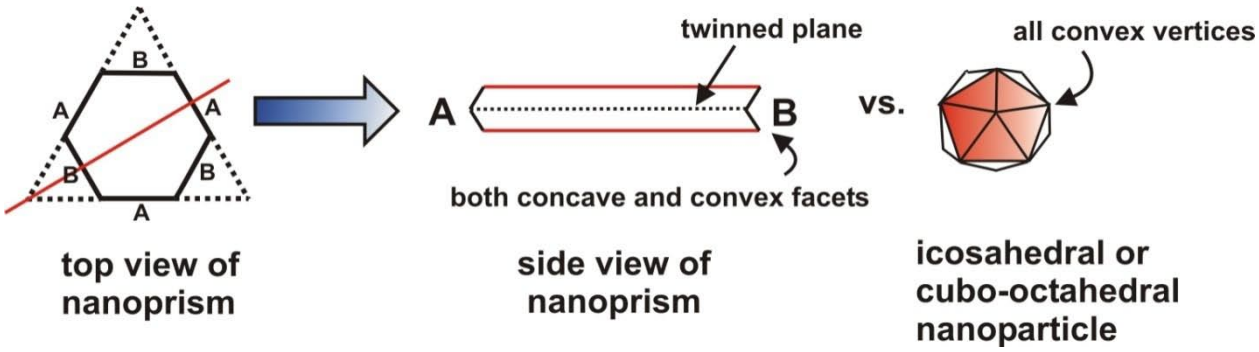


**Scheme 3.2.** Illustration of a twinned fcc nanocrystal, and the possible mechanism for platelike growth from such a structure. A polyhedral nanoparticle is shown for comparison.

In addition to these initial driving forces, we also have considered the age of the nanoprisms in evaluating the growth of the prism edge length, because it has been shown that the reactivity of Au nanoparticles can be highly dependent on nanoparticle age, at certain size

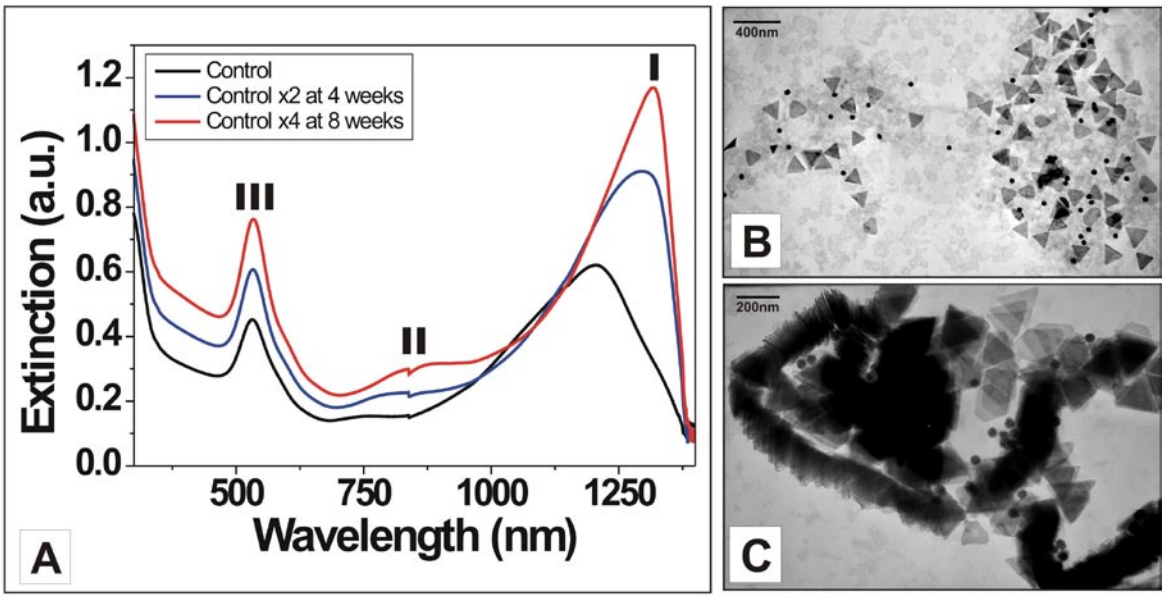


**Figure 3.9.** (A) UV-vis-NIR spectra of nanoprism solutions regrown at 4 and 8 weeks after their initial synthesis. Peak **I** and Peak **II** are the dipole and quadrupole plasmon resonances of gold nanoprisms, respectively. Peak **III** is the dipole resonance of spherical nanoparticles. (the small spike at 840nm is due to the grating changeover of the spectrophotometer when moving into the visible light range) (B) TEM images of nanoprisms grown at 4 weeks and (C) 8 weeks.

ranges.[199] It has been postulated that this dependence results from a reorganization of the nanoparticle surface as a means of reducing high energy defect sites that may have developed during synthesis. Using the growth method described herein, we have found that there is little effect on the growth process of nanoprisms as a function of aging time. For example, we have studied our growth method using nanoprisms that are 4 and 8 weeks old (Figure 3.9). The optical spectra of nanoprism growth show that the edge length increases are dependent only on the amount of gold ions and reducing agent added, and not the age of the nanoprism solution. Compared to nanoprisms grown from “fresh” colloids, older nanoprism solutions show similar intensity increases as the nanoprisms grow (average = 0.0766) and similar red-shifts of the quadrupole and dipole plasmon resonances (31 ± 13 nm for quadrupole) per two additions.

### 3.4 Conclusion

In summary, this chapter reports the development of a method for controlling the edge length of Au nanoprisms while preserving their original shape, crystal properties, and thickness. Importantly, edge length control is a way of tailoring the optical properties of these structures. This work also shows that the prisms can be used as seeds, and one can reinitiate particle growth simply by exposing them to Au ions in the presence of reducing agent in a step by step manner. These results indicate that certain nanoparticle surfaces may be more reactive than had previously been considered. Therefore, these findings have important implications for the synthesis of such structures and their use in a variety of applications, especially catalysis. Most significantly, we expect that many new shapes and sizes of nanoparticles will emerge as post-synthetic, seeding methodologies are integrated into other nanoparticle syntheses.

# CHAPTER FOUR

DNA-Gold Nanoprism Conjugates

Portions of this chapter have been accepted for publication in: *Small*, **2008.**

## 4.1 Introduction

Over the past two decades, there has been an enormous effort to understand, control, and use the relationship between the morphology of nanomaterials and their physical and chemical properties.[34, 200] Indeed, a great deal of effort has focused on controlling the size, shape, and composition of nanostructures. However, equally important is the surface chemistry of such structures, especially when one considers that the ratio of surface to bulk atoms is much higher than in micro or macroscopic systems. For example, the surface plasmon resonances (SPR) of nanoparticles are highly dependent upon the dielectric medium that surrounds them, including adlayers of molecules and solvent.[36, 105] Catalytic activity of a nanoparticle is also highly dependent upon adsorbate.[201, 202] Indeed, the development of ways to control the structure and chemical functionalization of a nanoparticle surface is a major area of research, and has led to the discovery of new properties and applications for this important class of materials.[203] In the case of isotropic metal nanoparticles, functionalization has led to a variety of exciting scientific insights and applications, including the use of nanoparticles for spectroscopic labels,[8]gene regulation agents,[25] and ultra-sensitive biodiagnostic tools.[13] In general, less has been done with anisotropic structures, but there have been some important observations and advances made for nanorod and nanoshell structures.[27, 28, 204, 205] For example, Murphy and coworkers have reported that gold nanorods functionalized with biotin-disulfide will assemble in an end-to-end manner when interconnecting streptavidin proteins are added to a colloid containing them. The authors concluded that such assembly behavior was indicative of end-selective functionalization.[205] Mann and coworkers described a similar example with oligonucleotide modified nanorods, but in contrast with the Murphy system, they observe sheet-like assembly of

nanorods along their long axes.[204] These results present a challenge to both understand and establish control over the face-selective functionalization of anisotropic nanoparticles.

An ideal system to address this challenge is an anisotropic nanoparticle that can be made in high yield, is composed of a metal with well known surface chemistry, exhibits strong, architecture- and environment-sensitive optical features, and has well-defined crystallographic facets. Recently, we and others have developed methods for synthesizing triangular prisms, made of gold or silver, that exhibit these characteristics.[45, 81, 84, 134] Nanoprisms of this type are generally single crystals, in some cases twinned, with broad, atomically flat triangular {111} faces, and high energy side crystal facets. Because of their well defined structures, these prisms are an excellent model system to study processes that involve the face selective functionalization of nanoparticles. Herein, we present a study aimed at determining the factors that allow one to adsorb alkylthiol-modified oligonucleotides on different facets of an anisotropic gold nanoparticle. To accomplish this goal, face-selective DNA ligand adsorption processes have been studied quantitatively and used to control the selective immobilization of DNA on the edges of the particle, which is confirmed by direct chemical analysis (using electron energy loss spectroscopy mapping) and indirectly by subsequent DNA-induced assembly events.

## 4.2 Experimental

### 4.2.1 Preparation of Au Nanoprisms

Nanoprisms were prepared according to a modified literature procedure.[104] In a typical experiment, all glassware was washed with aqua regia (3:1 ratio by volume of HCl and $HNO_3$), and rinsed copiously with NANOpure (18.1 MΩ) water. Au nanoparticle seeds were prepared by reducing 1 mL of 10 mM $HAuCl_4$ with 1 mL of 100 mM $NaBH_4$ while stirring vigorously. The reduction was done in the presence of 1 mL of 10 mM sodium citrate and 36 mL of fresh,

NANOpure water. Upon addition of the $NaBH_4$, the solution turned a reddish-orange color and was allowed to continue stirring for one minute. The resulting mixture was aged for 2 - 6 hours in order to allow the hydrolysis of unreacted $NaBH_4$. The gold nanoparticle seeds exhibited a plasmon resonance peak at 500 nm, and had an average diameter of 5.2 ± 0.6 nm. After the aging period, three growth solutions were prepared for the seed-mediated growth step. The first two solutions (**1** and **2**) contained 0.25 mL of 10 mM $HAuCl_4$, 0.05 mL of 100 mM NaOH, 0.05 mL of 100 mM ascorbic acid, and 9 mL of the prepared CTAB solution. The final growth solution (designated **3**), contained 2.5 mL of 10 mM $HAuCl_4$, 0.50 mL of 100 mM NaOH, 0.50 mL of 100 mM ascorbic acid, and 90 mL of the prepared CTAB solution. Nanoprism formation was initiated by adding 1 mL of seed solution to growth solution **1**. The solution was gently shaken, and after two seconds, 1 mL of growth solution **1** was immediately added to **2**, **2** was shaken and after two seconds, all of the resulting growth solution was added to **3**. After this addition, the color of **3** changed from clear to deep magenta-purple over a period of 30 minutes. Nanoprisms were purified by separating aliquots of the reaction mixture into 1.5 mL centrifuge tubes in 1.5 mL aliquots, and allowing the prisms to precipitate overnight. After separation, the supernatant was removed, and the nanoprism pellet was resuspended in NANOpure water.

### 4.2.2 Preparation of Functionalization Buffers

All buffers were prepared using nuclease-free water and molecular biology grade chemicals obtained from Sigma-Aldrich, Inc. To adjust salt conditions in the DNA-nanoprism solutions, a variety of buffer solutions were prepared: a phosphate adjustment buffer (0.1 M, pH 7.0, 0.562 g $Na_2HPO_4$, 0.125 g $NaH_2PO_4$, 50 mL water), a surfactant stock solution (0.1% SDS (w/v), .01 g SDS, 10 mL water), a salting buffer **(**2 M NaCl (pH 7.0): 5.844 g NaCl, 50 mL water), a disulfide cleavage buffer **(**0.17 M phosphate buffer (pH = 8.0), 1.147 g $Na_2HPO_4$,

0.0509 g $NaH_2PO_4$, 50 mL water), a washing buffer **(**0.01 M phosphate buffer + 0.01% SDS (pH 7.0): 0.562 g $Na_2HPO_4$, 0.125 g $NaH_2PO_4$, .05 g SDS, 500 mL water), and a hybridization/melting buffer (0.01 M phosphate buffer + 0.015 M NaCl (pH = 7.4): 0.562 g $Na_2HPO_4$, 0.125 g $NaH_2PO_4$, 8.766 g NaCl, 500 mL water).

### 4.2.3 Functionalization of Au Nanoprisms

Prior to the functionalization of Au nanoprisms, the alkylthiol-functionalized DNA sequences (HS-ssDNA, Sequence A: $^{5'}$ACT ATT GAT AAG GAT A10 SH$^{3'}$; Sequence B: $^{5'}$ATC CTT ATC AAT AGT A10 SH$^{3'}$) were reduced by treating the oligonucleotides with 0.1 M dithiothreitol (DTT) in phosphate buffer (0.17 M, pH 8) for 1 h (typically, 4 µL of DTT solution for every 1 $OD_{260}$ of DNA). The HS-ssDNA solution was purified from DTT using a desalting column (Nap-5, DNA grade, GE Healthcare). Nanoprisms were functionalized by using modifications of literature procedures.[206] Briefly, 1.2 $OD_{260}$ of purified HS-ssDNA is added to 1.0 $OD_{1250}$ of Au nanoprisms and allowed to react while shaking (1100 rpm, 22°C) for 30 min. The solution is then brought to physiological conditions (0.15 M NaCl, 0.01 M phosphates) in the presence of surfactant (0.01% sodium dodecyl sulfate) over a period of 2.5 h. Phosphate, surfactant, and NaCl concentrations were adjusted using stock solutions made from nuclease-free water and reagents (*vide supra*) where the phosphate and surfactant concentrations were adjusted first, and the total necessary volume of stock NaCl solution was divided into 3 aliquots, and each aliquot was added to the solution sequentially with 30 minutes between each addition. After the last salt addition, the solution was allowed to mix for an additional 30 minutes, at which point DNA adsorption to the nanoprism surface was monitored and marked as $t_0$.

### 4.2.4 UV-vis-NIR Spectrophotometry and TEM Analysis

The optical features and melting behavior of Au nanoprisms were monitored by absorbance spectroscopy (UV-vis-NIR) using a Varian Cary 5000 spectrophotometer, in double-beam mode, baselined to the spectrum of NANOpure water. Absorbance cuvettes were 10mm pathlength, single crystalline quartz (QS, 284, Hellma, Inc.), and contained either 1.5 mL sample chambers, or 2 mL sample chambers with stirring area (for hybridization and melting experiments). All nanostructures were characterized using a Hitachi-8100 transmission electron microscope (TEM) at 200kV.

### 4.2.5 Hybridization and Melting Experiments

To prepare DNA-nanoprism conjugates for hybridization and melting experiments, the conjugates were first washed in order to remove excess, unbound DNA from solution. To wash, the mixture was centrifuged for 3 minutes at 8,000 RPM (using an Eppendorf 5145D rotor), the supernatant removed, and the pellet resuspended in washing buffer. This process was repeated 3 times, and after the supernatant had been removed a third time, the pellet was resuspended in hybridization/melting buffer, and combined with a DNA-nanoprism conjugate that contained a complementary DNA strand, which was prepared using the same washing procedure. DNA-nanoprism conjugates were hybridized using a 1:1 ratio of complementary-DNA functionalized nanoprisms as measured by $OD_{1250}$ (the optical density at the $\lambda_{max}$ of the Au nanoprism dipole plasmon resonance). If monitored by UV-vis-NIR, the hybridization procedure involved heating the mixture to 75°C and cooling to 25°C at a rate of 0.25°C/min using the Cary 5000 Peltier temperature control system, while stirring. To melt, the solution was heated from 25°C to 75°C at a rate of 0.25°C/min again using the Peltier system. Two complementary DNA-functionalized

nanoprisms could also be hybridized by mixing the two in a 1.5 mL centrifuge tube, and being allowed to stand, protected from light, at room temperature overnight.

### 4.2.6 Determining DNA loading on Au Nanoprism

To determine the number of oligonucleotides conjugated to the nanoprism surface, a two step method was used wherein the number of DNA strands were measured using a commercially available ssDNA quantification assay, and the Au nanoprism concentration was determined using inductively-coupled plasma mass spectrometry (ICP-MS). First, DNA-nanoprism conjugates were prepared and washed to remove excess and loosely bound DNA from solution. To wash the nanoprisms, the solution was centrifuged at 8,000 rpm for 3 minutes (Eppendorf 5145D centrifuge) and the supernatant was removed. The pellet was resuspended in washing buffer, and this washing procedure was repeated 4 additional times. After the supernatant was removed a fifth time, the pellet was resuspended in 20 µL of 0.1 M aqueous solution of KCN and allowed to sit on the benchtop for 1 h. This process dissolves the Au nanoprism, but does not degrade the ssDNA. The resulting solution was then analyzed using the Quant-It ssDNA Assay with Oligreen® fluorophore (Invitrogen, Inc.) to determine the total number of DNA strands in solution, following the manufacturer protocol. Fluorescence was analyzed using a fluorescent plate reader (Photal Otsuka Electronics FluoDia T70, with excitation at 480 nm and emission at 520 nm).

Following this procedure, a 50 µL aliquot of the Oligreen-analyzed sample was prepared for analysis by ICP-MS to determine the number of Au atoms. Briefly, an Au standard curve was prepared with values 1, 2, 5, 10, 25, 50, and 100 ppb Au in a matrix of 3% $HNO_3$ (TraceUltra, Sigma Aldrich) and 1 ppb In, as an internal standard. This matrix was also used to prepare the unknown Au samples. The number of gold atoms obtained by ICP-MS were converted into

number of nanoprisms by using the relative frequency of nanoprism edge lengths (determined from a statistical analysis of nanoprism edge length as determined by TEM), the unit cell values

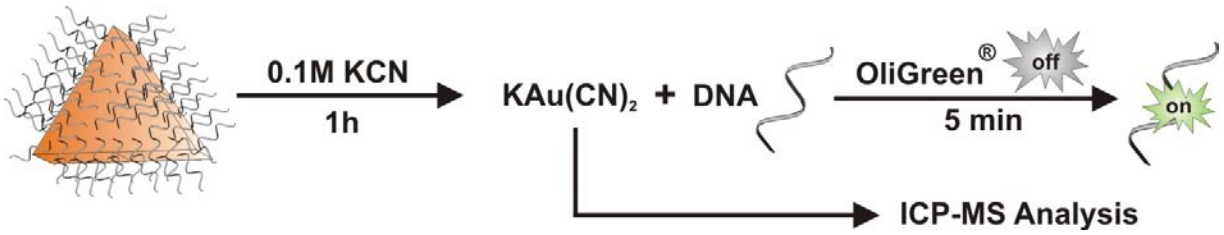


**Scheme 4.1** Process of determining oligonucleotide loading on Au nanoprisms.

of Au ($a$ = 0.4080 nm, 4 atoms per cell, $V_{unit\ cell}$ = 0.0679 $nm^3$) and the geometry of the nanoprism. This method allowed a more accurate determination of nanoprism concentration in solution which was critical to obtaining reproducible DNA loading values. With the concentration of nanoprisms and oligonucleotides in hand, the number of oligonucletoudes per nanoprism was calculated.

## 4.3 Results and Discussion

### 4.3.1 Hybridization and Melting Behavior of DNA-Nanoprism Conjugates

In this experiment, two separate batches of nanoprisms were functionalized with ssDNA sequences that were complementary. The two solutions of DNA-modified nanoprisms were then combined, and characterized by UV-vis-NIR spectroscopy (Figure 4.1A).[42] Dehybridization of the assembled DNA-Au nanoprism conjugates occurred over a very narrow temperature range, exhibiting a melting temperature, $T_m$, of 60.1°C (determined by taking the first-derivative of the melting curve and measuring the full width of the peak at half its maximum, FWHM = 2.4°C, Figure 4.1A insert). This sharp melting behavior has been observed previously for pseudo-spherical nanoparticles functionalized with DNA[42, 206] and is a diagnostic feature of particles that are densely functionalized with DNA. The melting of the Au nanoprisms was monitored at

1250 nm, which corresponds to the dipole surface plasmon resonance of Au nanoprisms and indicates that the melting transition is associated with the dehybridization of nanoprisms interconnected by DNA.

TEM images of nanoprisms that were taken after melting show that the nanoprism morphology is unaffected by either the functionalization or melting procedures (Figure 4.1B). These results are confirmed by UV-vis-NIR spectroscopy (Figure 4.1C) where hybridized gold nanoprisms (blue line) and the same nanoprism mixture after dehybridization by melting (black line), both exhibit the dipole (1250 nm) and quadrupole (800 nm) SPRs indicative of Au nanoprisms.[84] The observation that the nanoprism shape is maintained throughout these processes is significant, because surface reorganization at the high energy vertices and edges has been observed previously for structures containing high energy surface sites.[207, 208]

To further demonstrate not only the stability of the nanoprism structure, but also the robustness of DNA conjugation to the nanoprism surface, we investigated the reproducibility of hybridization and melting for the same batch of nanoprisms (Figure 4.1D). In this experiment, complementary ssDNA functionalized nanoprisms were mixed together at high temperature (75°C) and then slowly cooled (0.25°C/min) to 25°C in order to observe the hybridization transition of the conjugated DNA. Once hybridized, the mixture was heated back to 75°C (again at 0.25°C/min) in order to now observe the melting transition of the two conjugates. This cycle was then immediately repeated with the same batch of nanoprisms. The reproducibility of these transitions is a strong indication of the robustness of the DNA-modified nanoprisms, and is consistent with the covalent attachment of DNA to the nanoprism surface. This result was further confirmed by XPS, which showed the absence of bromine (usually present on as-made

nanoprisms), and the presence of phosphorous and sulfur indicating the replacement of CTAB ligands with thiolated ssDNA (Figure 4.2).

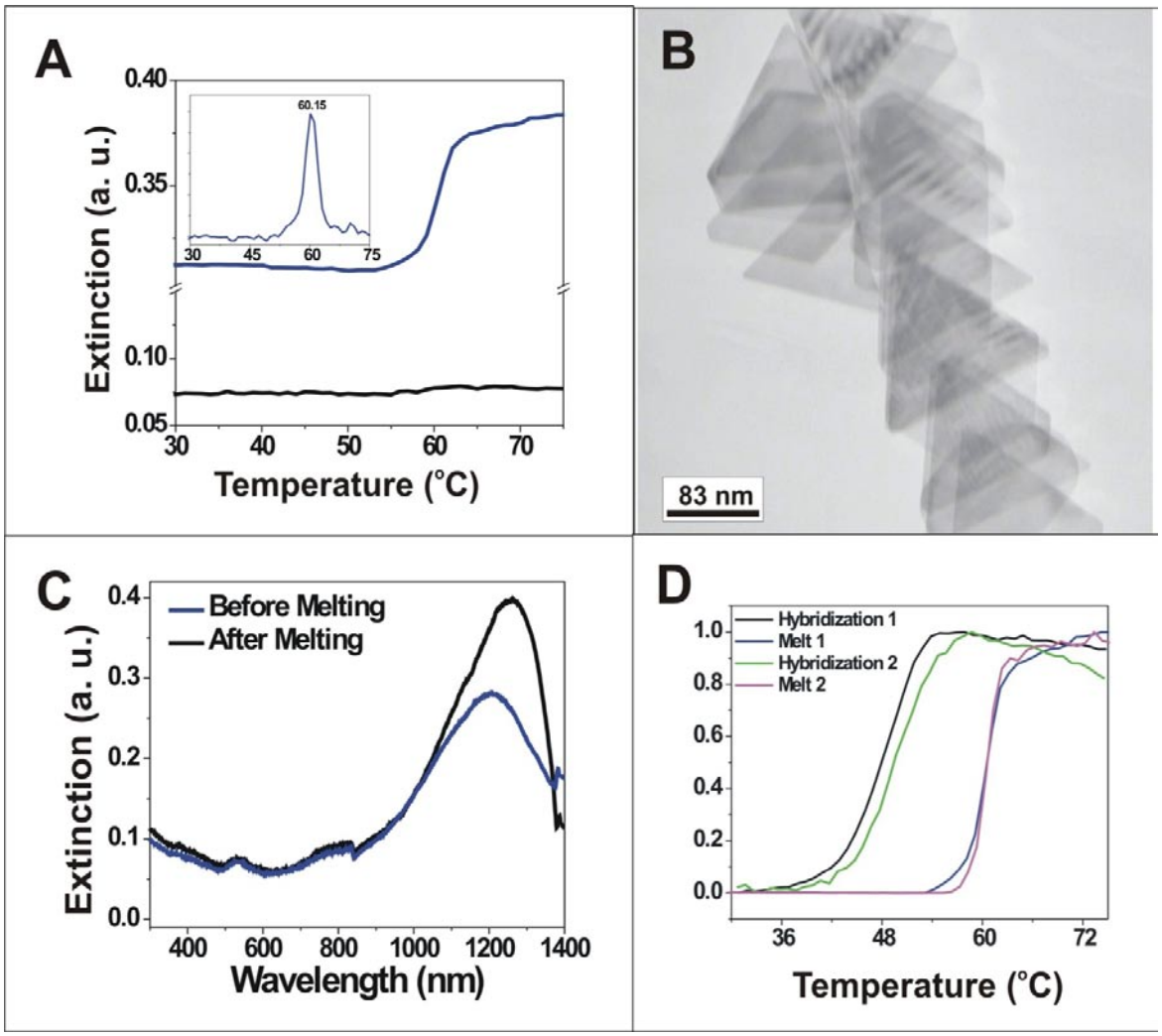


**Figure 4.1.** (A) Melting profile of Au nanoprism-DNA conjugates solution monitored at 1250 nm (dipole SPR of gold nanoprisms, blue) and 532 nm (dipole SPR of 40 nm gold nanoparticles, black). Inset: first derivative of melting transition at 1250nm; $T_m$ = 60.1 $^oC$; FWHM = 2.4$^oC$ (B) TEM image of nanoprism-DNA conjugates after melting. (C) UV-vis-NIR spectra of nanoprism conjugates. (D) Phase transitions of DNA-functionalized gold nanoprisms.

### 4.3.2 Quantification of DNA Loading on Nanoprism Surface

Having synthesized a DNA-conjugated nanoprism structure, the amount of DNA on the nanoprism surface was characterized in order to gain insight into the density of the DNA on the surface and therefore the efficiency of adsorption. If one uses simple geometry and assumes a flat surface on each of the nanoprism facets with a DNA-footprint of 17 $nm^2$, 21 approximately 1000 ssDNA molecules could adsorb per nanoprism, for a prism with 130 nm edge length and 7.5 nm thickness To confirm these loading values experimentally, we have developed a method that is complementary to our previous approach,[209] and which uses ICP-MS instead of extinction coefficient to determine Au nanoprism concentration because of the variation of particle extinction coefficients with particle size. [36] In a typical experiment, an aliquot of DNA-functionalized nanoprisms was centrifuged three times in 0.01% SDS solution to remove excess DNA (3 min at 8,000 rpm, Eppendorf 5145D Rotor). The supernatant was then removed and the pellet was resuspended in 20 μL of KCN (0.1M) for 1 hour in order to dissolve the Au and release the alkylthiolated DNA. An aliquot of this dissolved pellet was then analyzed by ICP-MS to determine gold atom concentration, and also analyzed by fluorescence using the Quant-it Oligreen™ ssDNA assay (Invitrogen, Inc) to determine ssDNA concentration. From these values the concentration of

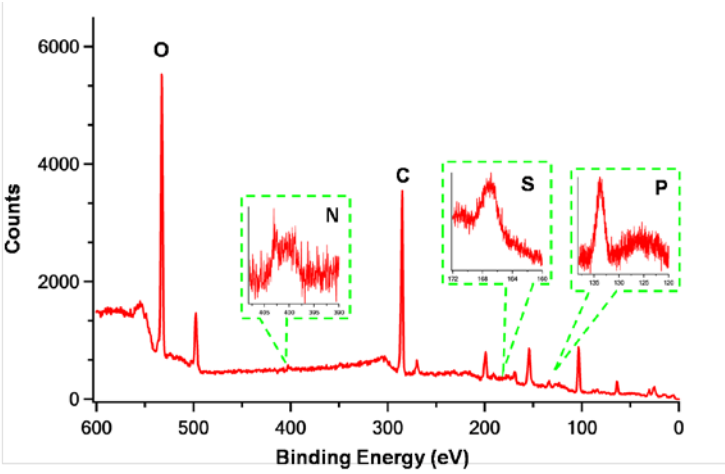


**Figure 4.2.** XPS spectrum of DNA-nanoprisms showing the presence of sulfur, phosphorous, and nitrogen on the nanoprism surface.

| Particle | Loading at 1 h Observed | Loading at 24 h Observed | Full Coverage Expected | Side-Only Coverage Expected |
|---|---|---|---|---|
| 130 nm Edge Length Nanoprisms | 484 ± 40.9 | 1550 ± 121 | 1894 | 172 |
| 150 nm Edge Length Nanoprisms | 643 ± 54.5 | 2030 ± 166 | 2491 | 199 |
| 80 nm Gold Nanoparticles | 762 ± 8.91 | 1330 ± 40.3 | 2000 | n/a |

**Table 4.1.** Compares theoretical and experimental values for DNA loading on Au nanoprisms and 80 nm Au nanoparticles. The calculations are based on 17 $nm^2$ footprint for the DNA molecule on the gold nanoprisms surface and a 15 $nm^2$ footprint for the 80 nm nanoparticles; these footprints account for the differences in surface curvature between the two structures.

DNA strands per nanoprism could be obtained (Table 4.1). Using this approach we determined that nanoprisms with 130 nm edge lengths typically contain approximately 1500 DNA strands per prism, and this is markedly larger than the predicted values based on a 17 $nm^2$ DNA footprint.[210] This larger loading value is most likely due to the fact that the theoretical calculation does not take into consideration the portion of the prism at the edge between the side and triangular facets, and the effective curvature at those sites. Additionally, the footprint of DNA is salt dependent, and may be influenced by the large effective salt concentration at the surface of the nanoprism.

### 4.3.3 Localization and Time-Dependence of DNA Adsorption

Interestingly, we have found that the prisms reach their maximum loading after 24 hours in excess ssDNA and buffer. However, data obtained earlier in the functionalization procedure, for example after only 1 hour in excess DNA/buffer, show markedly lower loading values (Table 4.1). Therefore, the timescale of ssDNA adsorption on the nanoprism surface was investigated and compared to the adsorption of ssDNA on CTAB-stabilized 80 nm Au nanoparticles (AuNPs) (Figure 4.3). Interestingly, ssDNA adsorption onto the nanoprism surface shows significantly

different kinetics than that of the pseudo-spherical AuNP controls. These data suggest that it takes over 12 hours to approach the theoretical ssDNA loading maximum for Au nanoprisms, whereas maximum loading is achieved on pseudo-spherical NPs after only 6 hours. We hypothesized that the slower kinetics may be a result of nanoparticle shape. The top, triangular face of the nanoprism is {111}, and the side facet is a high energy crystal facet that likely contains at least one twin plane.[104] We further hypothesized that the difference in surface energy of these two crystal faces may result in different ligand exchange kinetics, where ligand exchange would be faster at the higher energy side crystal facet.[211] This property could then result in site-selectively functionalized Au nanoprism structures.

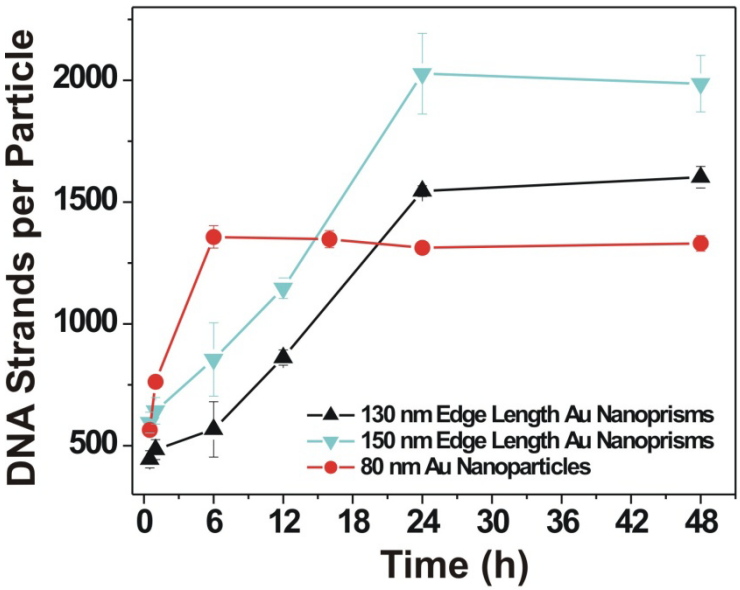


**Figure 4.3.** Correlation of time with DNA loading on nanoparticle surface. (Error bars indicate 5 independent experiments.)

To test this hypothesis, the location of DNA on the nanoprism surface was characterized at different functionalization time points. However, because nanoprisms are smaller than the wavelengths of visible light, optical microscopy-based techniques such as fluorescence could not provide the spatial resolution necessary to determine DNA location. We therefore first used transmission electron microscopy (TEM) and asymmetrically-functionalized AuNPs

(AsyNPs)[212] to investigate the location of DNA on the nanoprism surface. Here, the AsyNPs act as probes and indicators for ssDNA on the nanoprism surface (Figure 4.4A-C). These AsyNPs have been functionalized on one hemisphere with ssDNA that is complementary to DNA on the nanoprism surface. [212] Au nanoprisms are then isolated from buffered solutions of excess ssDNA, washed, and combined with the AsyNP probes at 4, 12, and 24 hours in the DNA mixture (Figure 4.4). At early functionalization time points, the probes bind only to the nanoprism side crystal facets, but as functionalization time increases the probes bind to more of the nanoprism surface, and finally after 24 hours the probes can be observed coating the entire nanoprism surface. These results were supported by electron energy loss spectroscopy (EELS) which allowed us to determine the presence of phosphorous (here phosphorous indicates the presence of DNA from the phosphodiester linkages of the DNA backbone) from both the center and sides of a single nanoprism structure. Results of this analysis indicate that, indeed, the side facets of the nanoprisms contain more DNA (as indicated by phosphorous EELS signal intensity) than the center of the nanoprism at short time points (Figure 4.4D).

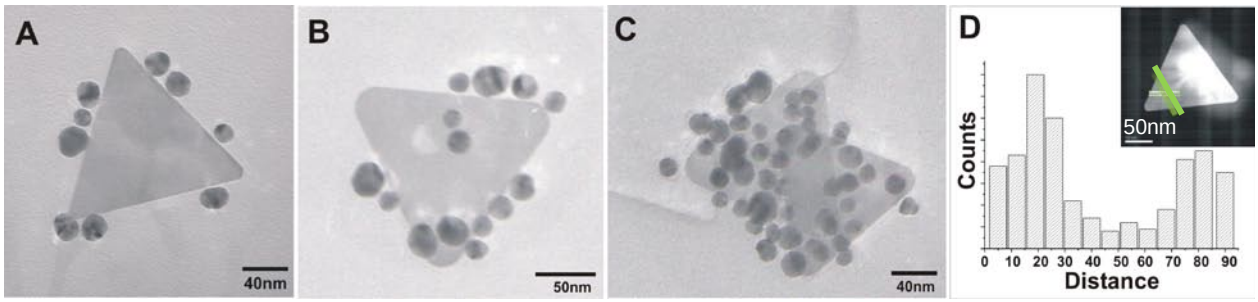


**Figure 4.4.** TEM images from experiments using asymmetrically functionalized AuNPs as surface functionalization probes. (A) Nanoprisms functionalized for 4 hours (B) 12 hours (C) 24 hours and then hybridized with AuNPs (13nm) that were asymmetrically functionalized with complementary ssDNA. (D) Phosphorous EELS analysis of Au nanoprism surface. The graph shows the signal of phosphorous as a function of distance. Inset is a STEM image of the nanoprism analyzed; the green line indicates the area at which each spectrum was taken.

The ligand functionalization pattern observed in these experiments seems to be one in which DNA adsorbs to the side facets of the nanoprism surface first, slowly functionalizes the outer top surface, and finally the entire prism. This model is consistent with ligand adsorption theories proposed by Murray, et al. who demonstrated that thiolated-ligand exchange on Au surfaces occurs fastest at crystal defect sites, and ligands adsorbed at these locations then migrate onto uniform crystal surfaces.[211] This theory is consistent with the observation that AuNP probes bind preferentially to the sides of the nanoprisms initially (where the concentration of edges and vertices is highest) and then slowly move from the edge to the center (Figure 4.4). The experiments with AsyNP probes also show that selectively functionalized prisms can be isolated at any time point. These site-selectively functionalized nanoprisms then represent powerful building blocks for nanoscale assemblies, with a type of valency that should allow for the use of multiple types of DNA links in a highly directional particle assembly scheme.

### 4.4 Conclusion

Taken together, these results represent three advances for anisotropic colloidal nanoparticles. First, Au nanoprisms capped by CTAB can be fully functionalized with an

alkylthiolated-DNA moiety, and the ligand-nanoprism conjugate is stable throughout DNA-based melting transitions. Second, DNA-functionalized anisotropic materials can exhibit cooperative melting behavior, similar to their isotropic counterparts. Finally, the inherent anisotropy of surface energetics in anisotropic colloidal particles can be exploited to achieve selective functionalization of the particle surface which has implications in fields ranging from materials design to catalysis and will be discussed in the following chapter.

# CHAPTER FIVE

Synthesis, Characterization, and Applications of DNA-functionalized Anisotropic Nanomaterials

Portions of this chapter have been published previously in: *Nano Lett.*, **2007**, *7*, 3818. and *Nano Lett.*, **2007**, *7*, 3849.

## 5.1 Introduction

The introduction and development of the oligonucleotide nanoparticle conjugates using isotropic nanoparticles has significant advances nanotechnology-based molecular diagnostics,[13] materials synthesis,[42, 213]and gene regulation.[25] Oligonucleotide conjugates using anisotropic nanoparticles are also promising materials and have found applications in cancer therapeutics,[27, 28, 65, 214] sensing,[72, 215] and encryption[72]. In addition to their many demonstrated applications, oligonucleotide-nanoparticle conjugates have undergone intense investigation in order to elucidate their fundamental properties. For example, oligonucleotide nanoparticles exhibit cooperative-DNA hybridization,[206] increased effect binding constants,[216] retain their oligonucleotide shell under cell culture conditions, are stable in physiological environments, resist nuclease degradation,[25] enter a variety of cell types without the use of auxiliary reagents, and are easily enhanced through chemical modification to increase efficacy.[26, 217]

On the other hand their anisotropic nanoparticle counterparts have received less attention. While anisotropic nanoparticle-DNA conjugates have been used in a variety of applications, there have not been parallel investigations of their fundamental properties or for methods to characterize them. In this chapter, a general method for synthesizing and characterizing anisotropic nanoparticle-DNA conjugates is presented, and several applications of these well-characterized structures are demonstrated including applications in encryption, detection, and gene regulation.

## 5.2 Experimental

### 5.2.1 Preparation of Functionalization Buffers

All buffers were prepared using nuclease-free water and molecular biology grade chemicals obtained from Sigma-Aldrich, Inc. To adjust salt conditions in the DNA-nanoprism solutions, a variety of buffer solutions were prepared: a phosphate adjustment buffer (0.1 M, pH 7.0, 0.562 g $Na_2HPO_4$, 0.125 g $NaH_2PO_4$, 50 mL water), a surfactant stock solution (0.1% SDS (w/v), .01 g SDS, 10 mL water), a salting buffer **(**2 M NaCl (pH 7.0): 5.844 g NaCl, 50 mL water), a disulfide cleavage buffer **(**0.17 M phosphate buffer (pH = 8.0), 1.147 g $Na_2HPO_4$, 0.0509 g $NaH_2PO_4$, 50 mL water), a washing buffer **(**0.01 M phosphate buffer + 0.01% SDS (pH 7.0): 0.562 g $Na_2HPO_4$, 0.125 g $NaH_2PO_4$, .05 g SDS, 500 mL water), and a hybridization/melting buffer (0.01 M phosphate buffer + 0.015 M NaCl (pH = 7.4): 0.562 g $Na_2HPO_4$, 0.125 g $NaH_2PO_4$, 8.766 g NaCl, 500 mL water).

### 5.2.2 Preparation of DNA-Conjugated Au Nanodisk Arrays

Nanodisk arrays were prepared using On-Wire Lithography (OWL)[218] and typically contained between six and ten disks each with 120 nm thickness and 360 nm diameter. A silica backing encapsulated one half of the nanostructure and immobilized the disks with their circular faces parallel to each other. After undergoing the OWL procedure, these structures were washed three times with $H_2O$, and three times with ethanol by centrifuging at 5k RPM for 5 min (using Eppendorf 5145D rotor). Prior to functionalization with DNA, the arrays were then washed an additional time in water in order to ensure that no array preparation reagents were carried over into the subsequent steps. Freshly prepared DNA (≈ 2 $OD_{260}$) was added to a 1 mL aqueous solution of OWL generated nanorods/arrays (one full template's yield ≈ 1fM dissolved in 1 mL nuclease free water) and allowed to mix for 30 min. Phosphate adjustment buffer and SDS

solution were added to this DNA-nanorod/array solution so that the final phosphate concentration was 0.01 M. and the final SDS was concentration to 0.01% (w/v) in solution. After 30 minutes, salting buffer was added in 1/5 increments separated by 30 min each to bring the final concentration of NaCl concentration to 0.30 M. The DNA-nanorod/array was allowed to mix for 2d in the dark on a Eppendorf Thermomixer® at 23°C, 800 RPM. These conjugates are stable in excess DNA, nucleas-free water, and at 4°C for over 1 month.

### 5.2.3 Hybridization Procedures for DNA Functionalized Nanorod/arrays

DNA-nanorod conjugates were washed to remove excess and unbound DNA strands by centrifuging the nanorod conjugates for 3 minutes at 8k RPM (Eppendorf 5145D rotor), removing the supernatant, and resuspending the pellet in washing buffer. This washing step was repeated two addition times, and after the third removal of supernatant the pellet was resuspended in a desired volume of assay buffer. Probe DNA (suspended in assay buffer) and/or target oligonucleotide (suspended in assay buffer) was added to this solution and the mixture was allowed to incubate overnight on Thermomixer® at 23°C and 800 RPM. In order to isolate hybridized DNA-nanorod structures for characterization, the conjugates were centrifuged and resuspended in assay buffer. This washing process was then repeated four times, and after the fifth removal of supernatant, the pellet was resuspended in a desired volume of 50mM ammonium acetate in NANOpure water (50 – 100 µL) for analysis by Raman spectroscopy.

### 5.2.4 Characterization by Raman Spectroscopy

To analyze the hybridized nanorods/array or to analyze simple DNA-conjugated nanorod/arrays, a 40 µL aliquot of the ammonium acetate solution suspension was drop cast onto a piranha-treated glass slide and allowed to dry. Use of ammonium acetate prevented the formation of large salt crystals which can inhibit characterization. The sample was mounted and

rods were focused at 100× magnification using conventional optics. Analysis was carried out using a Raman laser power density of approximately 104 $W/cm^2$ and image scans were performed with the following parameters: integration time = 0.1 s/pixel, points per line = 128, lines per image = 128.

### 5.2.5 Characterization of DNA Loading on Au Nanodisk Array

A sample of DNA-functionalized nanoarrays was prepared as described above. A 4 µL aliquot of these structures were analyzed by using a Cell-VU hemocytometer and dark field microscopy at 50× magnification. Using this method to count the number of NDCs in a controlled local volume, the concentration of NDCs in a typical solution was calculated (2 fM). The amount of DNA on the nanoarray was determined by dissolving the structure in 0.1M KCN for 1 hour at room temperature, and analyzing the resulting solution using the Oligreen® assay (Invitrogen). By coupling cytometry data with results from the Oligreen® assay the average number of ssDNA oligonucleotides on a single disk was determined ($1.99 \times 10^5 \pm 15\%$ strands). Note that it is necessary to used hemocytometry in this case because neither extinction spectra nor ICP-MS can be used with OWL structures due to low resolution of absorbance optical features, and the silica backing respectively.

### 5.2.6 Preparation of Au Nanoprisms and Nanorods for Cellular Transfection

Au nanoprisms were prepared as described in Section 2.2,; nanorods and arrays were prepared according to literature protocols[72] These structures were subsequently conjugated to thiolated oligonucleotides that were 28 bases in length, which consisted of a block of 18 mixed bases, a block of 10 adenine bases, and a 3'-thiol modifier (5'-GAG CTG CAC GCT GCC GTC AAA AAA AAA A- SH- 3'), (conjugation was carried out according to methods described in section 4.2.3). These oligonucleotide sequences were synthesized on an Expedite 8909

Nucleotide Synthesis System (ABI) using standard solid-phase synthesis and reagents (Glen Research). All sequences were HPLC purified following synthesis. Functionalized nanoparticles were separated from free oligonucleotides via three consecutive centrifugation steps (8k rpm, 3 min) and washed with phosphate buffered saline solution (PBS) (137 mM NaCl, 10 mM phosphate, 2.7 mM KCl, pH 7.4, Hyclone) after each centrifugation interval. At this stage, oligonucleotide nanoparticle conjugates are generally re-suspended in PBS buffer and filter sterilized using a 0.2 μm acetate syringe filter (GE). However, Au nanoprisms and nanorods are two large to undergo such a filtration procedure without significant particle loss. Therefore, great must be taken to maintain sterile conditions through the washing procedure. Fresh, nuclease free buffers, centrifuge tubes, and pipette tips are opened immediately prior to use. Pipettes, benchtop, testube racks, and gloves, are all sprayed copiously with an 80% ethanol/water mixture. Sterile, DNA-conjugated anisotropic nanoparticles were then transfected using published procedures.[25, 26]

*N. B. In the previous section, an effort has been made to include only the synthetic procedures developed or expanded by the author. All other experimental techniques are referenced to literatures sources, except where they are useful for clarity.

### 5.3 Nanodisk Codes

Encoded materials are used for many applications, including cryptography, computation, brand protection, and labeling in biological and chemical diagnostics.[13, 219, 220] Often, nanostructures are appealing materials for encoding applications because they can be dispersed or hidden in a variety of media due to their small size, and their chemical and physical properties can be rationally designed in a variety of ways. [221-223] In addition, certain types of nano- and micromaterials are beginning to find application as probes in sensitive and selective molecular diagnostic systems.[13, 224, 225] These materials include nanoparticles labeled with Raman

chromophores [19], striped nanorods,[226-229] and several types of beads modified with fluorophores such as organic dyes and inorganic quantum dots.[225] Striped nanorods are a particularly interesting class of materials because they are dispersible entities, allow for massive encoding based upon the length and location of individual chemical blocks within the structures, and can be functionalized using conventional surface chemistries.[226] These nanostructures are typically identified by reflectivity or fluorescence. However, the high degree of overlap between common fluorescent labels, the quenching properties of the metal blocks that comprise the structures, and difficulty in resolving differences in metal reflectivity represent limitations for these systems.[226, 227]

Recently, we reported a process called On-Wire Lithography (OWL) that allows one to tailor the physical and chemical structure of nanorods to generate a class of nanostructures not accessible by any known synthetic or lithographic process.[230, 231] Specifically, one can make dispersible, segmented nanorod structures of fixed diameters with well-defined metal block sizes along the length of the nanostructure. Gaps between these metal sections also can be fabricated with dimensions from 2 nm to many-micrometers. This extraordinary degree of tailorability has allowed us to probe the relationship between feature size, gap size, and Raman enhancing properties in such a way that we can identify the maximum enhancing structure for a class of disk materials fabricated by OWL.[231] By site isolating disk pairs along the long axis of a nanorod, we can use confocal Raman microscopy (CRM) to independently address each disk pair. Based on the observation that one can create Raman hot spots at specific locations along the long axis of the rod, we hypothesized that one could use disk pair structures that exhibit large enhancements in a novel encoding scheme. Once functionalized with the appropriate chromophores, these nanodisk codes (NDCs), can be easily identified by Raman spectroscopy,

and take advantage of the well known surface-enhanced Raman scattering (SERS) phenomenon [231-235]. In principle, one can generate a myriad of nanodisk codes simply by varying the number and location of the pairs as well as the type and number of chromophores used as spectroscopic labeling agents. This multi-level approach to encoding nanostructures avoids some of the limitations of striped barcodes by transitioning weaknesses such as fluorescence quenching into advantages in the context of the Raman format. This section will describe these use of these structure in the context of nucleic acid detection.

### 5.3.1 Nucleic Acid Detection using NDCs and AuNPs

The binary physical encoding coupled with the high sensitivity Raman readout makes these disk codes attractive as probes in biological detection schemes. Accordingly, we have investigated the use of NDCs in a three-strand sandwich assay for nucleic acid detection. In these experiments, thiol-modified single-stranded DNA (ssDNA) molecules were attached to the NDC surfaces according to previously published protocols used for gold spherical nanoparticles.[13] These oligonucleotides contained a sequence complementary to one-half of a target ssDNA sequence. The remaining half of the target sequence is complementary to a reporter strand that contains a Raman-active label (Cy3) (Figure 5.1A). Because the disk pairs generate a SERS-enhancement factor of over 8 orders of magnitude, even a small number of binding events can be detected by CRM (Fig. 5.1A, **5**). Using this approach, we have detected target DNA at concentrations ranging from 5 μM to 5 pM (Figure 5.2). A control experiment containing the same amount of reporter sequences and NDCs, but with no target DNA does not show a discernable Raman signal (Fig. 2B, C). Statistical variations at low concentrations of target preclude homogenous functionalization across disk pairs in the NDC, and thus signal intensity is not identical from each section of the NDC. However, since each NDC can be read out in 5

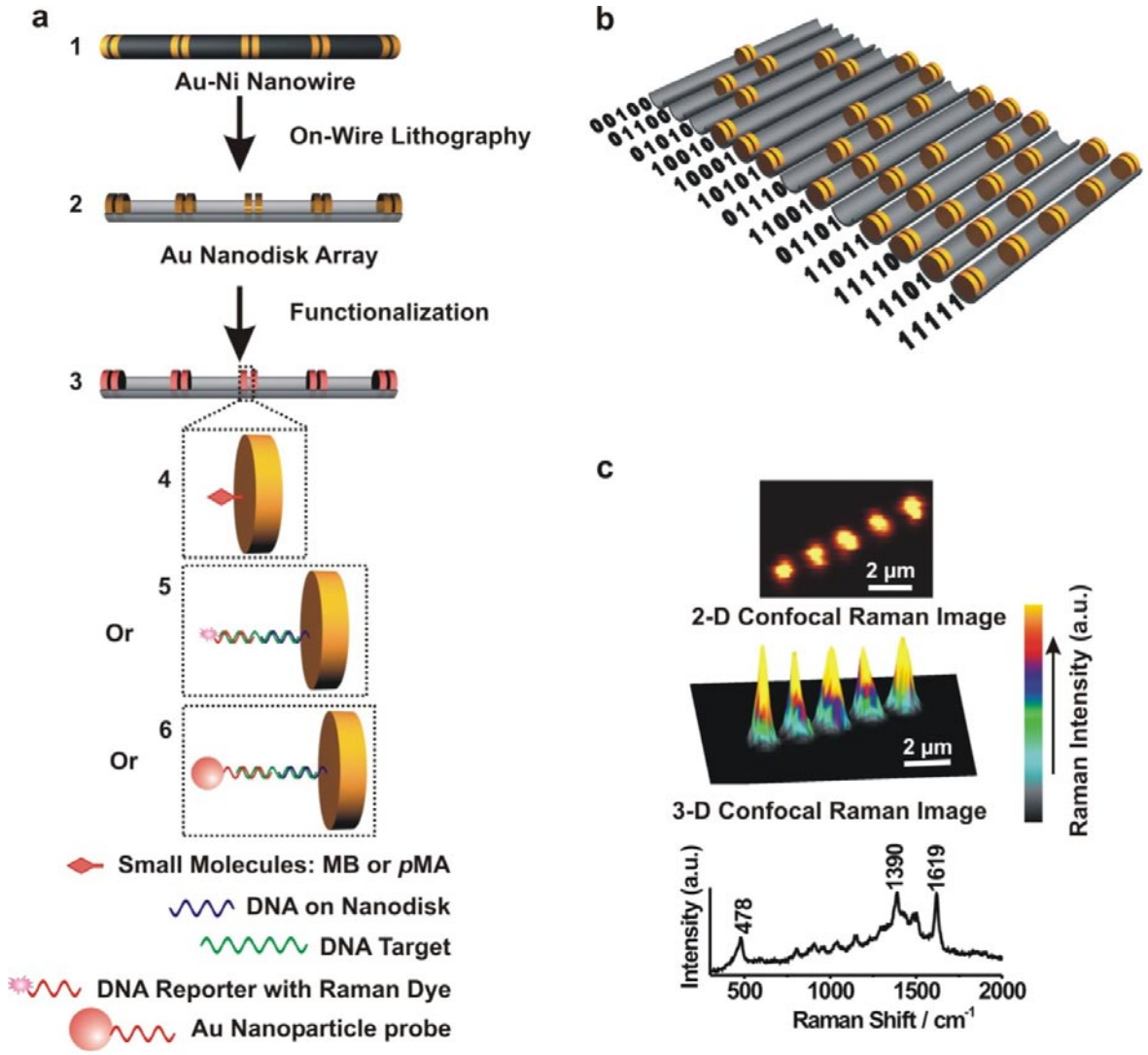


**Figure 5.1** (A) Scheme of NDC synthesis and functionalization; (B) 13 possible 5-disk-pair NDCs with corresponding binary codes. (C) Two- (top) and three-dimensional (middle) scanning Raman microscopy images of a 11111 NDC. Representative Raman spectrum of methylene blue (bottom) taken from the center of the hot spot generated in the middle disk pair shown in the Raman maps above.

minutes or less, it is trivial to scan multiple NDCs to confirm encoding patterns. These experiments demonstrate that the assay based upon NDCs and CRM readout has a low detection limit when conventional Raman dyes are used, in the absence of secondary amplification schemes.

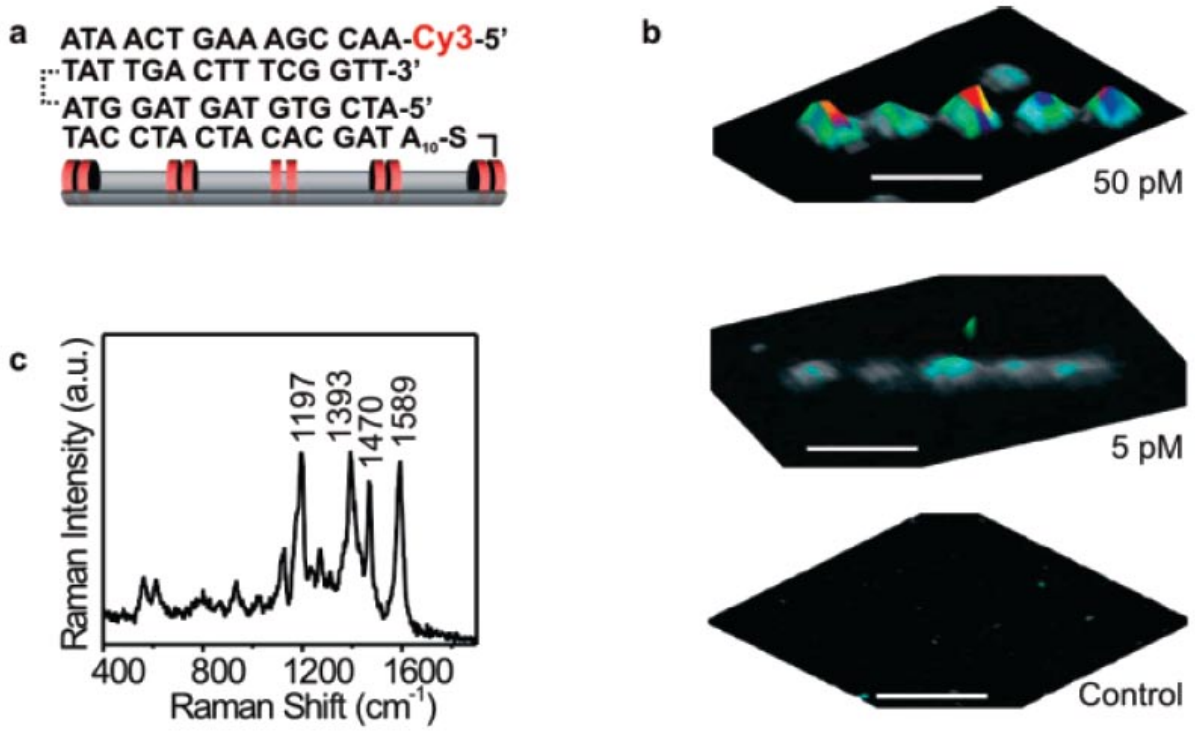


**Figure 5.2** (A) Schematic representation of three-strand DNA system, including DNA sequences used in these experiments. (B) 3D scanning Raman images of DNA detection results at target concentrations of 50 pM, 5 pM, and control with no target (top to bottom, respectively). All three images are graphed with the same z-scale. The control experiment (with only reporter and NDC strands, and no target) does not give any readable response. (C) A representative Raman spectrum taken from 3D spectra in (B).

Additional sensitivity can be gained if one immobilizes reporting DNA strands on Au nanoparticles (13 nm ± 2 %). Using the Raman-dye modified AuNPs has the potential to generate a 100-fold increase in signal intensity due to ~100 additional labeled strands being brought into the Raman hotspot per AuNP binding event.[209] The nanoparticle also quenches the fluorescence of the Raman dye, which has been shown to interfere with Raman scattering [236]. Using the NP-target-NDC sandwich assay **6** (Figure 5.1A), a detection limit of 100 fM is achievable (Figure 5.3). A control segment shows no discernable response, and SEM confirms no significant NP binding to the NDCs.

The NDC methodology is also attractive because, in principle, it has an inherent multiplexing capability due to the "barcode" nature of the structures. To confirm and demonstrate this capability, we employed a three-strand DNA detection system as described above wherein 11011 nanodisk codes are functionalized with an oligonucleotide sequence (called "$NDC_{11011}$") that we designed to be complementary to a section of a DNA target ($target_{11011}$). The complement to the second half of this target sequence contained a Cy5 reporter molecule ($reporter_{11011}$) (Figure 5.4). In a different solution, we functionalized 10101-encoded NDCs with a second sequence ($NDC_{10101}$), which is complementary to one half of a second DNA target ($target_{10101}$); the complement to the second half of this target sequence contained a TAMRA reporter molecule ($reporter_{10101}$) (Figure 5.4A). We then mixed the functionalized 11011 and 10101 NDCs, both target sequences, and both reporter strands in the same solution and allowed the oligonucleotides to hybridize at 37 $^{o}$C. When both $target_{11011}$ and $target_{10101}$ are present, positive images are obtained for both 11011 and 10101 disk codes (Figure 5.4B). Because the Raman image map contains full Raman spectral

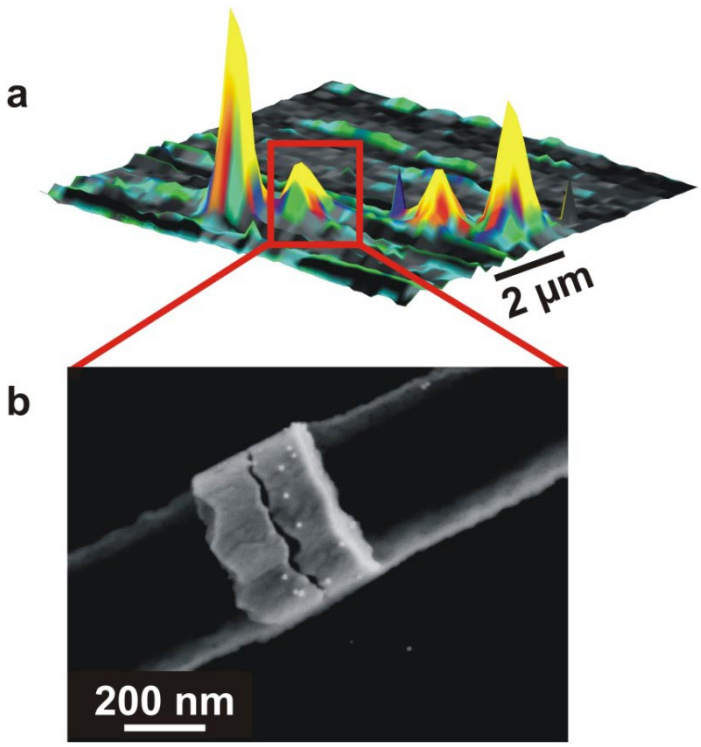


**Figure 5.3** NP-target-NDC sandwich assay. (A) Three-dimensional scanning Raman image of 11011 NDC after functionalization with ssDNA and hybridization with 100 fM target concentration and reporter NPs. (B) FE-SEM image of NPs immobilized on disk-pair surface.

information for both Cy5 and TAMRA embedded in every pixel, we were able to specifically monitor the Raman band ranging from 525.2 $cm^{-1}$ to 592.4 $cm^{-1}$ from Cy5 and apply a filter to the signal output (blue bar, Fig. 5.4E). By doing so, we have demonstrated that only $target_{11011}$ and $reporter_{11011}$ DNA are present on 11011 disk codes (Figure 5.4C). Likewise, we have monitored the Raman band ranging from 1630.0 $cm^{-1}$ to 1679.0 $cm^{-1}$ from TAMRA, applied a similar filter (red bar, Figure 5.4E), and demonstrated that only $target_{10101}$ and $reporter_{10101}$ were present on 10101 disk codes (Figure 5.4D). It is important to note that the multiplexing ability of this system is a result of the binary coding architecture and the different Raman dyes. In this case, two Raman dyes are used in this case simply to illustrate the specificity of the system.

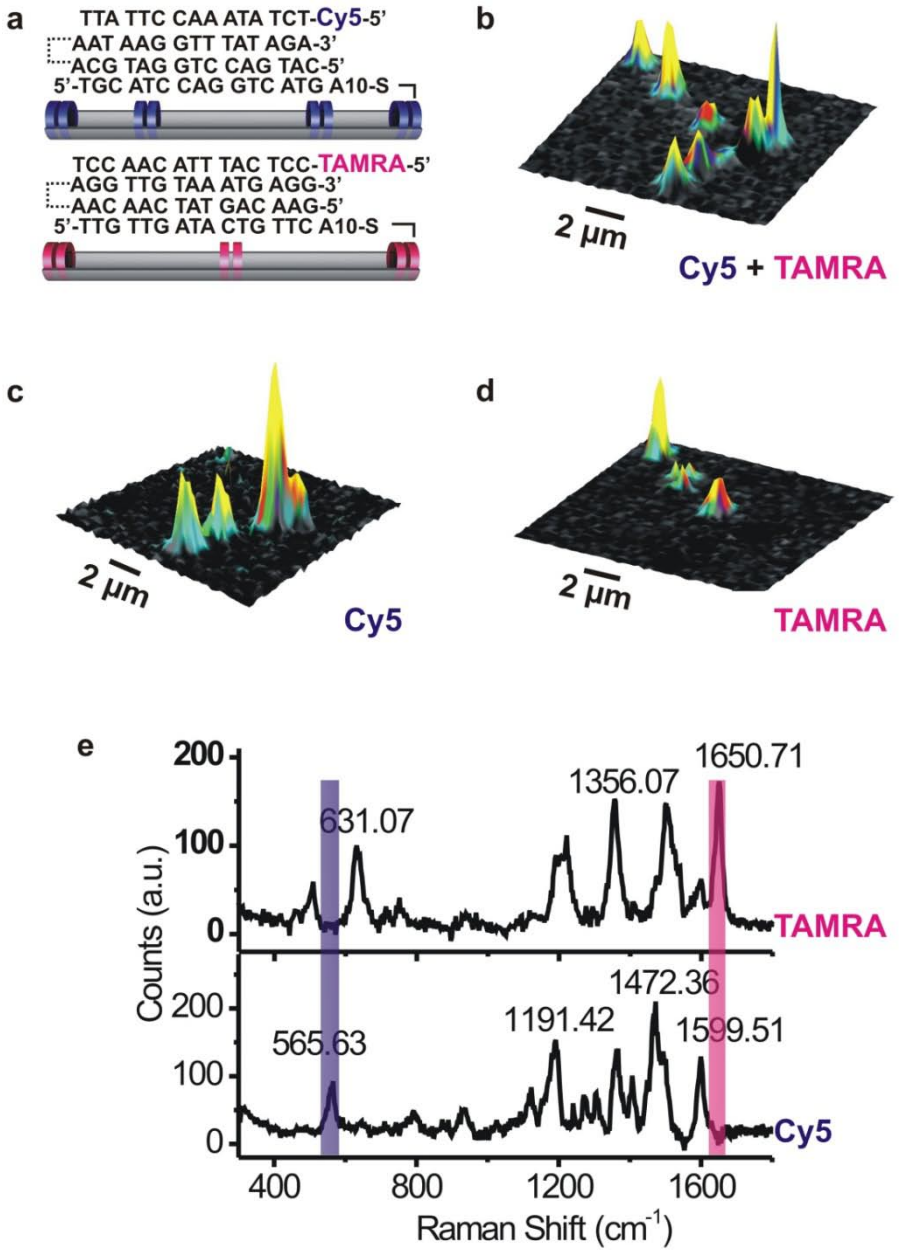


**Figure 5.4** Multiplexing with NDCs. (A) Scheme of 11011 and 10101 NDC nanostructures showing DNA sequences of target, reporter, and NDC strands. (B) Full-spectrum 3D scanning Raman image of 11011 and 10101 disk codes functionalized with different single-stranded DNA sequences. (C) Filtered Raman image of (B) where the transmitted frequencies are indicated by the blue bar in (E), corresponding to a unique Raman band from the Cy5 reporter (525.2-592.4 $cm^{-1}$). (D) Filtered Raman image of (B) where the transmitted frequencies are indicated by the red bar in (A), corresponding to a unique Raman peak from the TAMRA reporter (1630.0-1679.0 $cm^{-1}$). (e) Raman spectra of Cy5 and TAMRA from reporter DNA sequences immobilized on NDC after DNA hybridization. N.B. (C,D) are taken with only a fraction of the total Raman signal being collected; the three images in (B-D) do not have the same *z*-scale and have been normalized for a straightforward comparison.

**5.4 Cellular Uptake of Au Nanoprisms**

In addition to successful use in advancing biodiagnostics[13], oligonucleotide-nanoparticle conjugates are also now being used in gene and cancer therapeutics.[25, 26, 215] It is particularly interesting to envision the use of nanostructures other than pseudo-spherical nanoparticles, because of the wide range optical features afforded by their anisotropic counterparts. For example, Halas *et al.*[27] have used gold nanoshells to shrink cancerous tumors by inducing destructive levels of local heating that is mediated by the excitation of the nanoshell SPR. Likewise, El- Sayed *et al.*[28] have used the SPR of Au nanorods to possibly transfect cells, and elicit local heating to destroy the surrounding tissue.

These reports are just the first examples of the many possibilities afforded by the optical features of anisotropic materials. For example, if SPR-induced heating could be modulated (e. g. by laser power), it may be possible to selectively release hybridized DNA strands based solely on DNA melting temperature and wavelength of irradiation. This remotely initiated, SPR-mediated heating could then be used to effect a number of extremely interesting applications based on heat-related stimuli. Yet there are barriers to such a vision, not least of which is the size of anisotropic nanoparticles.[99] Nanoparticles with optical features at wavelengths greater than 1000 nm (the wavelength range transparent to biological tissue and also to water)[215] generally have at least one dimension greater than 100 nm and this may affect the ability of cells to take-up these particles.

In this section, preliminary work on the factors influencing Au nanoprism uptake are presented. First, DNA-Au nanoprism conjugates were prepared where the DNA strands contained a Cy5 fluorescent label for visualization using confocal microscopy. Au nanoprisms were transfected into three different cell lines (A549, Hep, SiHa) and at three concentrations (~ 1

pM, 500 fM, and 250 fM) and compared to control cells of each type (Figure 5.5). Interestingly, significant uptake of nanoprisms was observed (as measured by fluorescence intensity) in each case as compared with control. Qualitatively, these results also show that cellular uptake scaled with initial nanoparticle concentration, which is a trend that has been observed previously for DNA-conjugated pseudo-spherical nanoparticles.[26]

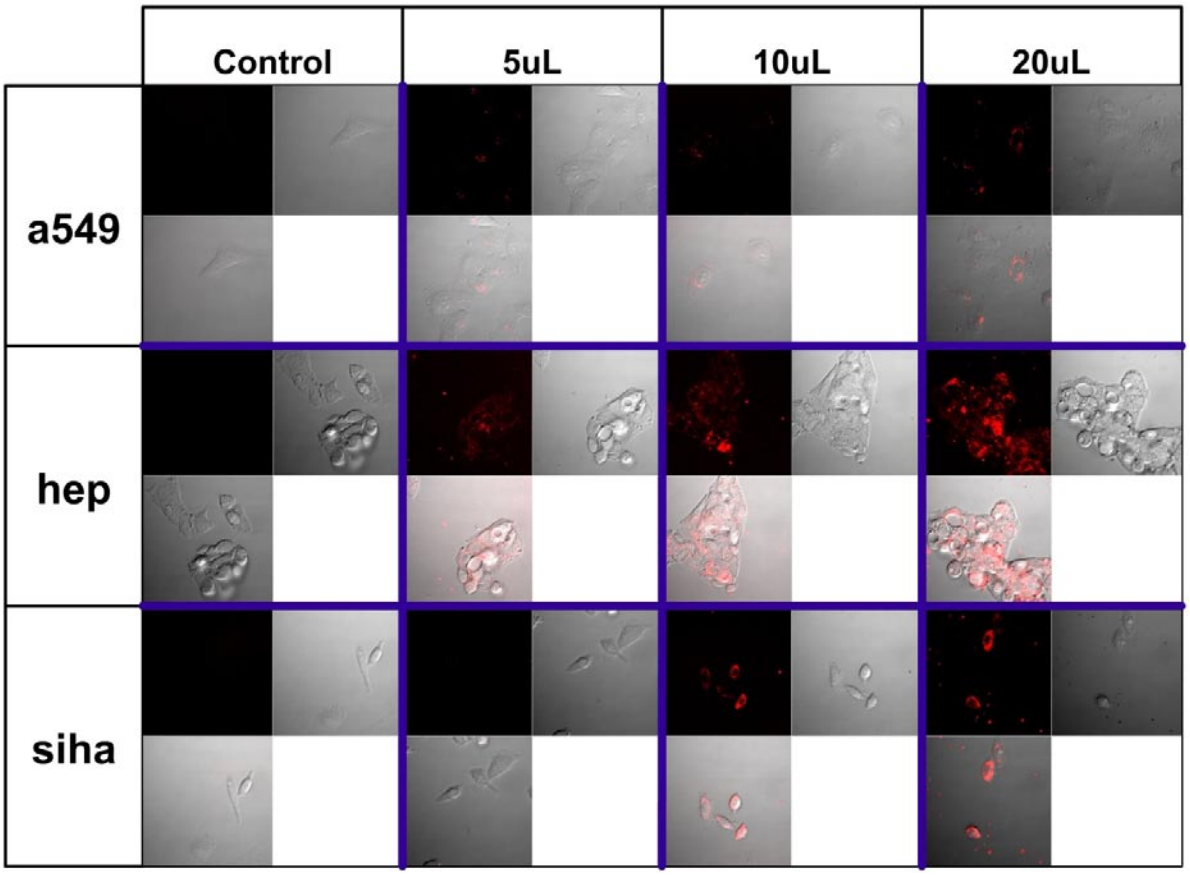


**Figure 5.5** Confocal microscope images showing fluorescence signals from 3 different cell lines, transfected with 3 different concentrations of Au nanoprisms. The volumes at the top of the image correspond to 0.25, 0.5, and 1.0 pM Au nanoprisms, respectively.

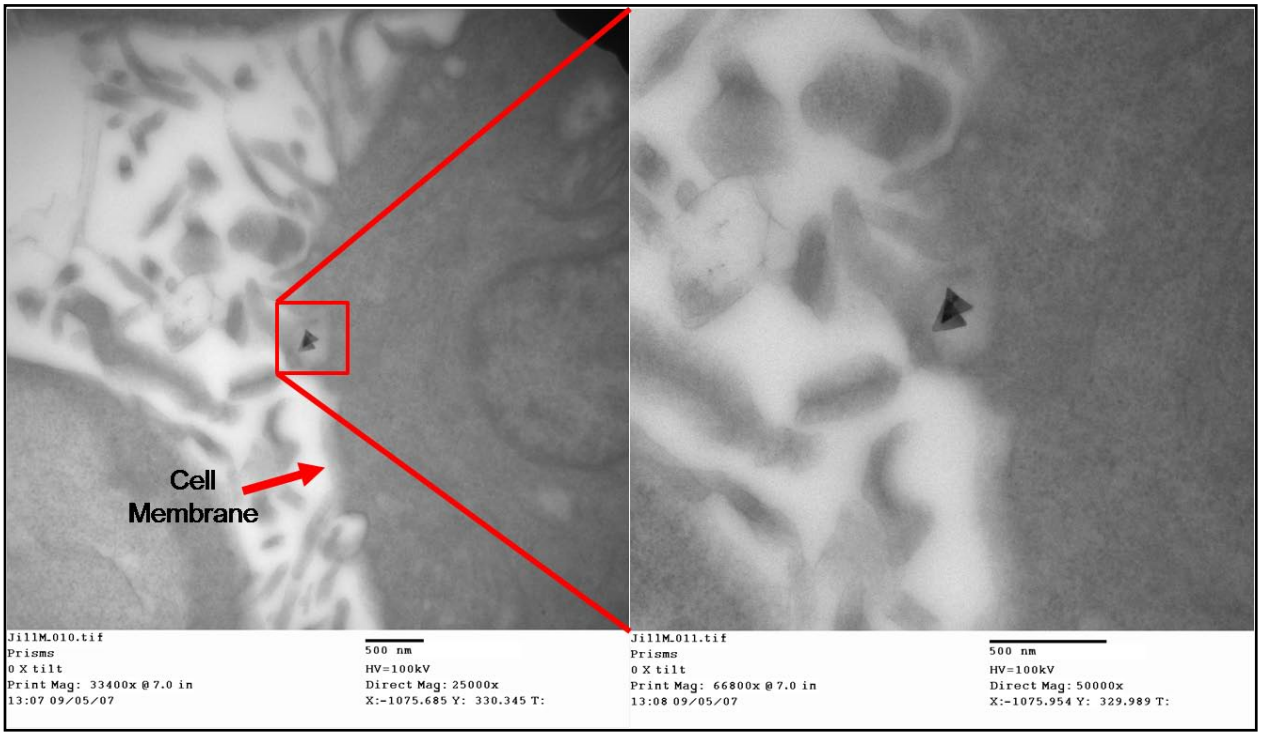


**Figure 5.6** TEM images of HeLa cell transfected with DNA-functionalized Au nanoprisms. Left image is a magnified view of the vesicle containing nanoprisms.

The uptake of Au nanoprisms was confirmed by TEM using HeLa cells that had been transfected with Au nanoprisms (~ 1 nM) (Figure 5.6). However, electron microscopy analysis indicated markedly lower uptake of Au nanoprisms than what was expected from the fluorescent optical microscopy experiments. This may be attributed to nanoprisms "sticking" on the outside of transfected cells despite repeated washing, and this adhesion may arise from the extended area of the triangular faces and the increased possibility of strong electrostatic interactions. Conversely, the low uptake observed by TEM may be attributed to the relatively low concentration of Au nanoprisms used to transfect the cells. Pseudo-spherical nanoparticle concentrations for transfection are generally between 1 and 60 nM[26] whereas Au nanoprism concentration used in these experiments are multiple orders of magnitude less concentrated (250 fM – 1 pM). Yet it is not trivial to increase the concentration of such particles due to the low

concentration of the as-synthesized structures, and the tendency for high concentrations to aggregate.

Taken together, these results are promising for the transfection of anisotropic materials into cells, and the use of these materials in SPR-mediated imaging and therapies. Further, these results provide a foundation for future experiments in terms of critical factors in the efficacy of such anisotropic nanoparticle-based schemes.

# CHAPTER SIX

Iodide Ions Control Seed-mediated Growth of Anisotropic Gold Nanoparticles

Portions of this chapter have been published in: *Nano Letters*, **2008**, *8*, 2526**.**

## 6.1 Introduction

Efforts to generate nanoparticles of various sizes and shapes have produced a library of materials that allow one to observe the close relationship between nanostructure properties and physical architecture. These structure-dependent behaviors are of enormous interest for applications in photonics,[43, 237] catalysis,[238] nanoelectronics,[64] and therapeutics.[25, 27, 65] For colloidal nanorods and nanoprisms made of gold, the preferred synthetic route is a seeding methodology. However, it is well known that certain methods used to synthesize these particles are often irreproducible and difficult to control.[103, 178] On the one hand, researchers have pointed to the importance of the surfactant (cetyltrimethylammonium bromide, CTAB), including surfactant concentration, counterion, alkane chain length, and even chemical manufacturer, on the yield and morphology of the resulting colloids.[90, 174, 178] On the other hand, researchers have also pointed to synthetic additives such as metal or halide ions as major factors in directing crystal growth.[77, 166, 239] However, there is not a strong connection between these observations, and this has resulted in the development of numerous methods to access similar nanoparticle architectures.[79-81, 84, 85] These methods contain varied, sometimes contradictory, reports of the shape-directing factors in a given preparation.[103, 165, 166, 178] For example, Sastry *et al.* report the suppression of gold nanoprism growth with the addition of iodide ion ($I^-$) whereas Ha *et al.* report that the presence of $I^-$ promotes nanoprism formation.[165, 166] In recent work, it was also shown that only CTAB obtained from certain manufacturers could produce nanorods, whereas other CTAB produced only pseudo-spherical particles.[178] In our work, we have observed both batch to batch CTAB sensitivity and an unexpected presence of $I^-$ on the surface of gold nanoprisms (*vide infra*). Therefore, understanding the links between these seemingly disparate

reports could provide valuable insight into the critical shape-directing factors involved in seed-mediated nanoparticle syntheses.

Herein, we report the controlled synthesis of gold nanorods, nanoprisms, and nanospheres under a unified framework that addresses previously reported results regarding the role of halide additives and the cationic surfactant, CTAB. The experimental approach focuses on understanding how to control shape using CTAB-based, seeding methodology, and is guided by the observation of $I^-$ on Au nanoprisms using X-ray Photoelectron Spectroscopy (XPS, *vide infra*). This observation is surprising since there is no apparent source of $I^-$ anywhere in the synthesis (or other syntheses using similar approaches) .[77, 90, 178, 187] Interestingly, identical syntheses and seed particles could be used to form all three nanoparticle architectures, where the final shape was controlled by modulating only the iodide ion concentration in the reaction mixture. Importantly, the source of iodide in previous CTAB-based, seed-mediated synthesis[16] has been identified as the CTAB itself, which may explain the variability associated with its use.

## 6.2 Experimental

### 6.2.1 Materials for Anisotropic Nanoparticle Synthesis

Hydrogen tetrachloroaurate trihydrate ($HAuCl_4 \cdot 3H_2O$, 99.9%), sodium borohydride ($NaBH_4$, 99.995%), sodium hydroxide (NaOH, 99.998%), L-ascorbic acid (99%), trisodium citrate (99%), potassium iodide (99%), sodium iodide (99%), lithium iodide (99%) were obtained from Aldrich and used as received. Bis (p-sulfonatophenyl) phenylphosphine dihydrate dipotassium (BSPP) was purchased from Strem Chemicals, Inc. CTAB was ordered from various manufacturers with various purities (Table 6.1).

| Chemical Reagent | Manufacturer, Purity, Batch Number | Iodide concentration in 0.01% aqueous CTAB solution (nM) |
|---|---|---|
| $HAuCl_4$ | Aldrich, 99.99% | - |
| Ascorbic Acid | Aldrich, 99+% | - |
| NaOH | Aldrich, 97% | - |
| $NaBH_4$ | Aldrich, 99.995% | - |
| Trisodium Citrate | Aldrich, 98% | - |
| CTAB #1 | Sigma, 99%, #095K0187 | - |
| CTAB #2 | Aldrich, 95%, #06901CD | 6.3 |
| CTAB #3 | Aldrich, 95%, #0590BH | - |
| CTAB #4 | Aldrich, 95%, #06602KC | - |
| CTAB #5 | GFS Chemical, 98%, #P452770 | 15.7 |
| CTAB #6 | Recrystallized CTAB #2 | - |

**Table 6.1** Iodide Concentrations of Reagents Used in Syntheses as Analyzed by ICP-MS

### 6.2.2 Preparation and Recrystallization of Cetyltrimethylammonium Bromide (CTAB)

For all experiments, 0.05 M CTAB was prepared by dissolving 2.733 g of CTAB in 150 mL of NANOpure™ water. The solution was sealed with parafilm and heated until it appeared completely clear. This sealed solution was then sonicated for ~30 s, to ensure that all CTAB was dissolved. The solution was cooled to room temperature on the benchtop before use in subsequent syntheses (~ 2 h).

To purify CTAB, 10 g samples of CTAB (SigmaUltra, Aldrich Chemical Company) were dissolved in a warm ethanol/water mixture (10:1) (~150mL) and recrystallized at 4$^{o}$C. The crystals were isolated by Buchner filtration, washed with ethyl ether, and dried in a vacuum oven at 55$^{o}$C for 6 h. The process was then repeated 2 additional times for each 10 g sample, so that CTAB had been recrystallized three times before being used in the experiments.

### 6.2.3 Synthesis of Anisotropic Gold Nanoparticles

In a typical experiment, all glassware was washed with aqua regia and rinsed copiously with NANOpure™ water (see Chapter 2, section 2.2 for additional details). Gold nanoparticle

seeds were prepared by reducing 1 mL of 10 mM $HAuCl_4$ with 1 mL of 100 mM $NaBH_4$ while stirring vigorously. The reduction was done in the presence of 1 mL of 10 mM sodium citrate and 36 mL of fresh, NANOpure water. Upon addition of the $NaBH_4$, the solution turned a reddish-orange color and was allowed to continue stirring for one minute. The resulting mixture was aged for 2 - 6 hours in order to allow the hydrolysis of unreacted $NaBH_4$. The gold nanoparticle seeds exhibited a plasmon resonance peak at 500 nm, and had an average diameter of 5.2 ± 0.6 nm (see Chapter 2, Figure 2.1).

After the aging period, three growth solutions were prepared for the seed-mediated growth step. The first two solutions (**1** and **2**) contained 0.25 mL of 10 mM $HAuCl_4$, 0.05 mL of 100 mM NaOH, 0.05 mL of 100 mM ascorbic acid, and 9 mL of the prepared CTAB solution. The final growth solution (designated **3**), contained 2.5 mL of 10 mM $HAuCl_4$, 0.50 mL of 100 mM NaOH, 0.50 mL of 100 mM ascorbic acid, and 90 mL of the prepared CTAB solution. For syntheses involving the addition of iodide, controlled amounts of KI, NaI, or LiI were added to the original CTAB solutions such that growth solutions **1**, **2** and **3** were at the same iodide concentration. Final concentrations of 100, 75, 50, 25, 10, and 2.5 μM iodide were prepared by adding aliquots of a 0.1 M solution of either KI, NaI, or LiI to the previously prepared 150 mL CTAB solutions (prior to dissolving procedure by heating described in Section 6.2.2).

In all cases, particle formation was initiated by adding 1 mL of seed solution to growth solution **1**. The solution was shaken, after approximately two seconds,1 mL of growth solution **1** was added to **2**, **2** was shaken, and after approximately two seconds, all of the resulting growth solution was added to **3**. After the addition, the color of **3** changed from clear to deep magenta-purple over a period of 30 minutes for all preparations. Growth of the nanoparticles was complete after 2 h, as determined by absorbance spectroscopy (see Chapter 2, Figure 2.4).

### 6.2.4 Synthesis of Ag Nanoparticles (AgNPs)

A 250 mL three-neck flask was cleaned using aqua regia (see Chapter 2, section 2.2 for additional details), and to it was added 95 mL of NANOpure water. This flask was then immersed in an ice bath, and the solution bubbled with $N_2$ in the dark under vigorous stirring for ~30 minutes. One mL of 10 mM $AgNO_3$ and 1 mL of 30 mM trisodium citrate were added into the solution. Immediately afterward, 1 mL of aqueous $NaBH_4$ (50 mM, freshly prepared with ice-cold NANOpure water prior to injection) was rapidly injected into the solution. Over the next 15 min, 5 drops of $NaBH_4$ solution were added every two minutes into the solution. Then 1 mL of BSPP solution (5 mM) and 1 mL of $NaBH_4$ solution were added dropwise to the reaction mixture. The resulting Ag colloid was gently stirred for 5 h in an ice bath and allowed to age overnight at 4°C in the dark. The AgNPs had an average diameter of 4.2 ± 0.9 nm as measured by TEM.

### 6.2.5 ICP-MS Analysis

Inductively Coupled Plasma-Mass Spectrometry (ICP-MS; Thermo-Fisher) analysis was performed using an Argon gas generated plasma and a 5% $NH_4OH$ aqueous matrix.[240] Experimental ICP-MS values were compared to a standard curve generated using standards prepared from NaI by weight (1, 2, 5, 10, 25, 50, 100, and 200 ppb by weight) that were dissolved in the $NH_4OH$ matrix. A 1ppb Indium internal standard was added to the matrix and used in all measurements.

### 6.2.6 XPS Analysis

Particle solutions were washed by centrifugation at 8 kRPM for 3 min (using an Eppendorf 5145D centrifuge), and nanoparticle pellets were resuspended in 1 mL of NANOpure™ water. This process was repeated three times, and the final pellet was resuspended

in 200 µL of NANOpure™ water. Two 10 µL droplets of this mixture were applied to a silicon substrate (substrate was cleaned by sonication in ethanol, rinsed with acetone, and finally rinsed with water) and allowed to dry in a vacuum-sealed desiccator. The substrate was then rinsed again with water and dried under a stream of $N_2$.

After preparation, the sample was transferred to an analysis chamber equipped with an X-ray photoelectron spectrometer (XPS, Omicron). An aluminum Kα (1486.5 eV) anode with a power of 200 W (20 kV) was used. XPS spectra were gathered using a hemispherical energy analyzer operated at a pass energy of 70.0 eV for survey scans and 20.0 eV for elemental analysis. Binding energies were referenced to the $Au_{4f}$ peak at 84.0 eV for pure Au.

### 6.2.7 UV-vis-NIR Spectrophotometry and TEM Analysis

The seed mediated growth reaction of the nanoparticles was characterized by absorbance spectroscopy (UV-vis-NIR) using a Cary 5000 spectrophotometer in double-beam mode, baselined to the spectrum of NANOpure™ water. All nanostructures were characterized using a Hitachi-8100 transmission electron microscope (TEM) at 200kV.

## 6.3 Results and Discussion

### 6.3.1 Role of Iodide

For a typical CTAB-based, seed-mediated gold nanoparticle synthesis, small gold seed nanoparticles (d ≈ 4 - 6 nm) are prepared by $NaBH_4$ reduction of $HAuCl_4$, and used in a subsequent three-step growth of these particles in an aqueous solution containing a capping agent (most commonly, CTAB), gold ions ($HAuCl_4 \bullet 3H_2O$), reducing agent (ascorbic acid), and NaOH (to adjust pH and deprotonate ascorbic acid); together termed “growth solution”.[84, 187] In order to understand the origin of the $I^-$ in this synthesis, ICP-MS was used to analyze iodide

concentration in the CTAB, NaOH, $HAuCl_4$, ascorbic acid, sodium citrate, and $NaBH_4$ used to prepare the nanoparticles (Table 6.1). Only in the case of the CTAB was the presence of iodide detectable (ICP-MS detection limit for $I^-$ is ~1 ppb under the conditions studied)[240]. We analyzed five additional batches of CTAB from various manufacturers with varying purities (Table 6.1). Interestingly, only certain CTAB batches contained $I^-$. Each of the 5 CTAB batches was used in repeated trials of the seed-mediated synthesis. Using CTAB that contained detectable traces of $I^-$ (#2, #5), nanoprisms formed. For the other three CTAB samples, two produced various concentrations and distributions of nanorods, and one produced only pseudo-spherical nanoparticles (#1) (Figure 6.1). From these data, we hypothesized that the variation of seed-mediated syntheses based on CTAB may originate from variability in the observed iodide impurities.

In order to determine whether iodide is the impurity responsible for observed nanorod, nanoprism, and nanosphere results, CTAB was recrystallized (#2) using literature methods.[241] The recrystallized product was analyzed by ICP-MS, and no $I^-$ could be detected (#6). This purified CTAB was then used to analyze the *absolute* concentrations of $I^-$ necessary to produce a given shape morphology using

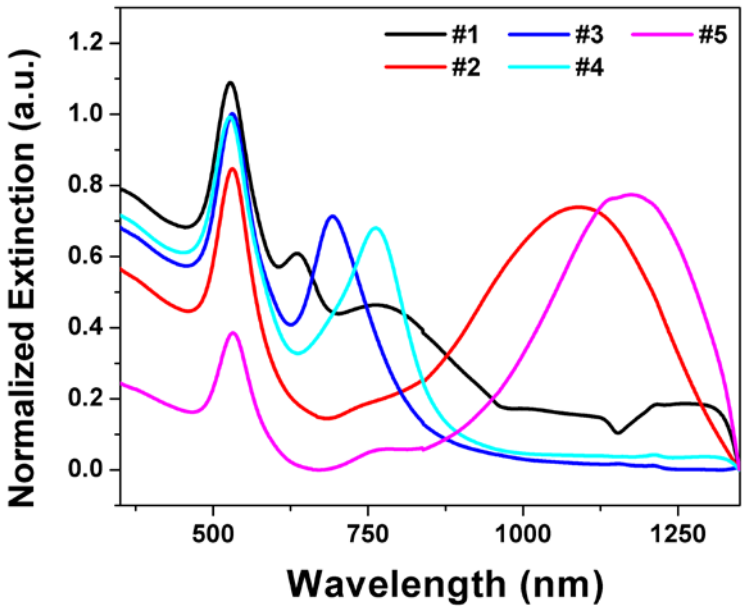


**Figure 6.1** UV-vis-NIR spectra of nanoparticles produced using 5 different CTABr batches. Each CTABr was used as received from the manufacturer.

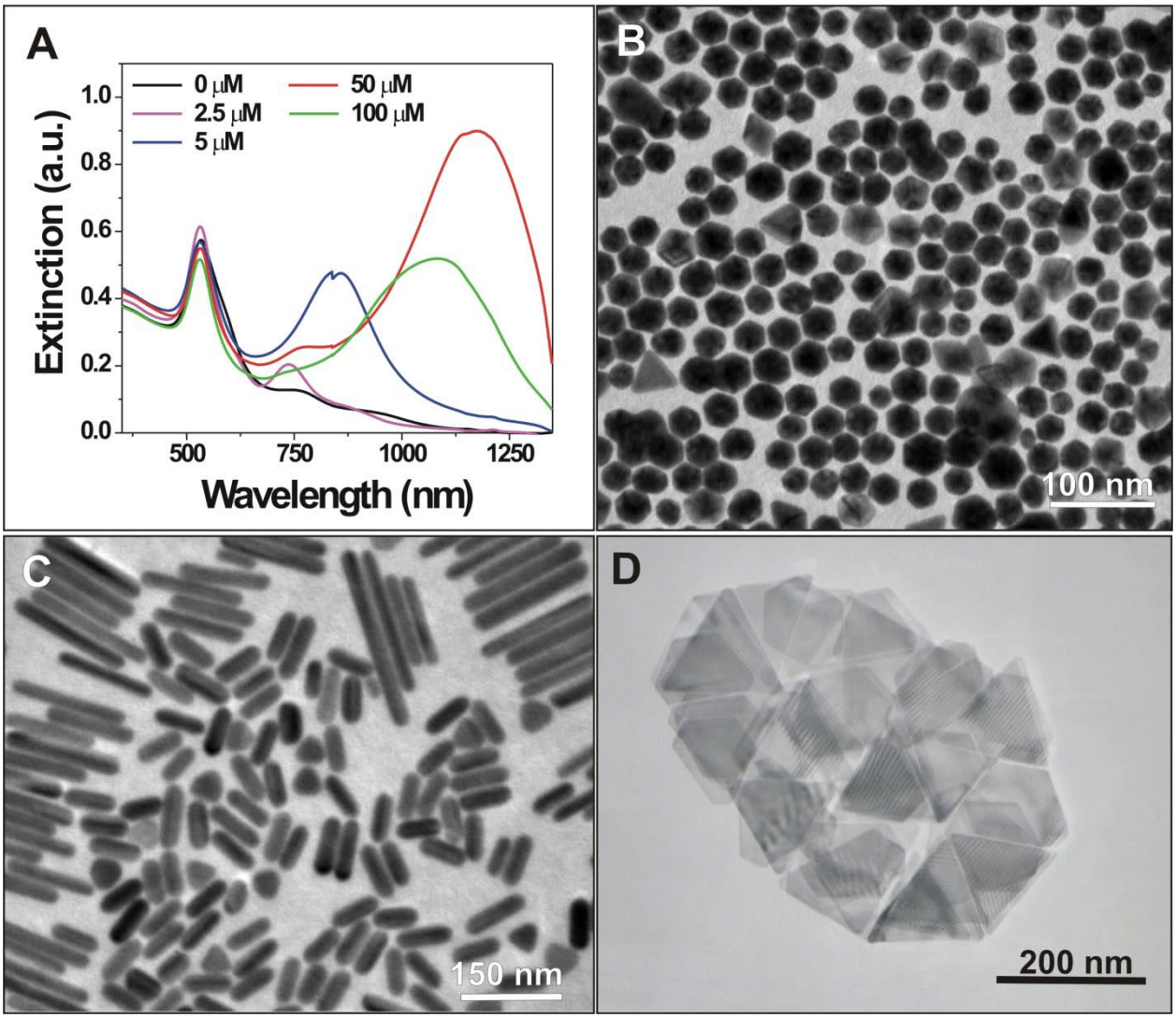


**Figure 6.2** (A) UV-vis-NIR spectra of nanoparticles made using various concentrations of $I^-$, and corresponding TEM images of (B) pseudo-spherical nanoparticles, (C) nanorods, and (D) nanoprisms.

seed-mediated methodology (it is important to note that others have concluded that use of CTAB from different manufactures leads to different results, but the cause of this variability has yet to be identified.)[178]. In a typical experiment, $I^-$ is introduced into the synthesis by adding aliquots of a NaI stock solution (0.1 M) directly into the CTAB prior to synthesis. Iodide concentrations of 0, 2.5, 5, 10, 50, and 100 μM were investigated, and the same nanoparticle seed batch was used to initiate each reaction, in order to control for the effects of the seed nanoparticle morphology (*vide infra).*

UV-vis-NIR spectra of the resulting solutions show a remarkable dependence of nanoparticle morphology on the presence of $I^-$ (Figure 6.2A). With no $I^-$ in solution, little anisotropic nanoparticle formation (< 10%) is observed. However, with low concentrations of $I^-$ (2.5 and 5 μM) a large population of nanorods can be observed (~ 45% yield before purification). As the concentration of $I^-$ increases (>10 μM), a mixture of nanoparticle morphologies is observed including rod, prism, and sphere. At 50 μM $I^-$ concentration, nanoprisms form in high yield as indicated by the strong dipole and quadrupole modes in the extinction spectrum (~ 65% yield before purification). However, at higher concentrations of $I^-$ (> 75 μM), plate-like growth continues but produces rounded, triangular and disk-like particles. This analysis, based on the bulk characterization afforded by UV-vis-NIR spectroscopy, was confirmed by TEM (Figure 6.2 B, C, and D). Interestingly, these results were not dependent on the counterion of $I^-$. In addition to NaI, KI and LiI produced similar results (Figure 6.3). To analyze the role of $I^-$ in these syntheses, we deposited nanoparticle solutions on silicon substrates for analysis by XPS. Interestingly, in all cases (both experiments using CTAB directly from the manufacturer and in experiments using purified CTAB and controlled introduction of $I^-$), iodide was only observed on samples composed of nanoprisms; samples from rods and spheres did not exhibit detectable $I^-$

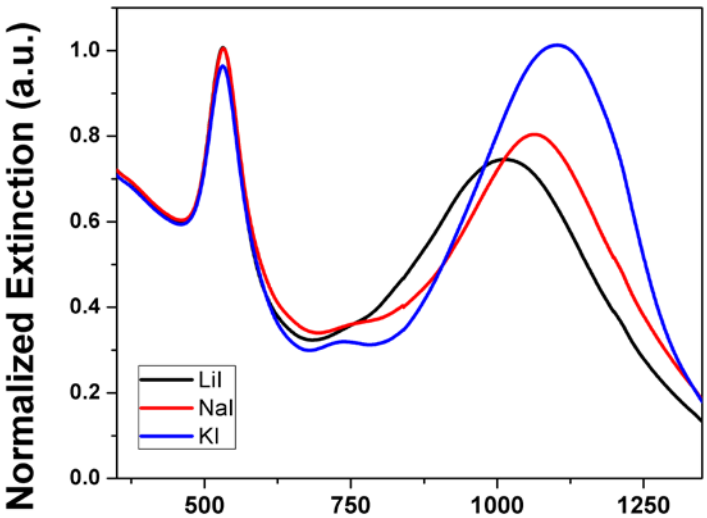


**Figure 6.3** UV-vis-NIR spectra of nanoprism solutions made using 50 µM concentrations of LiI, NaI, and KI. Each batch shows the characteristic dipole and quadrupole plasmon resonances of Au nanoprisms.

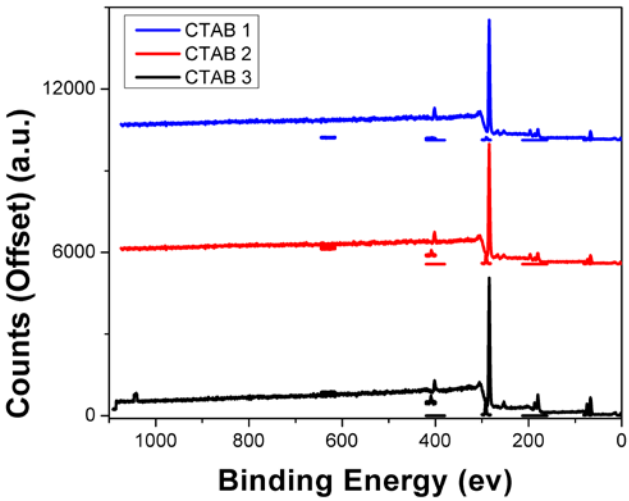


**Figure 6.5**. XPS Spectra of CTABr batches showing no presence of iodide.

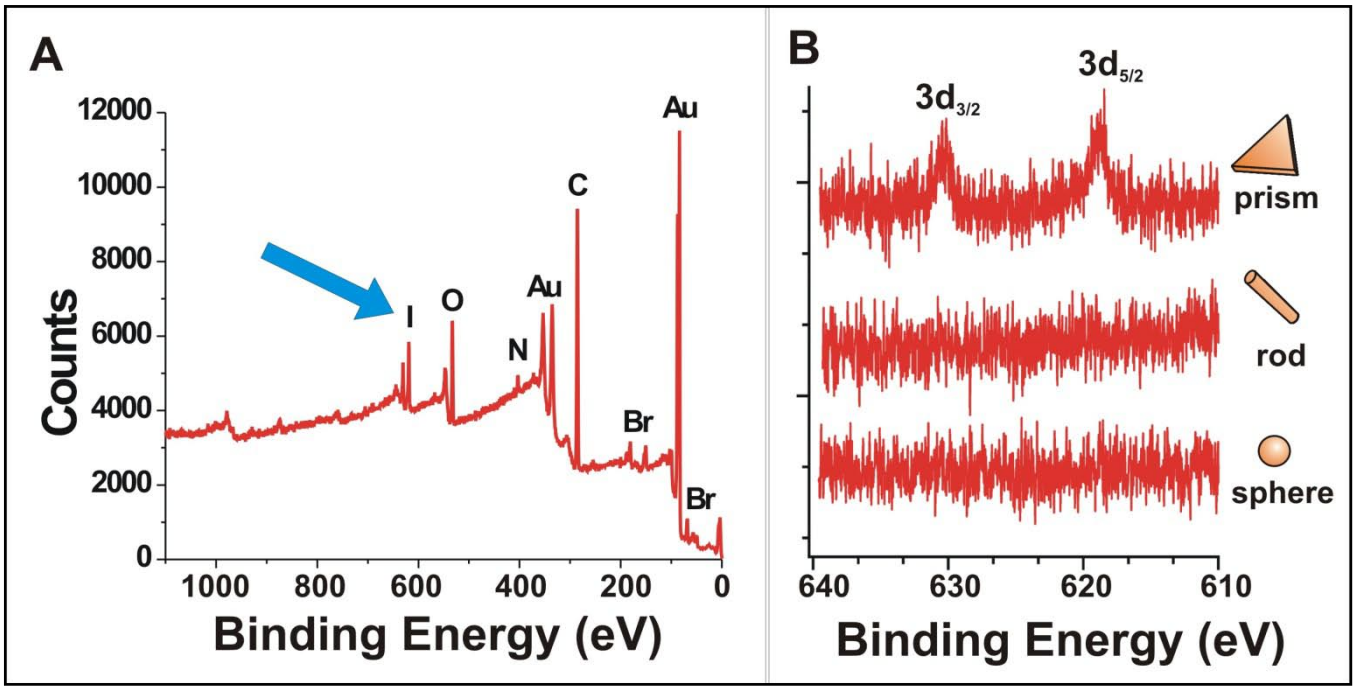


**Figure 6.4** XPS spectra (A) of gold nanoprisms; arrow indicates I- signal; (B) centered at binding energy of I- and taken from nanoprisms, rods, and pseudo-spherical nanoparticles. Spectra indicate I- only on nanoprisms.

signals by XPS (Figure 6.4 and 6.5). These results suggest that $I^-$ is bound to the (111) crystal facet of the nanoprisms which compose their broad triangular faces.[104] It is well known that halide ions adsorb on gold surfaces with binding energies that scale with polarizability ($I^- > Br^- > Cl^-$) and crystal facet ((111) > (110) > (100)).[149] In previous reports, it has been postulated that $I^-$ preferentially binds to the (111) facet of a growing nanoparticle, and prevents reaction at that surface.[165] However, reports describing this mechanism also pointed to competing shape directing factors such as pH, temperature, and surfactant counterion, and did not identify the original source of the $I^-$. We find that in standard CTAB-based, 3-step, seed-mediated conditions, $I^-$ is the dominant shape-directing moiety, more so even than the seed nanoparticle, as evidenced by the fact that the same batch of nanoparticles seeds can produce all three nanoparticle morphologies in high yield (*vide infra*). This observation indicates that although there may be multiple seed morphologies within a single seed nanoparticle solution, their growth into anisotropic structures is not dictated by the initial structure alone. Otherwise, a final shape would be the preferred outcome over the others, regardless of additional reagents.

The dependence of nanoparticle morphology on iodide concentration may be understood based on the preferential adsorption of iodide on the (111) crystal facet of Au.[149] Without iodide, a CTAB bilayer is present on all surfaces due to electrostatic forces, which leads to a lack of preferential growth and an isotropic nanoparticle. With slightly increased iodide concentrations iodide adsorbs on the (111) crystal facet (at the ends of the rod), leaving the (110) and (100) (the long axis facets of the rod) open for the adsorption of a close-packed CTAB layer that can limit the reduction of gold ions at these sites.[25,26] This model is consistent with previous observations for rod formation and offers additional insight into why growth in the (111) direction can compete effectively to form nanorods.[61, 175] It is also consistent with the observed

XPS spectra of nanorods, which exhibit no detectable iodide from a well-dispersed nanorod sample with their long axis parallel to the substrate (Figure 6.4B). Finally, at elevated concentrations of iodide, a layer of iodide is formed on the Au surface (as indicated by XPS, $I_{3d}$ = 618.9eV).[179] This layer may promote nanoprism formation by allowing the chemical reactivity of the different crystal facets to dominate the growth processes with growth at the high energy side crystal facets favored.[104] Taken together, this model presents a series of competing factors for directing anisotropic nanoparticle growth where iodide plays the primary mediating role.

### 6.3.2 Role of Seed

Investigations into the role of iodide provide information not only about the role of iodide in these syntheses, but also about the role of the seed nanoparticles. As has been already described, the role of iodide directs the final nanoparticle shape for the same solution of seed particles. These results indicate that the shape of the seed nanoparticle itself is not a dominant factor in determining whether the CTAB-based seed-mediated syntheses produces nanorods, nanoprisms, or nanospheres. However, it should be noted that these observations likewise do not eliminate the role of the seed in the final morphology of the nanoparticle, because only three nanoparticle architectures are observed. Therefore the original seed nanoparticle geometry and crystal facets (as dictated by the possible geometries of an fcc metal nanocrystal) may still play a role in narrowing the *possible* nanoparticle products. Empirically, the role of the original nanocrystal shape may be investigated by using different seed particles in a similar synthesis. For these experiments, both citrate-stabilized 13 nm gold nanoparticles (Ted Pella, Inc.) and phosphine ligand-stabilized Ag nanoparticles have been used to elucidate how the size, structure, and composition of the original nanoparticle seed affects the final nanoparticle morphology.

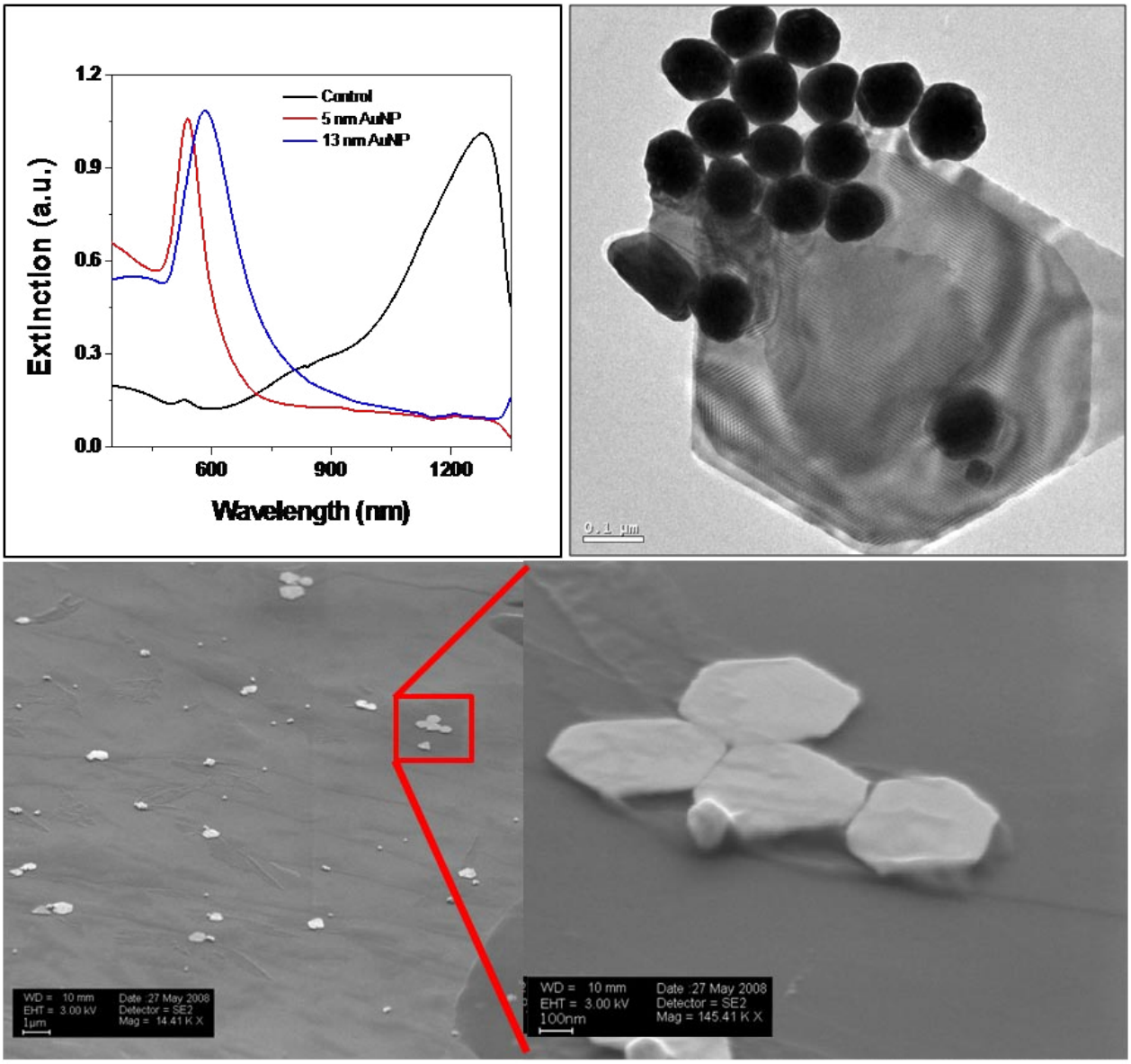


**Figure 6.6** Characterization of CTABr-based, seed-mediated nanoparticle synthesis using 13 nm Au nanoparticle seeds. The UV-vis-NIR spectrum shows no spectroscopically discernable anisotropic nanoparticle formation. However, TEM and SEM analysis reveal significant populations of very large (> 1µm) hexagonal and triangular nanoplates. The TEM image in the upper right shows two overlapping nanoplates which exhibit Moiré fringes and indicate that the plates are single crystalline.

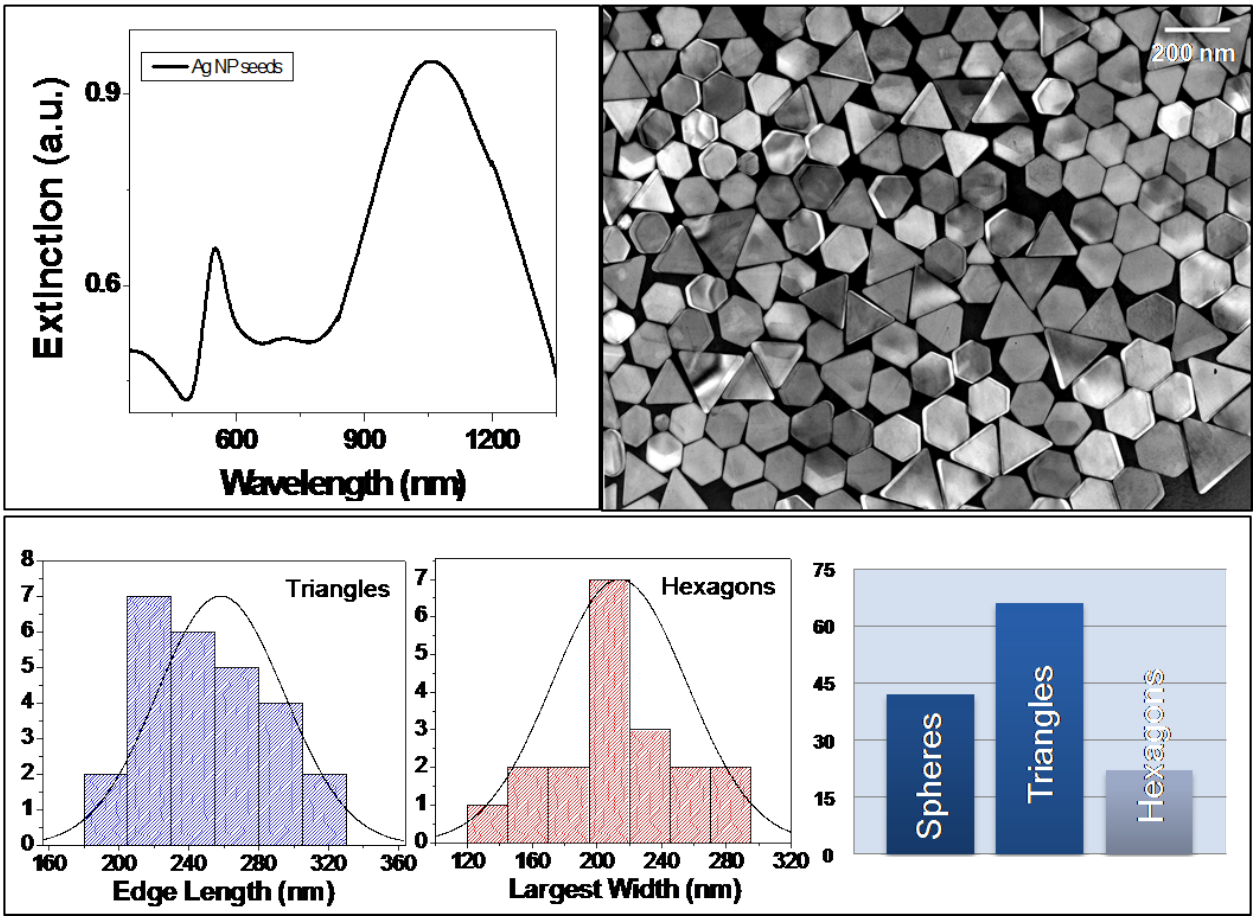


**Figure 6.7** Characterization of CTAB-based, seed-mediated nanoparticle synthesis using 5 nm Ag nanoparticle seeds. The UV-vis-NIR spectrum shows the characteristic spectrum of triangular platelike structures, which is confirmed by TEM. The bottom row shows statistical analysis of the size and shape distribution of the resulting nanoparticle products.

Using 13 nm Au nanoparticle seeds, in the presence of iodide, platelike growth occurs (Figure 6.6). Although, The UV-vis-NIR spectrum shows no spectroscopically discernable anisotropic nanoparticle formation (in this wavelength range), TEM and SEM analyses reveal significant populations of very large (> 1µm) hexagonal and triangular nanoplates. Further, TEM images frequently exhibit Moiré fringes which indicate that the plates are single crystalline (Figure 6.6, upper right). These results suggest that either the crystal facets of 13 nm Au nanoparticles are similar to the crystal facets of the borohydride generated Au seeds and the

same iodide influence exists for these particles, or they suggest that shape directing forces in this process are not directed by seed crystal morphology. However, while it is possible to characterize the crystal structure of the 13 nm Au nanoparticles, it is much more difficult to definitively characterize the active seed nanoparticle from the borohydride reduction case, because these particles are highly sensitive to Ostwald ripening and will change size quickly over the course of 2-4 hours from the time of synthesis. Therefore, isolating these seeds and comparing them to the 13 nm particles remains a challenge. However, another experiment can be designed to probe this question: a seed particle composed of a different material which will likely exhibit a different population of crystal facets can be used. For these experiments, BSPP-capped Ag nanoparticles have been synthesize and used as seeds. With these particles, the synthesis also produced platelike nanostructures, although much smaller than the micron size plates. However, like the micron sized plates, they are made in high yield (>70% before purification), and are composed of roughly half nanohexagons and half of nanotriangles (Figure 6.7).

**6.4 Conclusion**

For these studies, the original conditions reported by others [187], [52]and our group[84] have been used in an attempt to elucidate the shape-directing factors in CTABr-based, seeding methodologies for the production of gold nanospheres, nanorods, and nanoprisms. Importantly, these results demonstrate the critical role of iodide ion in these syntheses and the need for analytically pure CTABr, regardless of which morphology one wants to deliberately prepare. Additionally, preliminary work has been reported on the ability to use a variety of seed nanoparticles to effect platelike nanocrystal growth in the presence of this shape-directing halide ion. Taken together, this approach represents the first synthetic method for preparing either

nanoprisms, nanorods, or spherical nanoparticles made of gold that can be deliberately and consistently controlled based solely upon iodide ion concentration.

# REFERENCES

[1] G. Schmid, B. Corain, *J. Eur. Inorg. Chem.* **2003**, *2003*, 3081.

[2] A. N. Shipway, E. Katz, I. Willner, *Chem. Phys. Chem.* **2000**, *1*, 18.
[3] J. Xiang, W. Lu, Y. Hu, Y. Wu, H. Yan, C. M. Lieber, *Nature* **2006**, *441*, 489.
[4] Y. Cui, Z. H. Zhong, D. L. Wang, W. U. Wang, C. M. Lieber, *Nano Lett.* **2003**, *3*, 149.
[5] Y.-H. Chen, U. Nickel, *J. Chem. Soc. Faraday Trans.* **1993**, *89*, 2479
[6] R. M. Crooks, M. Zhao, L. Sun, V. Chechik, L. K. Yeung, *Acc. Chem. Res.* **2001**, *34*, 181.
[7] Y. Shiraishi, N. Toshima, *J. Mol. Catal.* **1999**, *141*, 187.
[8] M.-C. Daniel, D. Astruc, *Chem. Rev.* **2004**, *104*, 293.
[9] R. Narayanan, M. A. El-Sayed, *J. Phys. Chem. B* **2004**, *108*, 8572.
[10] R. Narayanan, M. A. El-Sayed, *J. Phys. Chem.* **2005**, *109*, 12663.
[11] R. Narayanan, M. A. El-Sayed, *J. Phys. Chem. B* **2004**, *108*, 5726.
[12] G. A. Somorjai, F. Tao, J. Y. Park, *Top. Catal.* **2008**, *47*, 1.
[13] N. L. Rosi, C. A. Mirkin, *Chem. Rev.* **2005**, *105*, 1547.
[14] H. D. Hill, C. A. Mirkin, *Nature Protoc.* **2006**, *1*, 324.
[15] J. A. Sioss, R. L. Stoermer, M. Y. Sha, C. D. Keating, *Langmuir* **2007**, *23*, 11334.
[16] R. Elghanian, J. J. Storhoff, R. C. Mucic, R. L. Letsinger, C. A. Mirkin, *Science* **1997**, *277*, 1078.
[17] J. J. Storhoff, R. Elghanian, R. C. Mucic, C. A. Mirkin, R. L. Letsinger, *J. Am. Chem. Soc.* **1998**, *120*, 1959.
[18] T. A. Taton, C. A. Mirkin, R. L. Letsinger, *Science* **2000**, *289*, 1757.
[19] Y. C. Cao, R. Jin, C. A. Mirkin, *Science* **2002**, *297*, 1536.
[20] S. J. Park, T. A. Taton, C. A. Mirkin, *Science* **2002**, *295*, 1503.
[21] J. M. Nam, C. S. Thaxton, C. A. Mirkin, *Science* **2003**, *301*, 1884.
[22] D. G. Georganopoulou, L. Chang, J. M. Nam, C. S. Thaxton, E. J. Mufson, W. L. Klein, C. A. Mirkin, *Proc. Natl. Acad. Sci. USA* **2005**, *102*, 2273.
[23] H. D. Hill, R. A. Vega, C. A. Mirkin, *Anal. Chem.* **2007**, *79*, 9218.
[24] D. S. Seferos, D. A. Giljohann, H. D. Hill, A. E. Prigodich, C. A. Mirkin, *J. Am. Chem. Soc.* **2007**, *129*, 15477.
[25] N. L. Rosi, D. A. Giljohann, C. S. Thaxton, A. K. R. Lytton-Jean, M. S. Han, C. A. Mirkin, *Science* **2006**, *312*, 1027.
[26] D. A. Giljohann, D. S. Seferos, P. C. Patel, J. E. Millstone, N. L. Rosi, C. A. Mirkin, *Nano Lett.* **2007**, *7*, 3818.
[27] L. R. Hirsch, R. J. Stafford, J. A. Bankson, S. R. Sershen, B. Rivera, R. E. Price, J. D. Hazle, N. J. Halas, J. L. West, *Proc. Natl. Acad. Sci. USA* **2003**, *100*, 13549.
[28] X. Huang, I. H. El-Sayed, W. Qian, M. A. El-Sayed, *J. Am. Chem. Soc.* **2006**, *128*, 2115.
[29] M. DiChristina, M. Roukes, G. M. Whitesides, J. C. Love, C. E. Schafmeister, N. C. Seeman, E. Shapiro, Y. Beneson, G. Gruner, H. A. Atwater, C. M. Lieber, A. P. Alivisatos, G. P. Collins, *Sci. Am.* **2007**, *17*, 1.
[30] V. Chan, R. Rengarajan, N. Rovedo, J. Wei, T. Hook, P. Nguyen, C. Jia, E. Nowak, C. Xiang-Dong, D. Lea, A. Chakravarti, V. Ku, S. Yang, A. Steegen, C. Baiocco, P. Shafer, N. Hung, H. Shih-Fen, C. Wann, in *Electron Devices Meeting, 2003. IEDM '03 Technical Digest. IEEE International*, **2003**, pp. 3.8.1.

[31] G. M. Whitesides, J. C. Love, *Sci. Am.* **2007**, *17*, 13.
[32] A. P. Alivisatos, *Science* **1996**, *271*, 933.
[33] J. T. Hu, T. W. Odom, C. M. Lieber, *Acc. Chem. Res.* **1999**, *32*, 435.
[34] C. Burda, X. Chen, R. Narayanan, M. A. El-Sayed, *Chem. Rev.* **2005**, *105*, 1025.
[35] M. A. El-Sayed, *Acc. Chem. Res.* **2001**, *34*, 257.
[36] K. L. Kelly, E. Coronado, L. L. Zhao, G. C. Schatz, *J. Phys. Chem. B* **2003**, *107*, 668.
[37] A. P. Alivisatos, *J. Phys. Chem.* **1996**, *100*, 13226.
[38] M. Haruta, *Gold Bull.* **2004**, *37*, 27.
[39] C. K. Chan, H. Peng, G. Liu, K. McIlwrath, X. F. Zhang, R. A. Huggins, Y. Cui, *Nat. Nano.* **2008**, *3*, 31.
[40] A. I. Hochbaum, R. Chen, R. D. Delgado, W. Liang, E. C. Garnett, M. Najarian, A. Majumdar, P. Yang, *Nature* **2008**, *451*, 163.
[41] H. A. Atwater, *Sci. Am.* **2007**, *17*, 56.
[42] C. A. Mirkin, R. L. Letsinger, R. C. Mucic, J. J. Storhoff, *Nature* **1996**, *382*, 607.
[43] S. A. Maier, P. G. Kik, H. A. Atwater, *Appl. Phys. Lett.* **2002**, *81*, 1714.
[44] "About the NNI - Home" National Nanotechnology Initiative Nanoscale Science and Engineering Subcommittee 18 Sept 2008 <www.nano.gov>
[45] R. Jin, Y. Cao, C. A. Mirkin, K. L. Kelly, G. C. Schatz, J. G. Zheng, *Science* **2001**, *294*, 1901.
[46] R. Garcia, R. V. Martinez, J. Martinez, *Chem. Soc. Rev.* **2006**, *35*, 29.
[47] G. M. Wallraff, W. D. Hinsberg, *Chem. Rev.* **1999**, *99*, 1801.
[48] C. Xue, C. A. Mirkin, *Angew. Chem. Int. Ed.* **2007**, *46*, 2036.
[49] G. Frens, *Nature, Phys. Sci.* **1973**, *241*, 20.
[50] M. Brust, M. Walker, D. Bethell, D. J. Schiffrin, R. Whyman, *J. Chem. Soc. Chem. Commun.* **1994**, 801.
[51] I. Hussain, S. Graham, Z. X. Wang, B. Tan, D. C. Sherrington, S. P. Rannard, A. I. Cooper, M. Brust, *J. Am. Chem. Soc.* **2005**, *127*, 16398.
[52] K. R. Brown, D. G. Walter, M. J. Natan, *Chem. Mater.* **2000**, *12*, 306.
[53] A. Taleb, C. Petit, M. P. Pileni, *Chem. Mater.* **1997**, *9*, 950.
[54] A. Henglein, M. Giersig, *J. Phys. Chem. B* **1999**, *103*, 9533.
[55] M. Q. Zhao, R. M. Crooks, *Adv. Mater.* **1999**, *11*, 217.
[56] C. W. Scheeren, G. Machado, J. Dupont, P. F. P. Fichtner, S. R. Texeira, *Inorg. Chem.* **2003**, *42*, 4738.
[57] T. Teranishi, M. Miyake, *Chem. Mater.* **1998**, *10*, 594.
[58] U. Kreibig, L. Genzel, *Surf. Sci.* **1985**, *156*, 678.
[59] A. Henglein, *Isr. J. Chem.* **1993**, *33*, 77.
[60] S. Link, M. B. Mohamed, M. A. El-Sayed, *J. Phys. Chem. B* **1999**, *103*, 3073.
[61] Z. L. Wang, R. P. Gao, B. Nikoobakht, M. A. El-Sayed, *J. Phys. Chem. B* **2000**, *104*, 5417.
[62] P. D. Jadzinsky, G. Calero, C. J. Ackerson, D. A. Bushnell, R. D. Kornberg, *Science* **2007**, *318*, 430.
[63] D. Astruc, F. Lu, J. R. Aranzaes, *Angew. Chem. Int. Ed.* **2005**, *44*, 7852.
[64] M. S. Gudiksen, L. J. Lauhon, J. Wang, D. C. Smith, C. M. Lieber, *Nature* **2002**, *415*, 617.
[65] P. K. Jain, K. S. Lee, I. H. El-Sayed, M. A. El-Sayed, *J. Phys. Chem. B* **2006**, *110*, 7238.

[66] M. Haruta, *Cat. Tech.* **2002**, *6*, 102.
[67] J. R. Lakowicz, *Anal. Biochem.* **2005**, *337*, 171.
[68] A. J. Haes, L. Chang, W. L. Klein, R. P. V. Duyne, *J. Am. Chem. Soc.* **2005**, *127*, 2264.
[69] C. S. Thaxton, D. G. Georganopoulou, C. A. Mirkin, *Clin. Chim. Acta* **2006**, *363*, 120.
[70] J. Perez-Juste, A. Mulvaney, L. M. Liz-Martan, *Int. J. Nanotechnol.* **2007**, *4*, 215.
[71] S. P. Liao, N. C. Seeman, *Science* **2004**, *306*, 2072.
[72] L. Qin, M. J. Banholzer, J. E. Millstone, C. A. Mirkin, *Nano Lett.* **2007**, *7*, 3849.
[73] J. D. Hood, M. Bednarski, R. Frausto, S. Guccione, R. A. Reisfeld, R. Xiang, D. A. Cheresh, *Science* **2002**, *296*, 2404.
[74] L. Brannon-Peppas, J. O. Blanchette, *Adv. Drug Deliver. Rev.* **2004**, *56*, 1649.
[75] N. R. Jana, L. Gearheart, C. J. Murphy, *J. Phys. Chem. B* **2001**, *105*, 4065.
[76] K. K. Caswell, C. M. Bender, C. J. Murphy, *Nano Lett.* **2003**, *3*, 667.
[77] B. Nikoobakht, M. A. El-Sayed, *Chem. Mater.* **2003**, *15*, 1957.
[78] M. Liu, P. Guyot-Sionnest, *J. Phys. Chem. B* **2005**, *109*, 22192.
[79] J. Perez-Juste, I. Pastoriza-Santos, L. M. Liz-Marzan, P. Mulvaney, *Coordin. Chem. Rev.* **2005**, *249*, 1870.
[80] C. J. Murphy, A. M. Gole, S. E. Hunyadi, C. J. Orendorff, *Inorg. Chem.* **2006**, *45*, 7544.
[81] C. S. Ah, Y. J. Yun, H. J. Park, W.-J. Kim, D. H. Ha, W. S. Yun, *Chem. Mater.* **2005**, *17*, 5558.
[82] S. Chen, D. L. Carroll, *Nano Lett.* **2002**, *2*, 1003.
[83] S. Chen, D. L. Carroll, *J. Phys. Chem. B* **2004**, *108*, 5500.
[84] J. E. Millstone, S. Park, K. L. Shuford, L. Qin, G. C. Schatz, C. A. Mirkin, *J. Am. Chem. Soc.* **2005**, *125*, 5312.
[85] S. S. Shankar, A. Rai, B. Ankamwar, A. Singh, A. Ahmad, M. Sastry *Nat. Mater.* **2004**, *3*, 482.
[86] R. Jin, S. Egusa, N. F. Scherer, *J. Am. Chem. Soc.* **2004**.
[87] B. Wiley, T. Herricks, Y. Sun, Y. Xia, *Nano Lett.* **2004**, *4*, 1733.
[88] D. Yu, V. W.-W. Yam, *J. Am. Chem. Soc.* **2004**, *126*, 13200.
[89] S. H. Im, Y. T. Lee, B. Wiley, Y. Xia, *Angew. Chem. Int. Ed.* **2005**, *44*, 2154.
[90] T. K. Sau, C. J. Murphy, *J. Am. Chem. Soc.* **2004**, *126*, 8648.
[91] C. G. Wang, T. T. Wang, Z. F. Ma, Z. M. Su, *Nanotechnology* **2005**, *16*, 2555.
[92] T. Cassagneau, F. Caruso, *Adv. Mater.* **2002**, *14*, 732.
[93] G. S. Métraux, Y. C. Cao, R. Jin, C. A. Mirkin, *Nano Lett.* **2003**, *3*, 519.
[94] F. Kim, J. H. Song, P. Yang, *J. Am. Chem. Soc.* **2002**, *124*, 14316.
[95] C. R. Martin, *Science* **1994**, *266*, 1961.
[96] C. R. Martin, *Science* **1994**, *266*, 1961.
[97] C. K. Preston, M. Moskovits, *J. Phys. Chem.* **1993**, *97*, 8495.
[98] S. J. Hurst, E. K. Payne, L. Qin, C. A. Mirkin, *Angew. Chem. Int. Ed.* **2006**, *45*, 2672.
[99] A. R. Tao, S. Habas, P. D. Yang, *Small* **2008**, *4*, 310.
[100] B. Wiley, Y. Sun, J. Chen, H. Cang, Z.-Y. Li, X. Li, Y. Xia, *MRS Bull.* **2005**, *30*, 356.
[101] J. Turkevich, P. C. Stevenson, J. Hillier, *Faraday Discuss.* **1951**, *11*, 55.
[102] L. M. Liz-Marzan, *Materials Today* **2004**, 26.
[103] C. Lofton, W. Sigmund, *Adv. Funct. Mater.* **2005**, *15*, 1197.
[104] J. E. Millstone, G. S. Metraux, C. A. Mirkin, *Adv. Funct. Mater.* **2006**, *16*, 1209.
[105] C. Xue, Z. Li, C. A. Mirkin, *Small* **2005**, *1*, 513.

[106] G. S. Métraux, C. A. Mirkin, *Adv. Mater.* **2005**, *17*, 412.
[107] C. Xue, J. E. Millstone, S. Y. Li, C. A. Mirkin, *Angew. Chem. Int. Ed.* **2007**, *46*, 8436.
[108] R. Jin, Y. C. Cao, E. Hao, G. S. Metraux, G. C. Schatz, C. A. Mirkin, *Nature* **2003**, *425*, 487.
[109] Y. L. Luo, *Mater. Lett.* **2007**, *61*, 1346.
[110] K. L. Shuford, M. A. Ratner, G. C. Schatz, *J. Chem. Phys.* **2005**, *123*, 114713.
[111] A. Sarkar, S. Kapoor, T. Mukherjee, *J. Colloid Interface Sci.* **2005**, *287*, 496.
[112] C. Li, W. Cai, Y. Li, J. Hu, P. Liu, *J. Phys. Chem. B* **2006**, *110*, 1546.
[113] Y. A. Sun, Y. N. Xia, *Adv. Mater.* **2003**, *15*, 695.
[114] D. H. Dahanayaka, J. X. Wang, S. Hossain, L. A. Bumm, *J. Am. Chem. Soc.* **2006**, *128*, 6052.
[115] P. Mulvaney, *Langmuir* **1996**, *12*, 788.
[116] E. K. Payne, K. L. Shuford, S. Park, G. C. Schatz, C. A. Mirkin, *J. Phys. Chem. B* **2006**, *110*, 2150.
[117] M. Maillard, P. Huang, L. Brus, *Nano Lett.* **2003**, *3*, 1611.
[118] A. Callegari, D. Tonti, M. Chergui, *Nano Lett.* **2003**, *3*, 1565.
[119] V. Bastys, I. Pastoriza-Santos, B. Rodríguez-González, R. Vaisnoras, L. M. Liz-Marzán, *Adv. Funct. Mater.* **2006**, *16*, 766.
[120] A. M. Junior, H. P. M. de Oliveira, M. H. Gehlen, *Photochem. Photobiol. Sci.* **2003**, *2*, 921.
[121] Y. Sun, B. Mayers, Y. Xia, *Nano Lett.* **2003**, *3*, 675.
[122] C. Xue, G. S. Metraux, J. E. Millstone, C. A. Mirkin, *J. Am. Chem. Soc.* **2008**, *130*, 8337.
[123] X. Wu, P. L. Redmond, H. Liu, Y. Chen, M. Steigerwald, L. Brus, *J. Am. Chem. Soc.* **2008**, *130*, 9500.
[124] P. L. Redmond, X. Wu, L. Brus, *J. Phys. Chem. C* **2007**, *111*, 8942.
[125] L.-P. Jiang, S. Xu, J.-M. Zhu, J.-R. Zhang, J.-J. Zhu, H.-Y. Chen, *Inorg. Chem.* **2004**, *43*, 5877.
[126] K. Okitsu, A. Yue, S. Tanabe, H. Matsumoto, Y. Yobiko, *Langmuir* **2001**, *17*, 7717.
[127] K. Okitsu, A. Yue, S. Tanabe, H. Matsumoto, Y. Yobiko, *Langmuir* **2007**, *23*, 13244.
[128] Y. Takeuchi, T. Ida, K. Kimura, *J. Phys. Chem. B* **1997**, *101*, 1322.
[129] Z. Xie, Z. Wang, Y. Ke, Z. Zha, C. Jiang, *Chem. Lett.* **2003**, *32*, 686.
[130] T. Tsuji, T. Higuchi, M. Tsuji, *Chem. Lett.* **2005**, *34*, 476.
[131] S. Remita, M. Mostafavi, M. O. Delcourt, *New J. Chem.* **1994**, *18*, 581.
[132] J. Belloni, M. Mostafavi, H. Remita, J.-L. Marignier, M.-O. Delcourt, *New J. Chem.* **1998**, 1239.
[133] I. Pastoriza-Santos, L. M. Liz-Marzan, *Nano Lett.* **2002**, *2*, 903.
[134] N. Malikova, I. Pastoriza-Santos, M. Schierhorn, N. A. Kotov, L. M. Liz-Marzan, *Langmuir* **2002**, *18*, 3694.
[135] T. J. Norman Jr., C. D. Grant, D. Magana, J. Z. Zhang, J. Liu, D. Cao, F. Bridges, A. Van Buuren, *J. Phys. Chem. B* **2002**, *106*, 7005.
[136] T. Klaus, R. Joerger, E. Olsson, C. G. Granqvist, *Proc. Natl. Acad. Sci. USA* **1999**, *96*, 13611.
[137] S. Chen, Z. Fan, D. L. Carroll, *J. Phys. Chem. B* **2002**, *106*, 10777.
[138] S. P. Chandran, M. Chaudhary, R. Pasricha, A. Ahmad, M. Sastry, *Biotechnol. Prog.* **2006**, *22*, 577.

[139] B. Liu, J. Xie, J. Y. Lee, Y. P. Ting, J. P. Chen, *J. Phys. Chem. B* **2005**, *109*, 15256.
[140] S. Brown, M. Sarikaya, E. Johnson, *J. Mol. Biol.* **2000**, *299*, 725.
[141] Y. Shao, Y. D. Jin, S. J. Dong, *Chem. Commun.* **2004**, 1104.
[142] M. Tsuji, M. Hashimoto, Y. Nishizawa, T. Tsuji, *Chem. Lett.* **2003**, *32*, 1114.
[143] I. Pastoriza-Santos, L. M. Liz-Marzan, *Langmuir* **2002**, *18*, 2888.
[144] T. R. Jensen, M. L. Duval, K. L. Kelly, A. A. Lazarides, G. C. Schatz, R. P. V. Duyne, *J. Phys. Chem. B* **1999**, *103*, 9846.
[145] A. J. Haes, R. P. V. Duyne, *J. Am. Chem. Soc.* **2002**, *124*, 10596.
[146] B. Wiley, Y. Sun, Y. Xia, *Langmuir* **2005**, *21*, 8077.
[147] B. J. Wiley, Y. Xiong, Z.-Y. Li, Y. Yin, Y. Xia, *Nano Lett.* **2006**, *6*, 765.
[148] J. C. Love, L. A. Estroff, J. K. Kriebel, R. G. Nuzzo, G. M. Whitesides, *Chem. Rev.* **2005**, *105*, 1103.
[149] O. M. Magnussen, *Chem. Rev.* **2002**, *102*, 679.
[150] S. Chen, S. Jagannathan, R. V. Mehta, R. Jagannathan, A. E. Taddei, *J. Imaging Sci. Technol.* **1998**, *42*, 399.
[151] M. G. Antoniades, J. S. Wey, *J. Imaging Sci. Technol.* **1995**, *39*, 323.
[152] M. G. Antoniades, J. S. Wey, *J. Imaging Sci.* **1998**, *42*, 393.
[153] J. E. Maskasky, *J. Imaging Sci.* **1986**, *30*, 247.
[154] C. T. Mumaw, E. F. Haugh, *J. Imaging Sci.* **1986**, *30*, 198.
[155] R. Jagannathan, *J. Imaging Sci.* **1991**, *35*, 104.
[156] R. Jagannathan, R. V. Mehta, J. A. Timmons, D. L. Black, *Phys. Rev. B* **1993**, *48*, 13261.
[157] N.-B. Ming, *J. Cryst. Growth* **1993**, *128*, 104.
[158] N.-B. Ming, H. Li, *J. Cryst. Growth* **1991**, *115*, 199.
[159] R. W. Berriman, R. H. Herz, *Nature* **1957**, *180*, 293.
[160] D. R. Hamilton, R. G. Seidensticker, *J. Appl. Phys.* **1960**, *31*, 1165.
[161] Y. Hosoya, S. Urabe, *J. Imaging Sci. Technol.* **1998**, *42*, 487.
[162] N.-B. Ming, K. Tsukamoto, I. Sunagawa, *J. Cryst. Growth* **1988**, *91*, 11.
[163] J.-M. Jin, N.-B. Ming, *Solid State Commun.* **1989**, *70*, 759.
[164] P. Bennema, G. Bögels, D. Bollen, T. Müssig, H. Meekes, *Imaging Sci. J.* **2001**, *49*, 1.
[165] T. H. Ha, H.-J. Koo, B. H. Chung, *J. Phys. Chem. C* **2007**, *111*, 1123.
[166] A. Rai, A. Singh, A. Ahmad, M. Sastry, *Langmuir* **2006**, *22*, 736.
[167] J. E. Millstone, W. Wei, M. R. Jones, H. Yoo, C. A. Mirkin, *Nano Lett.* **2008**, *ASAP*.
[168] D. L. Van Hyning, W. G. Klemperer, C. F. Zukoski, *Langmuir* **2001**, *17*, 3128.
[169] D. L. Van Hyning, W. G. Klemperer, C. F. Zukoski, *Langmuir* **2001**, *17*, 3120.
[170] D. L. Van Hyning, C. F. Zukoski, *Langmuir* **1998**, *14*, 7034.
[171] V. Germain, J. Li, D. Ingert, Z. L. Wang, M. P. Pileni, *J. Phys. Chem. B* **2003**, *107*, 8717.
[172] C. J. Johnson, E. Dujardin, S. A. Davis, C. J. Murphy, S. Mann, *J. Mater. Chem.* **2002**, *12*, 1765.
[173] N. R. Jana, L. Gearheart, C. J. Murphy, *Adv. Mater.* **2001**, *13*, 1389.
[174] J. X. Gao, C. M. Bender, C. J. Murphy, *Langmuir* **2003**, *19*, 9065.
[175] B. Nikoobakht, M. A. El-Sayed, *Langmuir* **2001**, *17*, 6368.
[176] A. J. Mieszawska, F. P. Zamborini, *Chem. Mater.* **2005**, *17*, 3415.
[177] R. G. Sanedrin, D. G. Georganopoulou, S. Park, C. A. Mirkin, *Adv. Mater.* **2005**, *17*, 1027.
[178] D. K. Smith, B. A. Korgel, *Langmuir* **2008**, *24*, 644.

[179] B. G. Bravo, S. L. Michelhaugh, M. P. Soriaga, I. Villegas, D. W. Suggs, J. L. Stickney, *J. Phys. Chem.* **1991**, *95*, 5245.
[180] T. S. Ahmadi, Z. L. Wang, T. C. Green, A. Henglein, M. A. El-Sayed, *Science* **1996**, *272*, 1924.
[181] R. M. Crooks, M. Q. Zhao, L. Sun, V. Chechik, L. K. Yeung, *Accounts of Chemical Research* **2001**, *34*, 181.
[182] H. Bönnemann, R. M. Richards, *Eur. J. Inorg. Chem.* **2001**, 2455.
[183] A. Bezryadin, C. Dekker, G. Schmid, *App. Phys. Lett.* **1997**, *71*, 1273.
[184] E. Katz, I. Willner, *Angew. Chem. Int. Ed.* **2004**, *43*, 6042.
[185] S. Link, Z. L. Wang, M. A. El-Sayed, *J. Phys. Chem. B* **1999**, *103*, 3529.
[186] C. L. Haynes, A. D. McFarland, L. Zhao, R. P. Van Duyne, G. C. Schatz, L. Gunnarsson, J. Prikulis, B. Kasemo, M. Kall, *J. Phys. Chem. B* **2003**, *107*, 7337.
[187] B. D. Busbee, S. O. Obare, C. J. Murphy, *Adv. Mater.* **2003**, *15*, 414.
[188] B. T. Draine, P. J. Flatau, *J. Opt. Soc. Am. A* **1994**, *11*, 1491.
[189] N. R. Jana, L. Gearheart, C. J. Murphy, *Chem. Mater.* **2001**, *13*, 2313.
[190] D. W. Lynch, W. R. Hunter, in *Handbook of Optical Constants of Solid* (Ed.: E. D. Palik), Academic Press, New York City, **1985**, p. 275.
[191] M. L. Theye, *Phys. Rev. B* **1970**, *2*, 3060.
[192] B. Dold, R. Mecke, *Optik* **1965**, *22*, 435.
[193] Y. G. Sun, Y. N. Xia, *Science* **2002**, *298*, 2176.
[194] S. Stoeva, K. J. Klabunde, C. M. Sorensen, I. Dragieva, *J. Am. Chem. Soc.* **2002**, *124*, 2305.
[195] Y. Sun, Y. Xia, *Adv. Mater.* **2003**, *15*, 695.
[196] S. Mosseri, A. Henglein, E. Janata, *J. Phys. Chem.* **1989**, *93*, 6791.
[197] D. R. Lide, 83 ed., CRC Press, Boca Raton, FL, pp. 8.
[198] J. G. Mclean, B. Krishnamachari, D. R. Peale, E. Chason, J. P. Sethna, B. H. Cooper, *Phys. Rev. B: Condens. Matter* **1997**, *55*, 1811.
[199] V. Chechik, *J. Am. Chem. Soc.* **2004**, *126*, 7780.
[200] A. Henglein, *Chem. Rev.* **1989**, *89*, 1861.
[201] G. Rupprechter, H. Unterhalt, M. Morkel, P. Galletto, L. J. Hu, H. J. Freund, *Surf. Sci.* **2002**, *502*, 109.
[202] P. Zapol, L. A. Curtiss, *J. Comput. Theor. Nanos* **2007**, *4*, 222.
[203] P. V. Kamat, *J. Phys. Chem. B* **2002**, *106*, 7729.
[204] E. Dujardin, L. B. Hsin, C. R. C. Wang, S. Mann, *Chem. Commun.* **2001**, 1264.
[205] A. Gole, C. J. Murphy, *Langmuir* **2005**, *21*, 10756.
[206] R. Jin, G. Wu, Z. Li, C. A. Mirkin, G. C. Schatz, *J. Am. Chem. Soc.* **2003**, *125*, 1643.
[207] X. G. Peng, J. Wickham, A. P. Alivisatos, *J. Am. Chem. Soc.* **1998**, *120*, 5343.
[208] S. H. Chen, D. L. Carroll, *Nano Lett.* **2002**, *2*, 1003.
[209] S. J. Hurst, A. K. R. Lytton-Jean, C. A. Mirkin, *Anal. Chem.* **2006**, *78*, 8313.
[210] T. M. Herne, M. J. Tarlov, *J. Am. Chem. Soc.* **1997**, *119*, 8916.
[211] M. J. Hostetler, A. C. Templeton, R. W. Murray, *Langmuir* **1999**, *15*, 3782.
[212] X. Y. Xu, N. L. Rosi, Y. H. Wang, F. W. Huo, C. A. Mirkin, *J. Am. Chem. Soc.* **2006**, *128*, 9286.
[213] S. Y. Park, A. K. R. Lytton-Jean, B. Lee, S. Weigand, G. C. Schatz, C. A. Mirkin, *Nature* **2008**, *451*, 553.

[214] P. K. Jain, X. Huang, I. H. El-Sayed, M. A. El-Sayad, *Plasmonics* **2007**, *2*, 107.
[215] P. K. Jain, X. Huang, I. H. El-Sayed, M. A. El-Sayed, *Acc. Chem. Res.* **2008**.
[216] A. K. R. Lytton-Jean, C. A. Mirkin, *J. Am. Chem. Soc.* **2005**, *127*, 12754.
[217] D. S. Seferos, D. A. Giljohann, N. L. Rosi, C. A. Mirkin, *Chembiochem* **2007**, *8*, 1230.
[218] L. Qin, J.-W. Jang, L. Huang, C. A. Mirkin, *Small* **2007**, *3*, 86
[219] D. Gershon, *Nature* **2002**, *416*, 885.
[220] R. Wilson, A. R. Cossins, D. G. Spiller, *Angew. Chem. Int. Ed.* **2006**, *45*, 6104.
[221] J.-M. Nam, C. S. Thaxton, C. A. Mirkin, *Science* **2003**, *301*, 1884.
[222] D. J. Milliron, S. M. Hughes, Y. Cui, L. Manna, J. Li, L.-W. Wang, A. P. Alivisatos, *Nature* **2004**, *430*, 190.
[223] N. L. Rosi, C. A. Mirkin, *Chem. Rev.* **2005**, *105*, 1547.
[224] Y. C. Cao, R. Jin, J.-M. Nam, C. S. Thaxton, C. A. Mirkin, *J. Am. Chem. Soc.* **2003**, *125*, 14676.
[225] R. Wilson, A. R. Cossins, D. G. Spiller, *Angew. Chem. Int. Ed.* **2006**, *45*, 6104.
[226] S. R. Nicewarner-Peña, G. Freeman, B. D. Reiss, L. He, D. J. Peña, I. D. Walton, R. Cromer, C. D. Keating, M. J. Natan, *Science* **2001**, *294*, 137.
[227] J. B.-H. Tok, F. Y. S. Chuang, M. C. Kao, K. A. Rose, S. S. Pannu, M. Y. Sha, G. Chakarova, S. G. Penn, G. M. Dougherty, *Angew. Chem. Int. Ed.* **2006**, *45*, 6900
[228] R. L. Stoermer, K. B. Cederquist, S. K. McFarland, M. Y. Sha, S. G. Penn, C. D. Keating, *J. Am. Chem. Soc.* **2006**, *128*, 16892.
[229] R. L. Stoermer, C. D. Keating, *J. Am. Chem. Soc.* **2006**, *128*, 13243.
[230] L. Qin, S. Park, L. Huang, C. A. Mirkin, *Science* **2005**, *309*, 113.
[231] L. Qin, S. Zou, C. Xue, A. Atkinson, G. C. Schatz, C. A. Mirkin, *Proc. Natl. Acad. Sci. U. S. A.* **2006**, *103* 13300.
[232] C. L. Haynes, A. D. McFarland, R. P. V. Duyne, *Ananlytical Chemistry* **2005**, *77*, 338A.
[233] Y. C. Cao, R. Jin, C. A. Mirkin, *Science* **2002**, *297*, 1536
[234] S. Nie, S. R. Emory, *Science* **1997**, *275*, 1102.
[235] D. L. Jeanmaire, R. P. V. Duyne, *J. Electroanal. Chem.* **1977**, *84*, 1.
[236] C. L. Haynes, A. D. McFarland, R. P. V. Duyne, *Anal. Chem.* **2005**, *77*, 338A.
[237] D. P. Fromm, A. Sundaramurthy, A. Kinkhabwala, P. J. Schuck, G. S. Kino, W. E. Moerner, *J. Chem. Phys.* **2006**, *124*, 061101.
[238] R. Narayanan, M. A. El-Sayed, *Nano Lett.* **2004**, *4*, 1343.
[239] T. H. Ha, H. J. Koo, B. H. Chung, *J. Phys. Chem. C* **2007**, *111*, 1123.
[240] X. Bu, T. Wang, G. Hall, *J. Anal. At. Spectrom.* **2003**, *18*, 1443.
[241] L. V. Dearden, E. M. Woolley, *J. Phys. Chem.* **1987**, *91*, 2404.

# CURRICULUM VITAE

# Jill E. Millstone

2145 Sheridan Road · Dept. of Chemistry
Evanston, IL 60208 · (W): 847.467.2438 · (C): 412.916.1895
e-mail: j-millstone@northwestern.edu


---

## Education

Northwestern University, Evanston, IL — Sept. 2003 – June 2008

- Ph.D. in Chemistry (Concentration: Materials Chemistry)

Carnegie Mellon University, Pittsburgh, PA — Sept. 1999 - May 2003

- B. S. Chemistry / B. S. English

## Research Experience

Northwestern University, Graduate Research (Advisor: Chad A. Mirkin) — Jan. 2004 - present

- Developed high yield synthesis for colloidal gold nanoprisms; collaborated with faculty experts to develop theoretical framework for discovery
- Demonstrated the unique optical features of colloidal gold nanoprisms and developed the use of these optical properties as an *in situ* test of nanostructure size and purity
- Investigated colloid surface energetics, leading to control of nanoprism size and surface chemistry with implications for catalysis, assembly and biodiagnostics
- Elucidated role of iodide ion in Au nanoparticle growth and developed mechanism for anisotropic nanoparticle growth combining strategies from, materials science, and electrochemistry
- Served as subgroup leader, graduate/undergraduate student research mentor, group information technology administrator, and spectrophotometer technician
- *Thesis title:* Synthesis, Properties, and Applications of Colloidal Gold Nanoprisms

Carnegie Mellon University, Undergraduate Research (Advisor: Richard McCullough) — Sept. 2001- Jan 2003

- Synthesized and characterized thiophene derivatives with bioactive substituents
- *Thesis title:* Regioregular Poly(3-alkylthiophenes) for Chromic Biosensor Devices

Carnegie Mellon University, Undergraduate Research (Advisor: Kathy Newman) — Jan. 2003 – May 2003

- *Thesis title:* Mr. Wizard and the Ultimate Demonstration: Making a Nation of Scientists in Cold War America

## Awards and Honors

| | |
|---|---|
| Northwestern University Graduate School Presidential Fellowship | 2007 - 2009 |
| Nanoscale Science and Engineering Outstanding Researcher Award | 2008 |
| Nanoscale Science and Engineering Service Award | 2008 |
| Materials Research Society Graduate Student Gold Award | 2007 |
| Edmund W. Gelewitz Outstanding Graduate Student Award | 2007 |
| Phi Lambda Upsilon Travel Fellowship | 2007 |
| National Science Foundation Pan-American Advanced Studies Institute Fellow | 2006 |
| Carnegie Mellon University Senior Leadership Award | 2003 |
| Carnegie Mellon University Department of Chemistry Commencement Speaker | 2003 |
| Carnegie Mellon University Dean's List with Honors | 2001 - 2003 |

## Publications

1. **Millstone, J. E.,** Georganopoulou, D. G., Xu, X., Li, S., Mirkin, C. A. "DNA-Au Nanoprism Conjugates" *Small*, **2008**, *in press.*
2. **Millstone, J. E.**; Wei, W.; Jones, M. R.; Yoo, H.; Mirkin, C. A. "Iodide Ions Control Seed-mediated Growth of Anisotropic Gold Nanoparticles" *Nano Lett.* **2008***, 8*, 2526–2529.
3. Wei, W.; Li, S.; Qin, L.; Xue, C.; **Millstone, J. E.**; Xu, X.; Schatz, G. C.; Mirkin, C. A. "Surface Plasmon-Mediated Energy Transfer in Heterogap Au–Ag Nanowires" *Nano Lett.* **2008**, *ASAP.*
4. Xue, C.; Métraux, G. S.; **Millstone, J. E.**; Mirkin, C. A. "A Mechanistic Study of Photomediated Silver Nanoprism Growth," *J. Am. Chem. Soc.,* **2008**, *130*, 8337.
5. Banholzer, M. J.; **Millstone, J. E.** ; Qin, L. ; Mirkin, C. A. "Rationally Designed Nanostructures for Surface-Enhanced Raman Scattering," *Chem. Soc. Rev*., **2008***, 37*, 885.
6. Giljohann, D. A.; Seferos, D. S.; Patel, P.; **Millstone, J. E.**; Rosi, N. L.; Mirkin, C. A. "Oligonucleotide Loading Determines Cellular Uptake of DNA-Modified Gold Nanoparticles," *Nano Lett.* , **2007**, *7*, 3818.
7. Qin, L.*; Banholzer, M. J*; **Millstone, J. E.** *; Mirkin, C. A. "Nanodisk Codes," *Nano Lett* , **2007**, *7*, 3849.
    - "Research Highlight" *Nature* **2007**, *450*, 925. New Scientist Magazine "Special Report", Nov 30 2007; "Research Highlight" *Nature Nanotechnology* Dec 14 2007. ** indicates equal author contribution*
8. Xue, C.; **Millstone, J. E.**; Mirkin, C. A. "Plasmon-Driven Synthesis of Triangular Core-Shell Nanoprisms From Gold Seeds," *Angew. Chem., Int. Ed. Engl.,* **2007**, *46*, 8436.
9. Li, S. Y.; **Millstone, J. E.**, Mirkin, C. A., Dravid, V. P. "Detection of Phosphorous in Biological Samples with Analytical Electron Microscopy," *Microsc. Microanal.* **2007**, *13*, 456.
10. Oh, B. K.; Park, S.; **Millstone, J. E.**; Lee, S. W.; Lee, K. B.; Mirkin, C. A. "Separation of Tricomponent Protein Mixtures with Triblock Nanorods" *J. Am. Chem. Soc.*, **2006**, *128*, 11825.
11. **Millstone, J. E.**; Metraux, G. S.; Mirkin, C. A. "Controlling the Edge Length of Gold Nanoprisms via a Seed-Mediated Approach" *Adv. Funct. Mat.* **2006**, *16*, 1209.
    - *Selected:* "Advances in Advance" by Wiley-VCH editors, May 2006.

12. **Millstone, J. E.**; Park, S.; Shuford, K. L.; Qin, L.; Schatz, G. C.; Mirkin, C. A. "Observation of a Quadrupole Plasmon Mode for a Colloidal Solution of Gold Nanoprisms," *J. Am. Chem. Soc.* **2005**, *127*, 5312.
    - *Selected:* "Hot Paper" of 2005, Journal of the American Chemical Society

## Selected Presentations

1. **Millstone, J. E.** "Gold Nanoprisms: A New Class of Inorganic Nanoparticle" *Lawrence Livermore National Laboratory*, Livermore, CA Mar. 14, 2008. (invited presentation)
2. **Millstone, J. E.**; Mirkin, C. A. "Synthesis and Behavior of Oligonucleotide Functionalized Anisotropic Gold Nanostructures" *Materials Research Society,* Boston, MA Nov. 27, 2007. (invited presentation)
3. **Millstone, J. E.** "Introduction to Nanoscience and Nanotechnology" *Illinois Institute of Technology*, Chicago, IL Oct. 20, 2007. (invited presentation)
4. **Millstone, J. E.**; Seferos, D.; Xu, X.; Mirkin, C. A. "Synthesis and Behavior of Oligonucleotide Functionalized Anisotropic Gold Nanostructures" *American Chemical Society*, Chicago, IL Mar. 25, 2007. (oral presentation)
5. **Millstone, J. E.**; Mirkin, C. A. "Observation, Analysis, and Utilization of a Quadrupole Plasmon Mode for Colloidal Solution of Gold Nanoprisms" *Pittsburgh Conference*, Chicago, IL Mar. 1, 2007. (oral presentation)
6. **Millstone, J. E.**; Payne, E. K.; Macrenaris, K.; Mirkin, C. A. "Shape-Dependent Behavior of Oligonucleotide Functionalized Gold Nanostructures" *Pan-American Advanced Studies Institute on Nano and Biotechnology*, San Carlos de Bariloche, Argentina Nov. 16, 2006. (poster presentation)
7. **Millstone, J. E.,** Mirkin, C. A. "Introduction to Nanoscience and Nanotechnology" *Hyde Park Unitarian Church*, Chicago, IL June 11, 2006. (invited presentation)
8. **Millstone, J. E.**; Schatz, G. C.; Mirkin, C. A. "Observation of a Quadrupole Plasmon Mode for a Colloidal Solution of Gold Nanoprisms" *Materials Research Society*, Boston, MA Nov. 30, 2005. (poster presentation)

## Selected Patents and Disclosures

1. Mirkin, C. A.; Xue, C.; **Millstone, J. E.** "Plasmon-Driven Synthesis of Triangular Core-Shell Nanoprism" (NU 27098) February, 2008.
2. Wei, W. , Qin, L., Xue, C., **Millstone, J. E**., Xu, X, Mirkin, C. A., Li, S., Schatz, G. C., "Method of Energy Transfer using Surface Plasmon Resonance Excitation" Disclosure, September 2007.
3. Mirkin, C. A.; **Millstone, J. E.**; Qin, L.; Banholzer, M. J. "Nanodisk Codes" Provisional Patent, May 2007.
4. Mirkin, C. A.; **Millstone, J. E.**; Park, S., Métraux, G. S. "Method of Producing Gold Nanoprisms" PCT Intl. Appl. WO2006US8930; EPO WO2006099312, September 21, 2006.

## Teaching and Leadership Experience

| | |
|---|---|
| *Leader,* Anisotropic Materials Subgroup | Jul. 2007 – June 2008 |
| *Co-Founder*, "Plant-it Purple" Graduate Gardens<br>• Community Building Grant Proposal Winner 2007 – 2008 | Jun. 2007 – June 2008 |
| *Mentor*, National Science Foundation Research Experience for Undergraduates (REU) | Jun. 2007 – Aug. 2007 |
| *Team Leader*, Department of Chemistry Outreach - Science in the Classroom | Jan. 2006 – May 2006 |
| *Mentor*, National Science Foundation Research Experience for Science Teachers (REST) | Jun. 2005 – Aug. 2006 |
| *Tutor,* Evanston Township High School and North Shore Country Day School | Jul. 2004 – June 2008 |
| *Teaching Assistant,* Northwestern University Analytical Instrumentation Lab | Sept. 2003 – Sept. 2004 |
| *Managing Editor,* Carnegie Mellon Undergraduate Research Journal | Jan. 2003 – May 2003 |
| *Teaching Assistant,* Carnegie Mellon Undergraduate Chemistry Lab | Jan. 2002 – May 2003 |

## Professional Affiliations

- Sigma Xi Scientific Research Society 2007 - present
- Phi Lambda Upsilon (Alpha Gamma Chapter) Chemistry Honors Society, 2005-present
- Materials Research Society, 2005 - present
- American Chemical Society, 2003 – present
- Association for Women in Science, 2001 – present